UNIVERSITY OF COPENHAGEN
FACULTY OF SCIENCE

Master's Thesis

Electron Interference and Mobility in InAs-based Nanostructures

by Christian Emanuel Noes Petersen

Supervisor: Thomas Sand Jespersen and Jesper Nygård

Submitted: May 20, 2022

Center for Quantum Devices, Niels Bohr Institute

Abstract

This thesis was motivated by the desire to have a quantum simulator capable of addressing open research questions in strongly correlated matter, such as the Cooper pairing mechanism that leads to unconventional superconductivity. In the engineering of the simulator, we choose nanostructures due to their intrinsic, hard wall confinement and the possibility to exploit their low dimensionality and tune energy scales before introducing electrostatic gating schemes. We will aim to prepare the simulator in a state that can be modelled with the simplest known Hamiltonian in condensed matter physics that accounts for strong correlations - the Hubbard Hamiltonian. Hence, we dub the simulator: "a Hubbard lattice". This model assumes that all particles are in the lowest Bloch band, which from an experimental point of view, makes disorder potentials generated by random impurities with energy fluctuations that match band gap energies important. Thus, reducing impurity content remains a crucial goal in these nanostructures and this requires significant insight into the material parameters that define physical properties such as the scattering mechanisms and retained phase of conduction particles. In this thesis, I present results related to these material parameters by studying indium-arsenide nanostructures. To study scattering mechanisms in a particular density regime, we develop a new method to extract a carrier density-dependent mobility from a two-terminal field-effect transistor measurement and demonstrate an excellent match with the Hall mobility. To study quantum effects arising from phase-coherent particles, I study universal conductance fluctuations, specifically, the statistics in normal-superconducting nanowires, which has not been done before. I show that it is possible to probe the symmetry-breaking mechanism from the amplitude of these fluctuations in different regimes. Some of the obtained results are in agreement with prediction from theory but other results disagreed strongly. We, therefore, suggest future work to clarify these issues. Finally, I present preliminary tight-binding calculations, on 2-dimensional square Hubbard lattices with dimensions matching those of the most recent selective-area-growth synthesized lattices. I show that it is possible to create localized orbitals in the junctions of the lattices which is an essential feature in simulating the Hubbard lattice.

Acknowledgements

I would like to thank all the members of Thomas Sand Jespersen's group. Thomas, Dags, Daria, Damon, Charline and Gunjan. It is a great pleasure to work with you all. In my opinion, this group is a fantastic composition of different talents and the future must be bright.

A special thanks, of course, to Damon who has been exceptional as a mentor since I started as a master's student at Qdev. Thanks for pushing me when I needed it and thanks for not pushing when I didn't need it - you know it.

Thanks to Helene and the kids at home, Bertram and Alberte, for all the support. I look forward to spending more time with you.

Contents

Chapter 1

Introduction

A major goal in condensed matter physics is the realisation of a quantum simulator capable of experimentally testing theories surrounding strongly correlated systems. The physics of strongly correlated systems - i.e. systems where electron-electron interactions can dominate the way electrons pass through a material - has been posited to explain high temperature superconductivity in certain materials[1,2]. However, the computational difficulty of solving even the most simple, easy-to-understand Hamiltonian when strong correlations are turned on means researchers have long sought to build simulators, or even quantum computers that could directly manifest the behaviour of strongly correlated systems in a controllable way[3,4]. That is a comprehensive task that requires a significant insight into the physical systems of interest. One crucial task towards making strongly correlated materials is to minimize random disorder potentials arising from impurities and/or defects, introduced during the growth/fabrication processes required to realise the nanoscale objects and systems that will constitute the simulator/computer. Disorder can be charge impurities, point defects, atomic vacancies, surface roughness, patterning imperfections etc.[5] Learning which parameters in the growth and/or fabrication process are the source of disorder is an absolute priority if we are to eliminate them. A measurable parameter that quantifies the level of disorder is the charge carrier mobility. The inherent difficulty in performing four-terminal Hall effect measurements on nanostructures, including nanowires (NWs)[6], means that the mobility is often reported as a single number from field-effect transistor (FET) measurements. This does not provide sufficient information about the underlying scattering mechanisms that determine the mobility in a particular carrier density regime. Thus one of the subjects of this thesis work has been to develop a method to accurately extract the gate voltage-dependent mobility from two-terminal FET measurements similar to a Hall mobility. A study of coherent electron transport allows for the observation of quantum interference (QI) effects that can provide information on the presence of disorder. One manifestation of QI-effects originating from randomly distributed disorder is universal conductance fluctuations (UCF). Contrary to Fabry-Perot interference that can be observed in disorder free electron waveguides where scattering only occur on the contacts, UCF are non-periodic reproducible fluctuations of the conductance observed upon varying disorder, fermi-wavelength or magnetic field (see fig. 1.1). Aside from information about the presence of disorder, the amplitude of UCF holds information about the phase coherence length - the typical distance that a conduction electron retains phase information - and the fundamental symmetries that are present in the system. Thus, in the view of the goal of minimizing disorder it is relevant to study and understand the phenomena related to UCF in NWs and this has been one of the subjects studied in this

thesis.

1.1 Thesis Outline

The work described in this thesis is **1)** a discussion of the physics of NW lattices **2)** Considerations of the mobility and the physics of UCF in NWs. The first chapter will introduce the theoretical background needed to appreciate the results and used subsequently to interpret the experimental results. A considerable fraction of the time in this project has been spent on experimentally fabricating nanowire electrical devices and measuring their properties at low temperatures. These experimental techniques are described in section 3. Chapter 5 contains

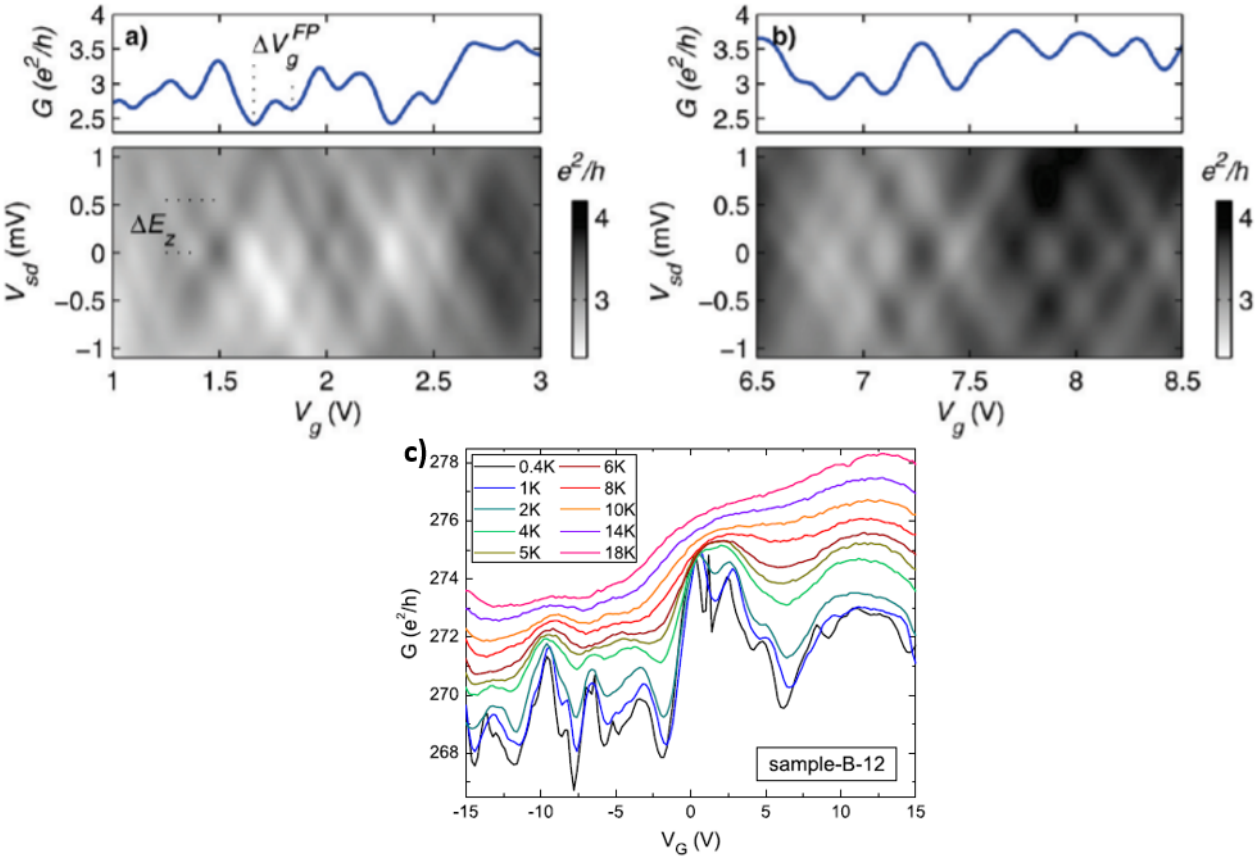

Figure 1.1: Fabry-Perot Oscillation vs. UCF. **a-b)**, show the regular chess-board pattern of Fabry-Perot oscillations at two regions of V_g, indicating a disorder free sample. The conductance as a function of gate voltage oscillates periodically with a periodicity of ΔV_g^{FP}. Adapted from ref.[7]. **c**, Example of UCF in a disordered sample. The conductance fluctuates non-periodically as a function of gate voltage. UCF are most pronounced at low temperatures in the phase-coherent regime. Adapted from ref.[8].

the main experimental results and analysis, and finally, considerations of NW lattices are discussed in chapter 6 based on a tight-binding model which has also been developed during the course of the project. In addition to this thesis, the mobility results were presented as a contributed talk at NanoWireWeek in Chamonix-Mont-Blanc on the 28th of April 2022 (see appendix A1). Also, two manuscripts are under preparation, one collecting the mobility work and one discussing the role of electron-hole symmetry for UCF.

Chapter 2

Theoretical Background

This chapter introduces the physics of UCF and provides a discussion of the carrier mobility with an overview of the currently used theoretical models for mobility extraction from a two-terminal FET measurement of NWs. Finally, the motivation for a new method to more accurately quantify scattering mechanisms in two-terminal nanostructures will be discussed.

2.1 Conductance Fluctuations in Mesoscopic Samples

Studies of transport in mesoscopic wires with a size less than the inelastic scattering length reveal a range of quantum phenomena[9]. UCF is one such phenomenon. While the theory of UCF in semiconductors/metals was thoroughly supported experimentally during the 1980's[10–16], the same is not true for normal(N)-superconductor(S)-junctions. That motivates the first part of the thesis. First a brief discussion is given on the well-established theory of UCF in disordered semiconductor systems. Here a simplified explanation to the value of the UCF-amplitude will be given. Then follows more convincing arguments of the UCF-amplitudes based on random matrix theory (RMT) including further insight into the role of fundamental symmetries of the system. The theory section of UCF ends with an introduction to UCF in NS-devices in the light of RMT.

2.1.1 Quantum Diffusive Transport - Universal Conductance Fluctuations

In small semiconducting wires at low temperatures, the conductance fluctuates as a function of the magnetic field or by changing the Fermi energy[8]. The fluctuations are different from noise in the usual sense in that they are time-independent stochastic patterns, reproducible in a given sample[17,18]. Remarkably, when the temperature is such that the phase coherence length, l_ϕ, is on the order of or larger than the sample size dimensions, the amplitude of the fluctuations are on the order of $\frac{e^2}{h}$. In disordered samples, this amplitude is constant[19] regardless of the degree of disorder and sample size, as long as the mean free path, l_m is much shorter than the length of the sample, L, hence the name *"universal conductance fluctuations"*, (UCF).

In the "*diffusive transport*" regime the elastic scattering of electrons takes place on length scales that are small compared to the size of the sample[21]. In the classical-diffusive regime a narrow wire can be divided into $\mathcal{N} = \frac{L}{l_m}$ *independently* fluctuating segments[20]. The uncertainty on the mean conductance, $\langle G \rangle$, falls off as $(\frac{l_m}{L})^{\frac{1}{2}}$, making the fluctuations in a classical wire negligible for $\frac{L}{l_m} \gg 1$. For a channel in the quantum diffusive transport regime the subdivided segments are quantum mechanically correlated on a length-scale determined by l_ϕ, the phase-coherence length determined by inelastic scattering by e.g. phonons. This length can, at low temperatures be much longer than l_m. On calculating probabilities of processes, one then has to include quantum interference terms. When phase coherence is maintained over the entire disordered sample, $l_\phi \geq L \gg l_m$, the theory of UCF predicts that $\delta \mathrm{G} \approx \frac{e^2}{h}$ at T=0[22,23]. Figure 2.2 is the starting point of the following argument for the UCF-amplitude. In a disordered quantum wire containing source and drain contacts with a scattering region in between at T=0 K, the Landauer equation takes the form[20,24]:

$$G = \frac{e^2}{h} \sum_{\alpha,\beta=1}^{N} \mid t_{\alpha\beta} \mid^2 \tag{2.1}$$

Where $\mid t_{\alpha\beta} \mid^2$ is the quantum mechanically transmission probability amplitude from the incident channel, α, to the outgoing channel, β. N represents the number of transverse modes, here each spin orientation counts as one mode. Given that $L \gg l_m$, each mode carries, on average, the same transmission probability. Using Drude theory[25] with eq. 2.1,

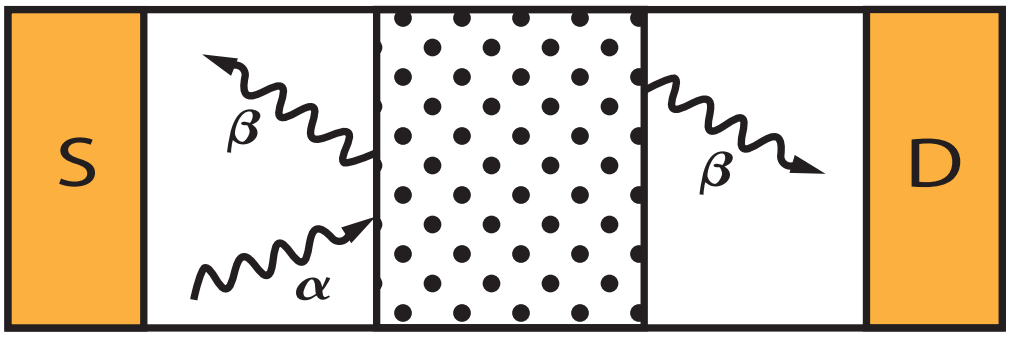

Figure 2.2: A disordered conductor. Yellow regions are souce and drain contacts. The dotted area is the scattering region. The curly arrows are incoming channels, α, and back scattered or transmitted channels β. Adapted with changes from ref. [20]

the transmission probability can be estimated to be:

$$\langle \mid t_{\alpha\beta} \mid^2 \rangle = \frac{\pi l_m}{2NL} \tag{2.2}$$

The fluctuation amplitude around the conductance mean is given by the square root of the variance: $\delta G = \sqrt{Var(G)} = \sqrt{\langle (G - \langle G \rangle)^2 \rangle}$. On evaluating δG, Lee[18] argued that the reflection probabilities, rather than the transmission probabilities, must be used. The argument is that it is a good assumption that the reflection channels are uncorrelated, since the reflection probabilities are dominated by few scattering events. On the contrary, the transmission channels will have traversed a large number of scattering sites, which increases the probability of the channels sharing scattering events. So from the relation, $\sum_{\alpha,\beta=1}^{N} \mid t_{\alpha\beta} \mid^2 = N - \sum_{\alpha,\beta=1}^{N} \mid r_{\alpha\beta} \mid^2$, it follows that:

$$\delta G = \frac{e^2}{h} \sqrt{Var(\sum_{\alpha,\beta=1}^{N} \mid r_{\alpha\beta} \mid^2)} = \frac{e^2}{h} N \sqrt{Var(\mid r_{\alpha\beta} \mid^2)} \tag{2.3}$$

Where the right hand site is true under the assumption that the reflection probabilities are uncorrelated and $N \gg 1$. The variance of the reflection probabilities, $Var(\mid r_{\alpha\beta} \mid^2) = \langle \mid r_{\alpha\beta} \mid^4 \rangle - \langle \mid r_{\alpha\beta} \mid^2 \rangle^2$, now needs evaluation. From eq. 2.2 it is recognized that:

$$\langle \mid r_{\alpha\beta} \mid^2 \rangle = (\frac{\pi l_m}{2L} + 1) \frac{1}{N} \approx \frac{1}{N}, \quad \text{for } L \gg l_m \tag{2.4}$$

The mean reflection probability is defined as a sum of the mean of different probability amplitudes $\langle \mid r_{\alpha\beta} \mid^2 \rangle = \sum_{i,j} \langle A_i A_j^* \rangle$. Where subscripts i and j are the ith and jth path respectively. Using the random phase approximation, assuming that the phases of the different paths are completely random, such that only terms where subscripts are equal to each other will survive the averaging, leads to:

$$\langle \mid r_{\alpha\beta} \mid^4 \rangle = \sum_{i,j,k,l} \langle A_i A_j^* A_k A_l^* \rangle (\delta_{ij}\delta_{kl} + \delta_{il}\delta_{jk}) = 2 \langle \mid r_{\alpha\beta} \mid^2 \rangle^2 \approx \frac{2}{N^2} \tag{2.5}$$

Finally, by combining eq. 2.4 and eq. 2.5 with eq. 2.3, we reach to the result of $\delta G \approx \frac{e^2}{h}$.

2.1.2 *Random Matrix Theory of Mesoscopic Quantum Wires*

A random matrix is a matrix whose elements are random variables. The eigenvalues $(\lambda_1....\lambda_i)$ of the random matrices are themselves random and the job is to understand the distribution of $\{\lambda_1....\lambda_i\}$ given the joint distribution of the entries. In mesoscopic systems, which are small enough that one must utilize the rules of quantum mechanics to describe them but also large enough that a statistical approach is natural[26], RMT has proven to be very fruitful[27]. The scattering matrix of a disordered wire, of which the the transmission matrix introduced in the previous section is a submatrix, is an example of a matrix that is too complicated to study and we can try to replace it with a random matrix and calculate statistical properties such as UCF. The basic idea is that all disordered quantum systems fall into a few broad classes that are distinguished by symmetries in the system[28]. In 1962 Freeman Dyson found that in a finite dimensional Hilbert space, the Hamiltonian that commutes with all symmetries must either be orthogonal, unitary or symplectic[29], corresponding to being real symmetric, complex Hermitian, or quaternionic self-dual, respectively. From these three symmetry classes the statistical properties of the energy levels can be studied by constructing probability distribution, $P(\mathcal{H})$, from a Gaussian ensemble of $N \times N$, Hermitian matrices, $\mathcal{H}$:

$$P(\mathcal{H}) = c \exp\left(-\beta \operatorname{Tr} V(\mathcal{H})\right) \tag{2.6}$$

Where $V(\mathcal{H}) \propto \mathcal{H}^2$ and c is a normalization constant. The choice of a Gaussian ensemble makes independent matrix elements. The parameter β, is the symmetry index that counts the degrees of freedom in the matrix elements. It can take the values of 1,2 or 4, depending on whether the elements are real, complex or quaternion numbers[30]. These three Gaussian ensembles are called the Gaussian orthogonal, Gaussian unitary and Gaussian symplectic ensemble (GOE, GUE and GSE), respecively. The GOE is invariant under orthogonal conjugation meaning that $O^T \mathcal{H} O = \mathcal{H}$, where O is an orthogonal matrix and models systems with time reversal symmetry (TRS). The GUE is invariant under unitary conjugation and models systems where TRS is broken. Finally, the GSE models systems with TRS but where spin rotation symmetry (SRS) is broken.

The joint probability distribution of the eigenvalues, $\{\lambda_n\}$ of eq. 2.6 is given as[27]:

$$P(\{\lambda_n\}) = c \prod_{i<j} \mid \lambda_i - \lambda_j \mid^{\beta} \prod_k \exp\left[-\beta V(\lambda_k)\right] \tag{2.7}$$

Interestingly, the first factor in eq. 2.7, which follows by the Jacobian from matrix to eigenvalue space[30], makes the eigenvalues strongly correlated and shows a repulsion between them. In fig. 2.3, a histogram of the nearest neighbour eigenvalue spacing, s, is plotted from an 8×8 GOE with $n_{samples} = 50000$ samples. This illustrates the correlation between the eigenvalues. The probability of finding two adjacent levels in the distance s is small when s is small due to the Jacobian factor, but is also small for large a spacing values due to the exponential factor.

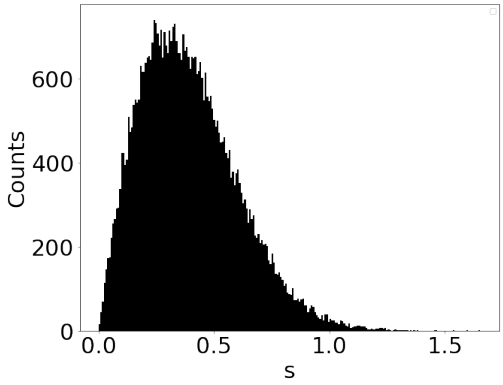

Figure 2.3: The probability density of finding two adjacent levels in the distance $s =\mid \lambda_i - \lambda_{i+1} \mid$. Here 50000 sample matrices was drawn from a 8×8 GOE. The GOE was constructed by randomly picking entries to the matrix, $\mathcal{H}_s$, from a normal distribution followed by the symmetrization: $\mathcal{H}_s = (\mathcal{H} + \mathcal{H}^{\mathcal{T}})^{0.5}$.

Using the RMT approach to study statistical properties of disorded quantum wires is restricted to the quasi-one dimensional wire ($W \ll L$) because only then, the electron motion is ergodic in the transverse direction, meaning that it has time to explore the complete phase space of the wire before it exits. This assumption breaks down in higher dimensions and RMT becomes inapplicable[26,31]. The statistics of the conductance of a quasi-one dimensional disordered wire with $l_\phi \geq L$ at $T = 0$, can be studied by drawing a random matrix distribution from the circular ensembles (COE, CUE or CSE for $\beta = 1, 2, 4$, respectively). In addition to the Gaussian ensembles the circular ensembles have to respect the unitarity of the scattering matrix elements and *circular* refer to the the eigenvalue distribution being constant on the unit circle in the complex plane[29]. The joint distribution of eigenvalues, $P(\{\tau_n\})$, for COE, CUE and CSE is given as[30]:

$$P(\{\tau_n\}) \propto \prod_{i<j} \mid \tau_i - \tau_j \mid^{\beta} \prod_k \tau_k^{-1+\frac{\beta}{2}} \tag{2.8}$$

Where $\{\tau_n\}$, can take values between 0 and 1. The product between neighboring transmission eigenvalues leads to a level repulsion similar to the repulsion of energy eigenvalues of the random Hamiltonian $\mathcal{H}$. A microscopic state of the ensemble is defined as $\rho(\tau) = \sum_n^N \delta(\tau - \tau_n)$. The average of $\rho(\tau)$ is then defined as[32]:

$$\langle \rho(\tau) \rangle = \int_0^1 \delta\tau_1 ... \int_0^1 \delta\tau_N P(\{\tau_n\}) \rho(\tau) \tag{2.9}$$

In the limit where the number of transverse channels, $N \to \infty$, it turns out that for a diffusive wire, the average distribution of transmission probabilities becomes asymmetric and bimodal[33]:

$$\langle \rho(\tau) \rangle \propto \frac{N l_m}{L} \frac{1}{\tau\sqrt{1-\tau}} \tag{2.10}$$

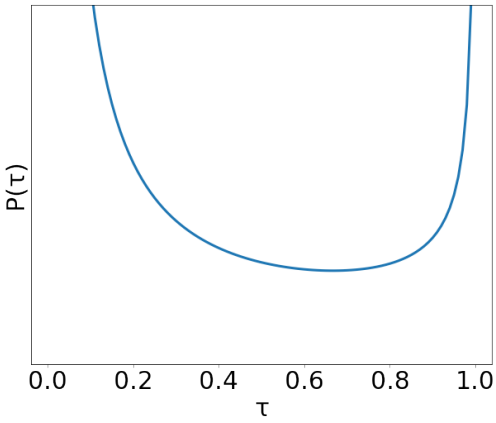

Figure 2.4: The average distribution of transmission values drawn from eq. 2.8. The eigenvalues clusters towards the limiting values and the fluctuations are small due to their mutual repulsion

Equation 2.10 is sketched in fig. 2.4. The eigenvalues are peaked near 0 and 1, corresponding to the channels being mostly either open or closed. The origin of eq. 2.10 comes from the repulsion factor in eq. 2.8, which has the effect of clustering the eigenvalues towards their limiting values. The repulsion factor also suppresses the fluctuations of the eigenvalues, since, as fig. 2.3 shows, the fluctuation of one eigenvalue is limited by the nearest neighbour values. Since $P(s) \propto s^\beta \cdot \exp(-s^2)$[27], the fluctuation depend only on the symmetry class, making them universal. From RMT, δG was calculated to be[30]:

$$\delta G_N = 0.73 \frac{e^2}{h} \frac{1}{\sqrt{\beta}} \tag{2.11}$$

2.2 Conductance Fluctuations in Quasi-1D Wires at Finite Temperature

Equation 2.11 gives the amplitude of UCF in the case of $T = 0$ with $l_\phi \geq L$ and a product of the spin-degeneracy and the valley degeneracy, $g_s \cdot g_v = 2$. However, increasing the temperature will reduce the amplitude by inducing inelastic electron-electron and electron-phonon scattering. When the l_ϕ becomes smaller than the length of the wire the conduction channels can be viewed as uncorrelated segments of length l_ϕ, which reduces the amplitude of the UCF. A thermal averaging effect, expressed by the thermal length $l_T = (\frac{\hbar D}{K_B T})^{0.5}$, similarly reduce the amplitude. The table in fig. 2.5 summarizes the value of the UCF amplitude in the regimes, $l_T, l_\phi \gg L$, $l_\phi \ll L, l_T$ and $l_T \ll l_\phi \ll L$[20]. In the intermediate regime $l_\phi \approx l_T$,

	$T=0$	$T>0$	
	$l_T, l_\phi \gg L$	$l_\phi \ll L, l_T$	$l_T \ll l_\phi \ll L$
$\delta G \times \frac{2}{g_s g_v}\beta^{1/2}$	$C\frac{e^2}{h}$	$C\frac{e^2}{h}\left(\frac{l_\phi}{L}\right)^{3/2}$	$C\frac{e^2}{h}\frac{l_T l_\phi^{1/2}}{L^{3/2}}$
C	0.73	$\sqrt{12}$	$\left(\frac{8\pi}{3}\right)^{1/2}$

Figure 2.5: The amplitude of UCF for a given β in different regimes at zero and finite temperature. Adapted from ref. [20]

.

Beenakker and van Houten[20] proposed an interpolation formula given by:

$$\delta g = \frac{g_s g_v}{2}\frac{1}{\sqrt{\beta}}\sqrt{12}\frac{e^2}{h}\left(\frac{l_\phi}{L}\right)^{\frac{3}{2}} \times \left[1+\frac{9}{2\pi}\left(\frac{l_\phi}{l_T}\right)^2\right]^{-\frac{1}{2}} \tag{2.12}$$

Finally, Zeeman splitting under applied magnetic field may lift the spin degeneracy and g_s in eq. 2.12 is replaced by $\sqrt{g_s}$.

2.3 Conductance Fluctuations in NS-Junctions

The symmetry classes behind the large scale quantum interference effects of mesoscopic materials turned the attention towards superconductors, where Altland and Zirnbauer found it appropriate to expect that novel interference mechanisms arise when these two systems are combined[28,34,35]. They found that NS-junctions are described by four different symmetry classes based on the presence or absence of TRS and SRS, similar to the conventional mesoscopic system. However, the unique feature that distinguishes the two systems is the process of Andreev reflections (AR), which puts the NS-device in a new universality class. In this section the effect of AR on UCF is summarized.

2.3.1 *Briefly on BCS Superconductivity*

Superconductivity is a correlated phase of matter emerging in certain some materials where below a certain critical temperature T_c, the electrical resistance is zero and it shows perfect diamagnetism. The demonstration of the latter, known as the Meissner effect, is the true definition of a superconductor[36].

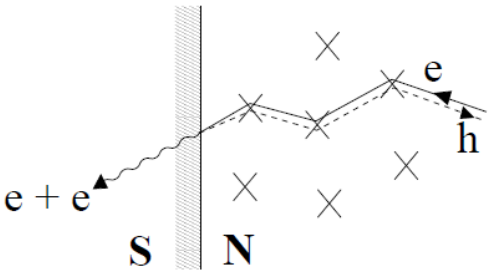

Figure 2.6: Feynman path of AR. An electron incident on an NS-junction leads to a non-zero Cooper-pair amplitude in the diffusive N-region. Adapted from ref. [35].

The microscopic behaviour leading to these observable macroscopic phenomena are well explained for most single-crystal superconductors, and many compound superconductors, by BCS (Bardeen-Cooper-Schrieffer) theory[37]. BCS theory posits that an attractive interaction between conduction electrons can lead to a correlated, zero resistance state. Typically the attractive force occurs between two electrons of opposite momentum and spin, mediated by phonons. The idea is that positive ions are attracted to an electron because of the Coulomb interaction. The dynamics of the ions are slow compared to the the dynamics of electrons, due to a much larger mass of the ions. Once the electron moves away, another electron can move into the positive charged region, before the ions have had time to relax back. Then the attraction to the same point in space can lead to the Cooper pair formation, a bosonic state, that will open a superconducting gap with an energy, Δ, around the Fermi-energy, proportional to the T_c of the superconductor, above which the superconducting phase is destroyed. Excitations, such as scattering, is forbidden if the associated energies are smaller than the size of Δ. An external magnetic field will reduce T_c until it reaches a critical magnetic field B_{crit}, above which the Cooper pairs breaks up and the superconductor turns normal. Since the electron-phonon attraction is local in space and retarded in time, it favors pairs of opposite momenta. By fermion antisymmetry, it requires that the pair state is a spin singlet[38].

2.3.2 *The Proximity Effect and the Effect of Andreev Interference on UCF*

The proximity effect is the generic name for the phenomena appearing at the NS-interface[39]. In such junctions, the N-metal shows superconducting-like properties.The normal metal does so through AR processes, where sub-gap energy electrons incident on the the superconductor can not penetrate but is instead coherently reflected as holes upon injecting Cooper pairs. As opposed to specular reflection, AR represents the process of retro-reflection, where the

incident electron is reflected back along the same path, as a hole, upon acquiring a scattering phase of $\frac{\pi}{2} - \phi$, where ϕ is the phase of the superconducting order parameter at the interface[35]. The process of AR, illustrated in 2.6, creates a non-zero Cooper-pair amplitude inside the normal region.

The energy is conserved in AR and an incident electron with the energy, ϵ, above E_F is scattered into a hole with energy,$-\epsilon$. Thus, both particles have the same excitation energy, ϵ. The superposition of a negatively charged filled state at $E_F + \epsilon$ and a positively charged empty state at $E_F - \epsilon$ is called a Bogoliubov quasi-particle[40]. In the context of RMT, the new constraint that must be put on the matrices describing the scattering processes of AR, is particle-hole symmetry, coming from the ambiguity that a Bogoliubov quasi-particle can be thougt of as a Cooper-pair either missing a particle or having an extra particle[41]. Considering the NS-device seen in fig. 2.7, at $T = 0$ and $l_\phi \gg L$, Beenakker calculated the amplitudes of the UCF[30]. The results are summarized in the following equations.

$$\delta G_{NS} = 1.51 \frac{e^2}{h} \frac{1}{\sqrt{\beta}} \approx 2\delta G_N, \quad \text{for } \beta = 1, 4 \tag{2.13}$$

$$\delta G_{NS}(\text{no TRS,SRS}) = 1.46 \frac{e^2}{h} \approx \sqrt{8}\delta G_N(\text{no TRS,SRS}) \tag{2.14}$$

Equation 2.13, states that δG doubles in an NS-junction compared to a normal wire. The enhancement by a factor of two is due to the transfer of two elementary charges in an Andreev reflection[28]. Equation 2.14, is more subtle. In fact, it only holds in the absence of a reflection

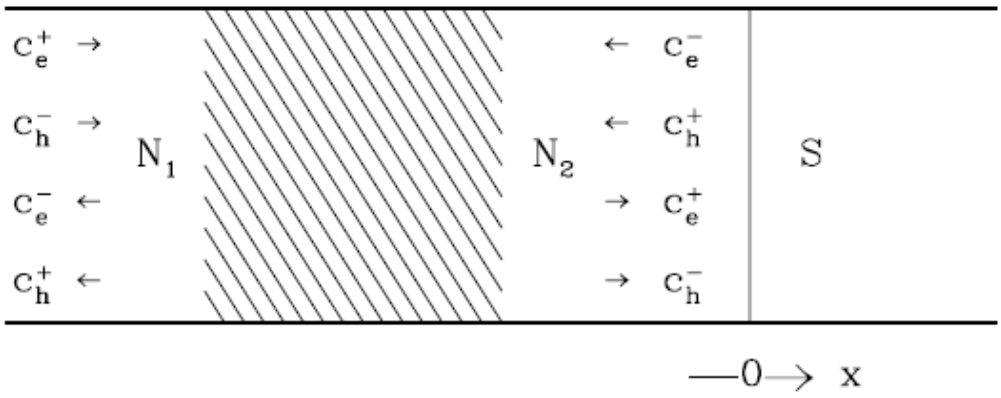

Figure 2.7: The model considered by Beenakker[30] on calculating the amplitude of UCF in an NS-device. The shaded region between the two normal leads, N_1 and N_2 is disorder. It is assumed that only AR scattering happens at the NS-interface and that the interface is ideal. Adapted from ref. [30]

symmetry in the normal part of the wire. That is, if the normal metal consists of two segments in series with specularly reflected disorder potentials, such that the first segment has a scattering matrix that is the mirror image of the second segment[30,42]. When that is not the case, $\delta G_{NS} = 2\delta G_N$. If SRS is broken, eq. 2.14 is divided by 2. The aim is to test the validity of eq. 2.13 and 2.14.

2.4 Charge Carrier Mobility in Nanowires

In this section we are concerned with scattering mechanisms that occur when the current carriers are confined within a narrow region, like a quasi-1D quantum semiconducting wire, quantified by the charge carrier mobility, μ. In this type of system μ is influenced by the location of the carriers near the oxide-semiconductor interface that introduces additional scattering mechanisms like Coulomb scattering from oxide charges and interface states, as well as surface roughness scattering[43]. From Drude theory the mean free path, l_m, is related to μ by the equation: $\mu = \frac{el_m}{m^* v_f}$, where e, m^* and v_f is the elementary charge, the effective mass and the Fermi velocity, respectively. A simple calculation, using bulk properties for InAs, shows that a $l_m = 1$ µm would require that $\mu = 23$ m^2/(Vs), far above the current best mobilities in InAs nanostructures which are on the order of ≈ 1 m^2/(Vs)[44]. This motivates a better understanding of scattering mechanisms, in order to be able to increase the value of μ and reach a ballistic transport regime over µm length scales that would enable devices where the potential landscape is determined solely by researcher-defined electrostatic gating schemes. Here follows a discussion of current state-of-art methods to extract μ from two terminal measurements. While the most reliable method probably comes from doing a Hall measurement[45], using nanostructures comes at the cost of it being essentially impossible to do four terminal measurements. The reliability of current "two terminal" methods is therefore reconsidered and the question "do we need a new method?" is asked.

2.4.1 Traditional Two-Terminal FET Mobility Extraction

The operation of a FET is controlled by an externally applied electric field realized with a gate electrode. The practical importance of μ in research level, nanoscale FETs stems from the fact that it gives a rough measure of the amount of disorder, and in the case of a density-dependent Hall mobility measurement, one can extract information about the scattering times/lengths from specific impurity sources. For NWs, mobilities have commonly been extracted either by taking the peak transconductance[43] or by fitting FET pinch-off curves[46]. Both methods start

from the Drude conductivity:

$$\sigma = ne\mu \tag{2.15}$$

Where n is the carrier density and e is the elementary charge. In the following, a system where all carriers are electrons and has a 2d carrier density n_{2d} will be considered. The carrier density is approximated by:

$$n_{2d}(V_g) = \frac{C_i \cdot V_g}{e} - n_0 \tag{2.16}$$

Where C_i is the capacitance pr. area, V_g is the gate voltage and $n_0 = \frac{C_i \cdot V_{th}}{e}$ is the critical density at the defined threshold voltage (V_{th}). Important to notice is that below n_0, the carrier density becomes comparable to the effective charged impurity density from randomly distributed charges in the 2d-transportation-layer, interfaces and the surrounding layers. The system then becomes insulating due to a percolation transition driven by the failure of screening leading to an inhomogeneous density landscape[5]. The following methods to extract μ, are only valid above the percolation regime where there is a linear relationship between n_{2d} and σ. Further, they assume μ is carrier density independent and that $V_g \gg V_{SD}$. The latter to ensure a more uniform source-drain channel charge.

Inserting eq. 2.16 into eq. 2.15 and multiply through by $\frac{W}{L}$, where W and L are the width and length of the conducting channel, respectively, leads to an expression for conductance, G, being:

$$G(V_g) = \frac{\mu C}{L^2}(V_g - V_{th}) \tag{2.17}$$

From this model the transconductance $g = \frac{\delta G}{\delta V_g}$ can be taken and if C, L are known parameters μ_{FE} is:

$$\mu_{FE} = \frac{gL^2}{C} \tag{2.18}$$

Due to the assumption that the μ_{FE} is independent of V_g, the peak value of eq. 2.18, known as the peak mobility is often reported from experiments. Albeit this is a very simple model, it is seldom very feasible in experiments since it does not account for any contact resistance or other resistances, R_s, that might be connected in series with the FET-wire. Thus, another model was suggested to account for a R_s[46]:

$$G_{2p,R_s}(V_{tg}) = \Big(R_s + \frac{L^2}{\mu C(V_g - V_{th})}\Big)^{-1} \tag{2.19}$$

Equation 2.19 is used to fit to a measured $G(V_g)$ and R_s, V_{th} and μ are the free fit parameters. To avoid complications from including the percolation regime, the start-fit-index can be chosen from an analysis of the numerical derivative of $G(V_g)$ near the transition into the linear regime. The threshold voltage in this model is defined as the intersection point with the x-axis and is estimated from the fit by extrapolation from the start-fit-index down to $G(V_g) = 0$. At high voltages the $G(V_g)$ saturates to R_s. While the model in eq. 2.19 likely results in a more accurate mobility estimation compared to the model in eq. 2.17, and has been employed in recent studies[46,47], the assumption of a constant mobility prevents one from obtaining knowledge about which scattering processes may dominate at different carrier densities[47–49]. This motivates a reconsideration of the method and we suggest a new model that will be introduced in the results chapter.

Chapter 3 The Experimental Platforms

The experimental realization of the three different experiments takes fundamentally different starting points. For the UCF-devices vapor-liquid solid growth (VLS) was used, while the growth of the devices used for the mobility experiments and Hubbard lattices was made with selective area growth (SAG).

3.1 Vapor-Liquid-Solid Growth of Superconductor/Semiconductor Hybrids

To test the hypotheses about UCF in NS-devices, it is the goal to realize a device similar to the one shown in 2.7. In particular, a quasi 1D ($W \ll L$) semiconducting wire, a nanowire(NW), in the regime of $l_\phi > L > l_m$ proximitized by a superconductor with a clean NS-interface is desirable.

3.1.1 Choice of Materials

Indium Arsenide

The high surface area to volume ratio in NWs, means that surface effects become important, and even dominant, in their influence on electronic transport[50]. The material of choice for the semiconducting part is indium arsenide (InAs). At the surface of InAs, where translational symmetry is broken the dangling bonds will reconstruct to form new surface states[51]. The surface states cause band bending such that the Fermi level is pinned above the conduction band minimum (CBM), forming a 2D-quantum well for electrons[52–54]. The electron gas formed at the surface is the reason for the absence of a Schottky barrier when a metal is deposited onto InAs, which is highly desirable since AR requires a relatively transparent interface[30]. However, since the electrons live at the surface, the quality of the NS-interface is highly dependent on details of growth processes and/or fabrication.

Aluminium

The material of choice for the superconducting part is a thin half-shell epitaxial coating of aluminium (Al) onto one end of the InAs-NW, which has shown the needed high NS-interface transparency[55,56].

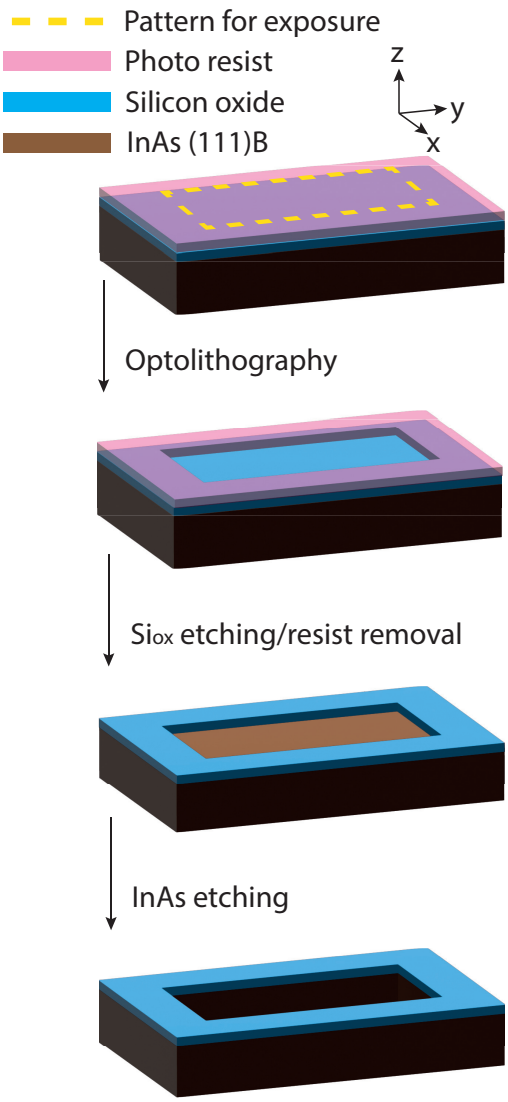

Figure 3.8: The steps leading to creation of a trench for the NW to grow from. First, a custom pattern of the trench is made and exposed with optolitography. Then the exposed SiO_x and the resist is removed. Finally, the InAs substrate is ecthed to form the trench.

3.1.2 Shadow Epitaxial in-situ Growth of Al/InAs Nanowires

Traditional epitaxial approaches to the growth of Al/InAs require post processing that chemically etches away the Al. This comes with the risk of damaging the wire. To eliminate the need of post processing, the approach of shadow epitaxial in-situ growth was used[57].

The idea of the shadow-technique is to grow the InAs nanowires in trenches. Subsequently, Al will be deposited from one side at an appropriate angle such that at a given site, wall of the trench shadows the bottom of the wire and only the top part will be half-shell coated with Al. Rough sketches of the growth process are illustrated in fig. 3.8 and 3.9, for more details I refer to ref. [57]. The first step is to pattern the trenches, where the nanowires will grow from, on an InAs $\langle 111 \rangle$B-wafer capped with a mask of 100-150 nm SiO_x. The wafer is covered in photoresist and a desired pattern is defined and then exposed with optolithography. The exposed SiO_x is then removed using wet etching techniques followed by removal of the photoresist. Next the InAs is etched, with the SiO_x pattern acting as a mask. Once the trenches are formed, droplets of gold particles are placed at the bottom using standard electron beam lithography (EBL) and metal evaporation techniques. The nanowire VLS-growth takes place in a Molecular Beam Epitaxy (MBE) system and consists of two steps. First, in an ultra high vacuum chamber, effusion cells

containing In and As are heated to the point of sublimation and the cell shutters are opened for the gaseous elements to condense on the InAS (111)B-wafer. The gold droplets act as catalysts for the crystal growth of InAs NWs and the size of the droplets determines the final thickness of the wire. In and As adsorbs to the liquefied gold droplets until the point of saturation where InAS starts crystallizing underneath the droplets and the NWs grows vertically.

On the (111)B-wafer, the NWs tend to grow in a Wurtzite structure with 6 facets[7]. Under the right conditions, a single atom layer-by-layer growth can be achieved. The second step of the growth, is radial overgrowth of InAs which promotes flatter NW facets for optimal deposition of Al[57,58]. The final step is Al metal deposition. Under UHV the substrate is transferred from the MBE chamber to a metal evaporation chamber, with a freely rotatable sample holder. Here Al is deposited at a fixed angle directed from one side of the chamber, coating 2 facets of the wires[57].

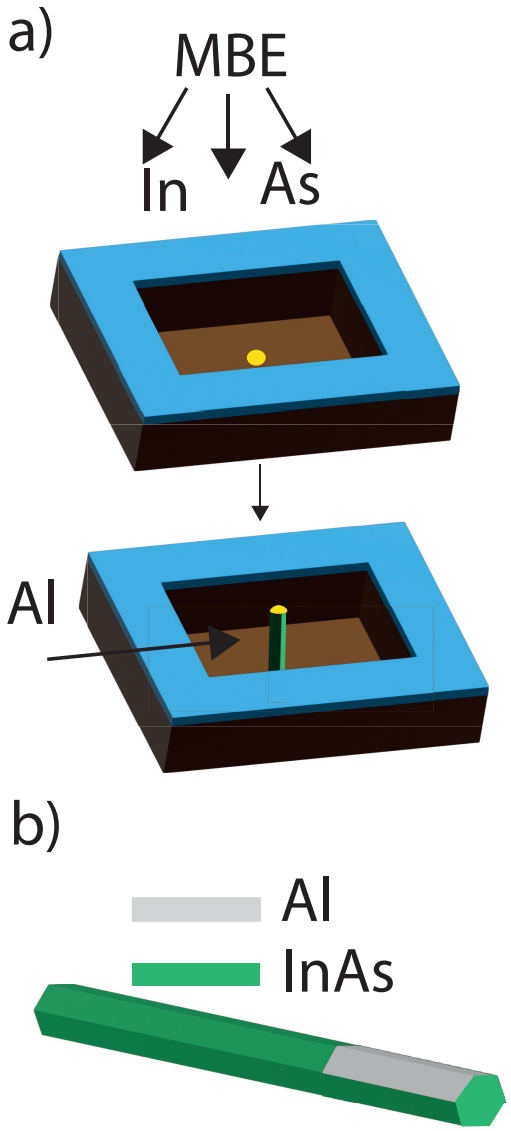

Figure 3.9: The growth steps of the NW. **a),** a gold catalyst particle is deposited in the bottom of the trench using standard EBL and metal evaporation techniques. In the MBE chamber, incident In and As atoms are absorbed by the Au droplet. At saturation, an InAs crystal forms selectively below the droplet. The substrate is then transferred to a metal evaporation chamber under UHV, where Al is deposited at an fixed angle and from one side, coating 2 facets of the top part of the wire. **b),** the NW after growth.

3.2 Selective Area Growth of Nanowires

The method of SAG uses lithographically defined openings in a mask on a crystalline substrate where structures, such as NWs or arrays of NWs, can be grown directly on the substrate[59]. This comes with a number of advantages, including control over shapes, dimensions, positions and faceting[60,61]. Further, in contrast to the VLS-method, the structures can be grown horizontally in plane of the substrate which simplifies device fabrication[44].

3.2.1 *Nanowires in a Hall Bar Geometry*

To test the applicability of eq. 5.28 in extracting μ from a two-terminal measurement, a NW in a Hall bar geometry was used (see fig.3.10b). This way, a reference Hall mobility and a two-terminal FET mobility could be extracted from the same NW and compared. The SAG of the NW was done by Daria Beznasyuk et al. and details about the growth can be found in ref. [44]. Figure 3.10a shows a schematic of the SAG steps. On an undoped GaAs(001) substrate the NW geometry was controlled by defining windows in a 10 nm silicon dioxide (SiO_2) mask layer using EBL process (see chapter 4) followed by a plasma etching technique that used excited ions of tetrafluoromethane and hydrogen to remove the SiO_2 and reveal the pattern. Native oxide that formed on the surface of the exposed trenches was removed. A challenge in this respect is to maintain a smooth surface after the oxide-removal. The standard approach is thermal annealing where a constant flux of As is applied at high temperatures to remove native oxide-layers. The disadvantage of this method is that it removes the oxides by consuming GaAs. This degrades the surface and introduces interface roughness that will lead to lower electronic performance of the NW. An alternative method is atomic hydrogen (a-H) treatment. Here a hydrogenation of the surface removes the oxides and

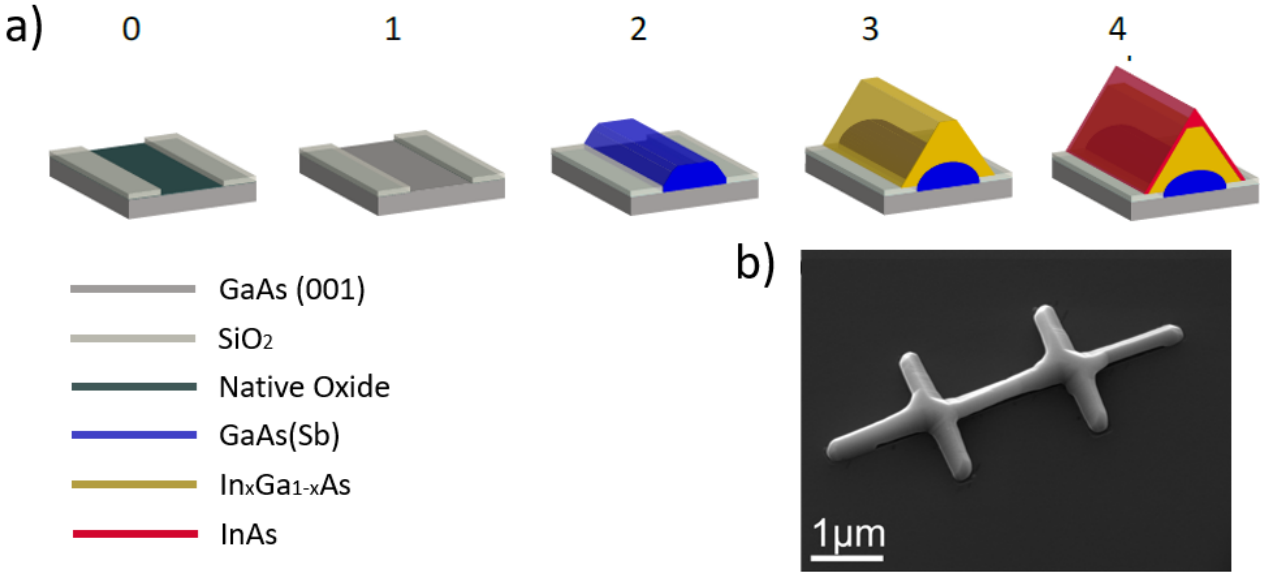

Figure 3.10: SAG NW in a Hall bar geometry. **a)** The SAG steps. *Step 0*, the growth pattern is defined in a 10 nm SiO_2 mask layer. *Step 1*, the native oxide is removed. *Step 2*, the growth of GaAs(Sb) buffer layer. *Step 3*, the growth of $In_xGa_{1-x}As$ buffer layer. *Step 4*, InAs transport channel growth. Adapted from ref. [44] **b)**, a SEM image of the finished SAG NW in a Hall geometry before fabrication of electrodes.

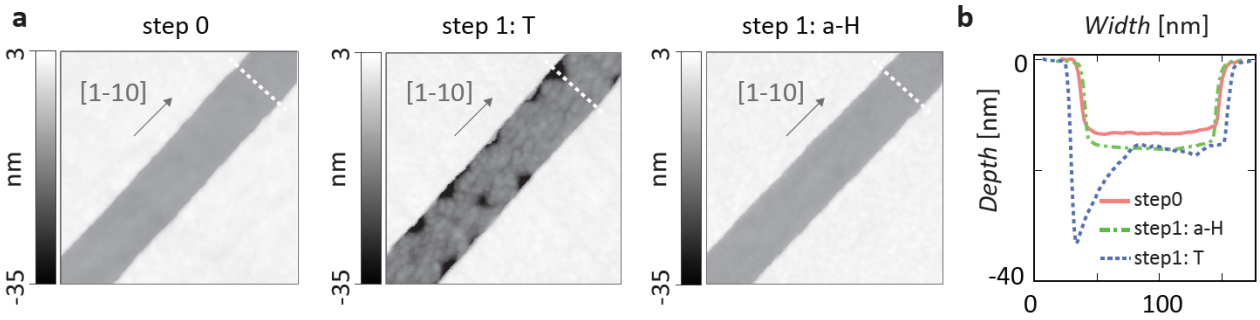

Figure 3.11: AFM analysis showing the difference between two methods to remove oxide. **a)**, *step 0*, an AFM image of the surface (dark area) before oxide removal. *step 1: T*, after oxide removal using thermal annealing clearly showing surface degradation. *step 1: a-H*, after oxide removal using a-H treatment shows a much more smooth surface. This is backed up by the AFM profile shown in **b**. The white dashed lines in **a)**indicate the position of AFM profiles. Adapted from ref. [44].

creates only water as a bi-product without consuming GaAs. Figure 3.11) shows atomic force microscopy (AFM) images comparing the two oxide removal methods. Two other challenges of the SAG-method in the context of electronic transport performance, is 1) to limit the material intermixing of InAs and GaAs and 2) to accommodate the lattice mismatch between the insulating GaAs, and the conduction layer of InAs. This was addressed by introducing buffer layers. First, a buffer layer of MBE-grown GaAs(Sb) - where Sb was used only as a surfactant to enhance the quality of the GaAs -buried the surface impurities. Then In-rich, yet still insulating $In_xGa_{1-x}As$, was grown as an intermediate buffer layer to reduce the lattice mismatch between GaAs and InAs. Finally, the InAs was grown on top of $In_xGa_{1-x}As$, resulting in an approximately triangular-shaped core-shell transport channel.

Chapter 4

Fabrication and Setup

Fabrication of new devices is a crucial part of experimental electron transport physics. After growth, the devices needs to be contacted to electrodes and possibly gate electrodes to enable control of the potential landscape in the conductor. A finished fabricated device is ready to be connected to electronic measurement tools. An overview of the devices and recipes of the fabrications can be found in appendix A2 and A3, respectively.

4.1 Fabrication of UCF-Devices

A scanning electron microscopy (SEM) image of a full fabricated device (CP1-0.70) is seen in fig. 4.12. The devices consisted of two layers of electrodes separated by the dielectric HfO_2. The first (second) layer consisted of source/drain contacts and side gates (top gates). The source/drain contacts and the gate electrodes were defined such that each nanowire consisted of a NS-device and a reference N-device. The two devices were disconnected from each other by a region that could be pinched off with a top gate (TG3) and had their own source/drain contacts (S1/D1 and S2/D2). The scattering region for both N and NS devices were designed to have approximately the same length and have their own source/drain contacts (S1/D1 and S2/D2), to facilitate direct comparison and robustly test eqs. 2.13 and 2.14. The sidegates S1-S6 were designed to tune the electron density and distribution in the relevant device segments, while the topgates T1-T4 were used to control the tunneling barriers for incoming and outgoing electrons. As shown in fig. 4.13, the devices were fabricated on a highly n-doped Si substrate, insulated from the overlaying structures by SiO_x, such that the substrate acted as a global backgate. In total, six chips were used to fabricate devices during the thesis, with the total number of devices = 16. The naming of each device holds the information of the initials of the person who fabricated it, the chip number and the length of the scattering region in microns, e.g. device *CP1-0.70* was fabricated by the author on chip number 1 and has a scattering region of 0.70 μm. A schematic overview of the fabrication steps can be seen in fig. 4.13.

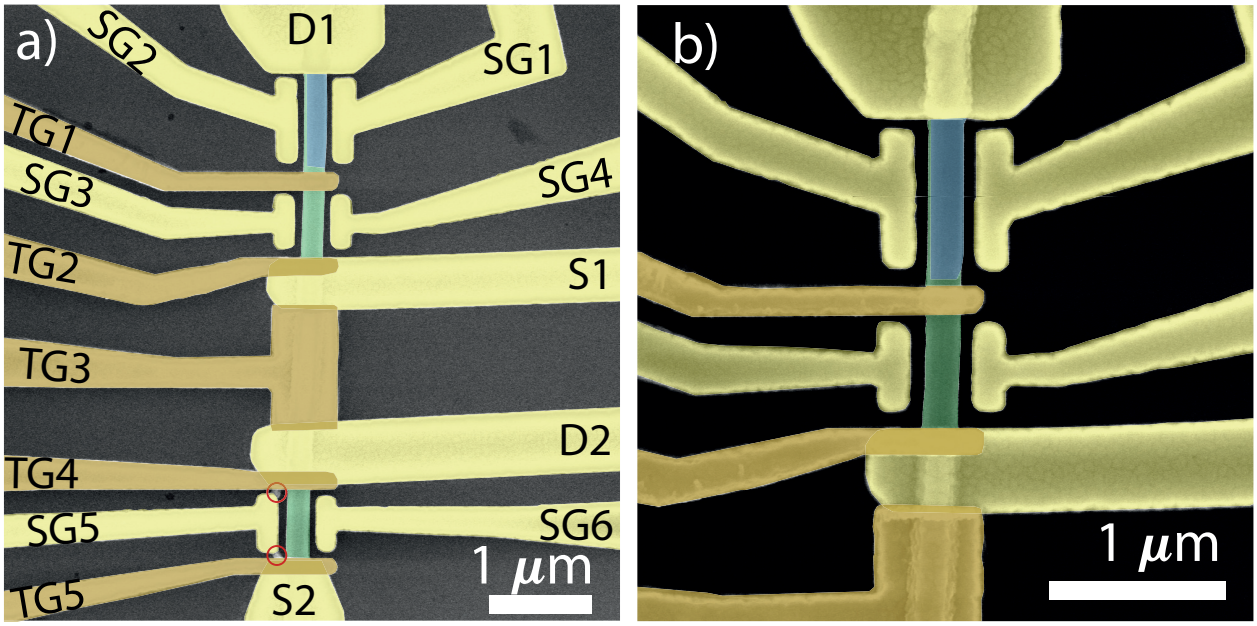

Figure 4.12: a), False-color SEM image of device CP1-0.70. Green is InAs and grey is Al. Yellow and dark yellow are both Ti/Au electrodes - the difference in color is made for clear distinction between layer 1 (yellow) and layer 2 (dark yellow) which are separated by a 15 nm thin layer of HfO_2. Layer 1 consists of source/drain contacts, side gates and the NW. Layer 2 consists of top gates. Underneath the NW, a layer of dielectric SiO_x separates the NW from a layer of n-doped Si enabling a global back gate. The wire holds two devices, a NS-device and a reference NN-device, disconnected from each other by a region that can be electronically controlled with the top gate, TG3. The red circles show, what looks like a short circuit from SG5 to D2 and S2 or it could be residual PMMA. **b)**, SEM-image of CP1-0.70 zoomed in on the NS-device.

Micromanipulation

This fabrication step requires a substrate with grown NWs and a clean "blank chip". These are substrates that the NWs are transferred to in order to make devices. The blanks used for the NS-devices are 4x4 mm chips made of n^{++}-doped Si, capped with an insulating layer of 200-500 nm SiO_x. On the surface are 48 pre-patterned gold-lines that can be used to connect to the designed electrodes seen in fig. 4.12. The gold lines are later connected to big bond pads outside the chip. The 48 lines limits the devices on each chip to maximally 3, since a device has a total of 15 electrodes.

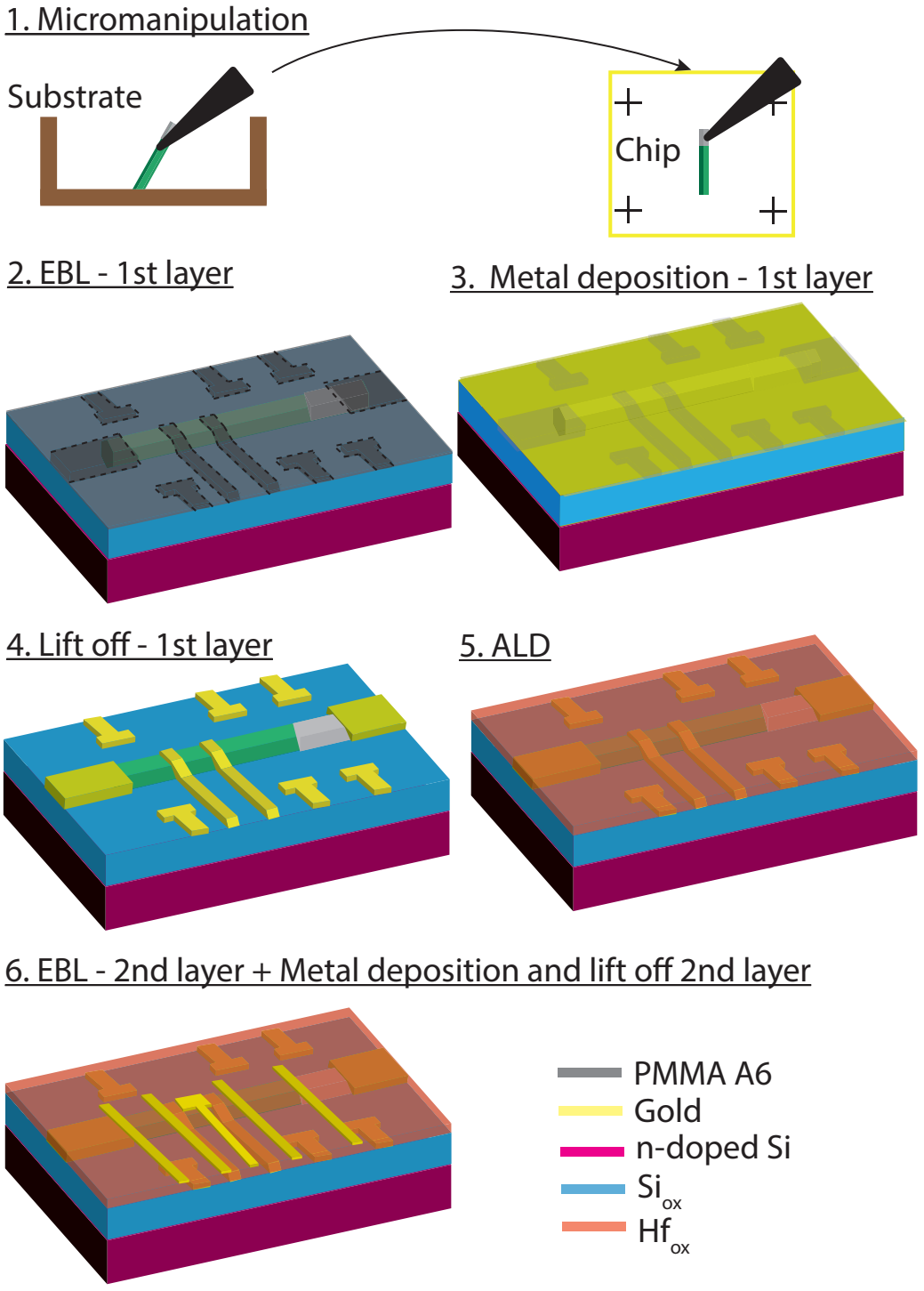

Figure 4.13: A schematic showing the fabrication steps. **Step 1**: The NW was transferred from the substrate to the chip with a $0.1\mu m$ thick needle. **Step 2**: The chip was covered in PMMA with a custom pattern defining sources/drains and side gates areas, and exposed using EBL. **Step 3**: After exposure Ti/Au was deposited on the chip. **Step 4**: Lift-off resulting in a well defined 1st-layer metal pattern. **Step 5**: ALD of 15 nm dielectric HfO_2. **Step 6**: The 2nd-layer metal pattern, defining the top gates, was made following the same procedure as in step 2-4.

The process of transferring NWs was done using a micromanipulator, sketched in fig. 4.13, step 1. A 100 nm radius needle, controlled by an Eppendorf TransferMan, was used under an OM. The NW attaches to the needle - and subsequently to the substrate - by van der Waals forces. Once they were picked up and transferred to the chip a "poking"-technique was used to straighten them and align them all with each other. It was possible to identify the Al-part under a high-quality OM (see fig. 4.14).

Electron Beam Lithography

The deposition of gates and contacts were enabled by a lithography process that use a thin, patternable polymeric film known as 'resist'. Figure 4.13 step 2 shows the basic principle; small windows for a substrate to be deposited into is defined in a mask of resist on the chip using lithography. The sizes of the windows can be down to the nanoscale.

First, a film of an organic polymer, Poly-methyl-methacrylate (PMMA 6%), dissolved in anisole known as "resist" was spin-cast onto the chip with a frequency of 4000 rpm to create a uniform thin layer. After spin-cast, the chip was baked on a hot plate to evaporate the solvent.

The patterned windows in the resist are custom designed with CAD software. PMMA is a positive tone resist, meaning the exposed areas are soluble. For exposure, EBL with an Elionix using acceleration voltages of up to 100kV was carried out. The structure of the Elionix is that of an SEM and consists of a electron beam column, which is aligned with the writefield such that the sample is in a constant position relative to the SEM aperture and

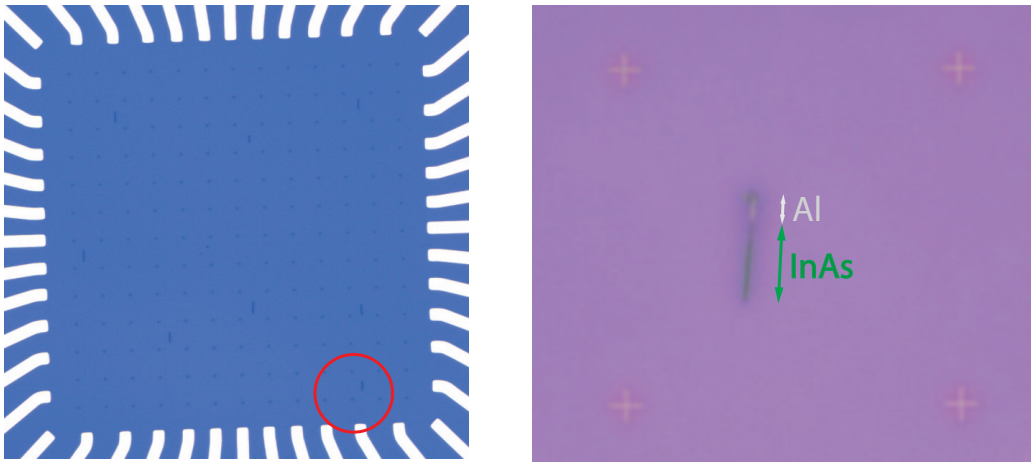

Figure 4.14: Optical images of the chip after micromanipulation. **Left**, an overview image of the chip, where a total of 8 wires were picked up. The 48 gold lines are seen along the edges. **Right**, A close-up of the NW marked with a red circle on the left figure. The Al and InAs are clearly distinguishable.

the beam is deflected to trace out the custom-designed patterns and features down to a few nanometers precision can be patterned. An area dose and a beam current is chosen to define the time that a given area is being exposed. If the ratio between the dose and the current is to high there is a risk of overexposing the resist. Using positive tone resist with EBL tends to expose the underside of the resist outside the region defined by the beam due to some of the primary electrons, which are penetrating deep into the resist, are generating secondary electron from inelastic scattering processes. A proximity effect correction is activated in the software which lowers the dose at beam sites with a lot of neighbouring beam sites to reduce the unwanted effect from secondary electrons.

The chip was developed in methyl isobutyl ketone (MIBK) and IPA, with the ratio 1:3 MIBK:IPA, to dissolve the exposed areas and afterwards ashed with an oxygen plasma to remove any residual organic material. Immersion in MIBK for too long might be the cause of pattern broadening. Together with the the risk of overexposure and wire displacement a safety distance of at least 100 nm between features in the same layer was used. Nevertheless, as seen in fig.4.15 some samples suffered from one or more of those errors.

Argon Milling and Metal Deposition

To prevent insulating surface oxides before making contact, argon milling that toos place inside an AJA evaporation chamber immediately before metal deposition was done in the same UHV chamber. The milling process was used to remove loosely bound surface impurities by bombarding the NWs with the noble gas argon. Afterwards, Ti was evaporated with an

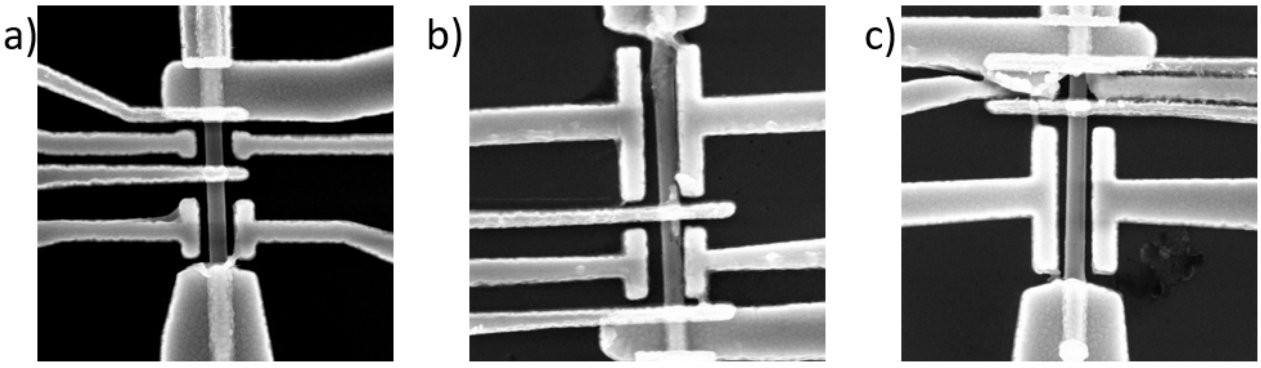

Figure 4.15: SEM images of three examples of fabrication errors. **a)**, device CP1-0.50. The side gates should have sharp corners, but the roundness suggest either overexposure or an overdeveloped sample. **b)**, device CP2-0.85. This wire has been slightly displaced to the right before exposure and the deposited metal is misaligned. **b)**, device CP2-0.35. Here it looks like the lift-off went wrong. This was the sample with the smallest scattering region, meaning that a lot of features were closely packed, making the fabrication more error prone.

electron beam to fill up the vacuum chamber and deposit on the chip. Only a thin layer was deposited on the chip to help a subsequent layer of evaporated Au stick to the surface of the chip. The thickness of the deposited Au was chosen to be greater than the thickness of the wire but smaller than the thickness of the resist. If the Au-layer is too thin it might not cover the NW from all sides and if it is too thick it might cause problems during the step known as "lift-off". In this step the resist layer and the metal regions not in contact with the substrate was removed with a solvent. For lift-off to be effective, the solvent must be able to access the resist layer underneath the metal. A handy trick to successfully achieve access, is to cover the edges of the chip in foil right before loading it into the AJA chamber to prevent the metal from being deposited here.

Atomic layer deposition

To enable the patterning of top gates a 15 nm insulating layer of HfO_2 was deposited by atomic layer deposition. This process ensures a perfectly uniform layer of dielectric allowing for ultimate thickness control. The choice of HfO_2 as the insulator was based on considerations about its relatively high dielectric constant compared to e.g. SiO_x, that enables a thicker layer while keeping the same capacitance and reducing the risk of leakage currents.

4.2 Fabrication of Hall Bar/FET-devices

An advantage of the SAG method is that it excludes the necessity to transfer wires from the growth substrate to a fabrication substrate. This means that fabrication of the Hall bar devices for the mobility measurements, fabricated by Jung-Hyun Kang, followed the same steps as in fig. 4.13 except for step 1. Details of the recipe is found in ref. [44]. In total, four fabricated Hall bar devices were used in this thesis.

A post-fabrication SEM image is shown in fig. 4.16. The Hall bar geometry of the NW allowed for easier contacting of the voltage probes, that are going to be used for measuring the transverse and longitudinal voltage drop across the InAs channel. A top gate spanning from source-drain and separated from the contacts and the NW by 15 nm of dielectric HfO_2, was used to control the carrier density.

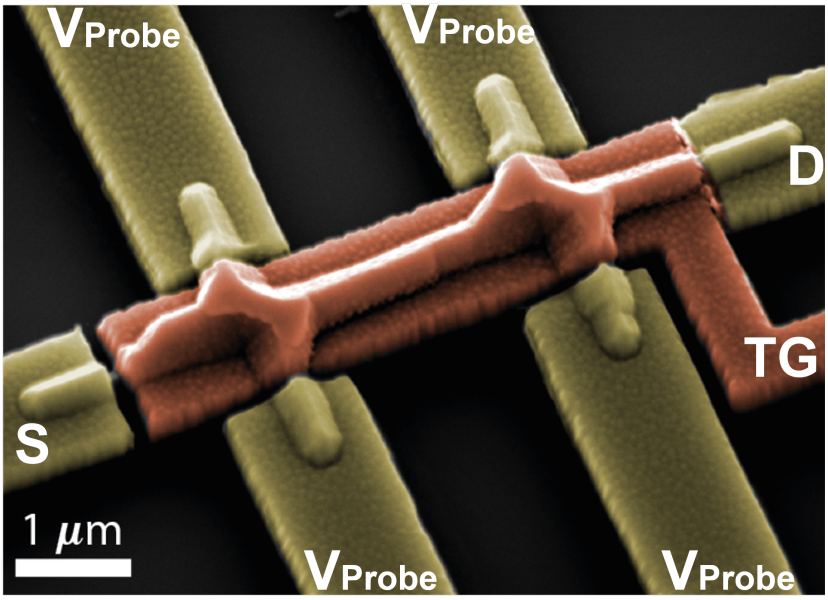

Figure 4.16: False color SEM image of a fabricated SAG Hall bar. Three of the four voltage probes (yellow) were used for transverse and longitudinal voltage drop measurements. The top gate (orange) spanning from source-drain (yellow) was used to control the carrier density. All electrodes consist of with Ti/Au.

4.3 Measurement Methods

All electrical set-ups and experiments proceeded along the same basic lines. A source-drain voltage difference V_{sd} was applied and a gate voltage, V_g, was used to modulate the current I_{sd} through the channel. Standard low frequency ($\approx$ 200 Hz) lock-in techniques were used, allowing for more accurate measurements of the differential conductance by measuring the current response to a small voltage excitation. Whenever the magnetic properties was of interest, a 6-1-1 T vector magnet was activated. The electron transport measurements were conducted in an Oxford Triton dilution refrigerator with a base temperature $\approx$15 mK. In the following, the tools that were used to perform coherent electron transport experiments and the setup of the electronic circuits are discussed.

4.3.1 The Triton 200/400 Helium Dilution Refrigerator

One thing that all the experiments have in common is that the phenomena under investigation are easiest observable if scattering events from phonon interactions are minimized or eliminated. While the NS devices by their nature require a temperature, $T < T_c$ $\approx$1-2 K to exist as superconductors, the semiconductor devices require millikelvin temperatures for us to be able to resolve UCF, elastic scattering mechanisms and strong correlations. The key word here is "phase coherent waves", which can be described by the wave nature of quantum particles. The wavefunctions of all particles evolve according to the Schrödinger equation, which maps all the possible histories of the quantum system. The probability for a particle to propagate from one space-time to another can be described by summing up all the possible paths leading to the final state. This idea is formulated in Richard Feynman's path integrals[62] and simplest visualized by the double-slit experiment. For this idea to work; for QI to be observable, the different branches of the possible paths must remain coherent, meaning their waves must match in frequency, have the same shape and a constant offset between their peaks and troughs. On the other hand, if decoherence occurs, the coherent phase relation is destroyed, causing the loss of information about the relative phase and the ability to see interference patterns. Decoherence happens when the particle picks up random phases along its way to the final state. The length over which the waves remain coherent is inversely proportional to the temperature, emphasizing the need to cool the samples before measurements. The Triton 200/400 Helium Dilution Refrigerator[63] (cryostat) exploits the properties of a ^{3}He-^{4}He mixture at cryogenic temperatures to cool samples down to millikelvin. Figure 4.17a shows a ^{3}He-^{4}He phase diagram. Below T= 2.2 K ^{4}He Bose-Einstein condensates into a superfluid, while ^{3}He remains

in the fermionic state until much lower temperatures, that are not accessed with this system. Following the lambda line, that separates the normalfluid phase from the superfluid phase, it is seen that adding an increasing amount of ^{3}He to the ^{4}He results in a decreasing critical temperature of the superfluid. At a sufficient ^{3}He-concentration, a continuous temperature decrease will separate the mixture in two phases, a normalfluid ^{3}He-rich (concentrated) phase and a superfluid ^{3}He-poor (diluted) phase, with the less dense concentrated phase floating on top. A stronger binding energy between^{3}He-^{4}He atoms than between ^{3}He-^{3}He atoms results in an energy decrease by letting ^{3}He atoms enter the diluted phase until an equilibrium is reached. For $T \to 0$, the equilibrium concentration of the diluted phase approaches 6.6%.[64]. An image of the inside of the cryostat is shown in fig. 4.17b. The top plate at room temperature, is used to attach the vacuum can (not shown), separating the inside vacuum chamber from the outside. The vacuum chamber pressure is kept at 10^{-5} mbar to prevent thermal exchange with the environment and also contains several layers of radiation shielding. Outside is a valve plate, connecting the mixture tank to the condensing- and pre-cool line. The cryostat is designed with several cooling stages that initially cools the incoming mixture down below the triple point in the phase diagram before a pumping system pulls ^{3}He atoms across the phase boundary to obtain further cooling.

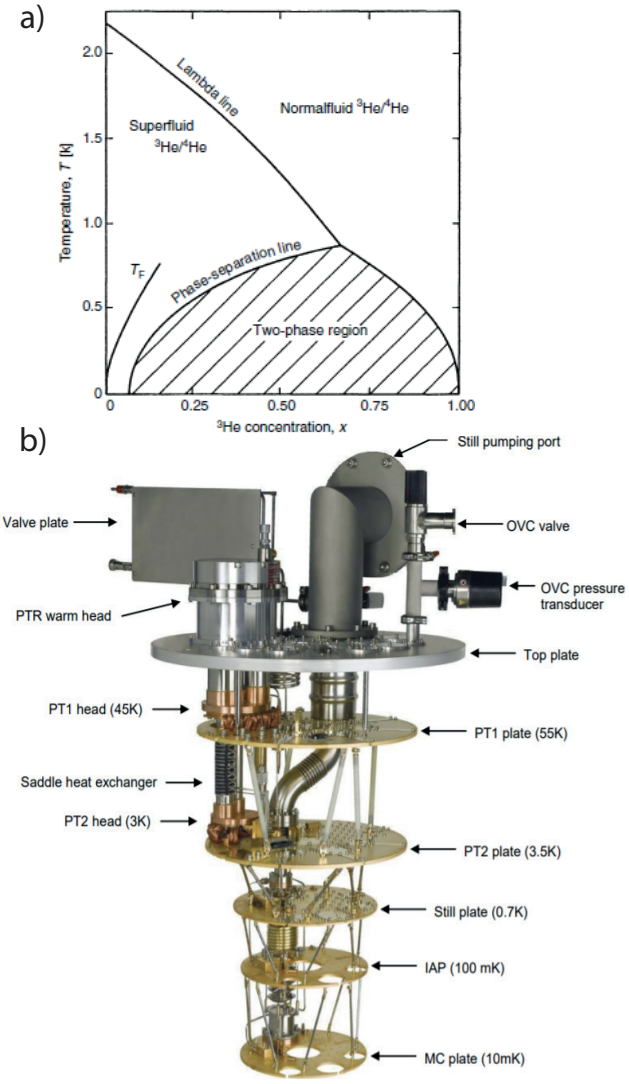

Figure 4.17: **a**, the phase diagram of ^{3}He-^{4}He mixture. Adapted from ref. [64]. **b**, the Triton 200/400 helium dilution refrigerator shown without the vacuum cans, thermal shields and magnet. Adapted from ref. [63]

Figure 4.18 shows a schematic of the logic of the cryostat. Before cooling with the mixture can begin it is cooled down in a pre-cool loop (purple pipes) provided by a continuously running pulse-tube cooler that uses ^{4}He to cool the PT2 plate to $\approx$ 4 K. When the mixture is below 10 K it is redirected into the much thinner condensing lines (black pipes) for cooling to 'base'

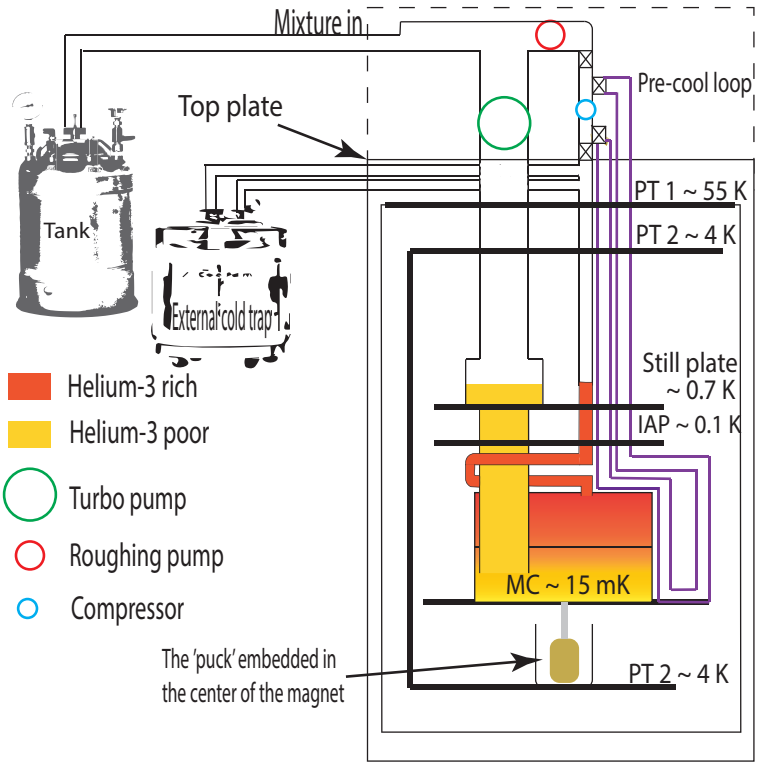

Figure 4.18: A simplified schematic of the Triton 200/400 Helium Dilution Refrigerator. The parts are not drawn to scale.

temperature. Here, the mixture is forced past PT1 and PT2, where pumping on the mixture on the other side lowers the temperature to 0.7 K, i.e. below the triple point where the mixture separates into two phases. The volume of the mixture and the gas lines in the fridge are chosen to ensure the phase boundary occurs in a small chamber, the mixing chamber, and that the phase boundary between liquid and gas occurs in the still. Therefore, attaching a plate to the MC ensures the sample can be brought into thermal contact with the mixture phase boundary. Maintaining a constant mixture volume is important, thus the outgoing mixture from the still must be returned via the condensing circuit, and PT1, PT2, etc. Since PT2 is at $T = 4$ K - two orders of magnitude higher than 15 mK - heat exchangers are used at the still and below so that the outgoing, cold mixture cools the incoming, warm mixture. The intermediate anchoring plate (IAP) is attached where the mixture reaches approx 100 mK to enable users to mount and thermalise electronics, etc. External and internal(not shown) cold traps of activated charcoal immersed in a liquid nitrogen vacuum dewar, either freezes contaminants on the cold surfaces or adsorb them to the charcoal. The "puck" which contains the sample is located underneath in thermal contact with the MC. Around the puck is the magnet, which is in thermal contact with PT2, consisting of a superconducting coil with

$T_c \approx 5$ K.

4.3.2 Loading a Device

The type of cryostat used in this thesis enables unloading/loading devices without having to warm up the cryostat first. The loading procedure of a room temperature puck into a cold cryostat is as follows: First, all the mixture is collected in the mixture tank to avoid heating of the mixture and possible overpressure when a new sample is loaded. Second, a new puck containing a sample is mounted to a loading stick (see fig. 4.19). The sample chip has been glued onto a daughterboard containing bond pads which has been electrically connected to the bond pads on the sample chip with a thin Al thread. Then the daughterboard is screwed onto one a motherboard inside the puck, with electrical connectors mounted to both the top and bottom. While the connectors on the top connect to the wiring inside the cryostat, the bottom ones enable electronic connection to the loading stick. A load lock system enables attachment from the bottom of the cryostat followed by evacuation, using a turbopump. Once the load lock has reached ultra high vacuum comparable to that inside the cryostat vacuum can, a gate valve is opened and the puck inserted such that it mates with the cold finger mounted beneath the MC plate.

4.3.3 The Measurement Setup

A total of 48 DC lines are connected from the sample to the top of the cryostat where they connect to break-out-boxes (BoB) that are placed right next to the cryostat. From here, BNC coaxial cables are used to insert suitable measurement tools into the electronic circuit. A

Figure 4.19: Left, a picture of the puck. **Middle,** a picture of the puck without the shield. The daughterboard containing the sample is mounted onto the motherboard, which has electrical connectors to both the bottom and the top of the puck, ensuring electrical connection to both the wiring inside the cryostat and the loading stick. **Right**, a picture of the loading stick with the puck mounted onto it. The loading stick is grounded to minimize the risk of blowing up a device, while attached to the puck.

diagram of the circuit that was used as a basis for the two terminal measurements is shown in fig. 4.20. In the case of the SAG Hall bar in fig. 4.16, voltmeters were added to measure longitudinal and transverse voltage in a four terminal setup, but was otherwise identical to the setup in fig. 4.20. A typical current through the devices is on the order of a nano ampere or smaller and therefore even small noises will bury the signal. To maximize the signal-to-noise (S/N)-ratio a SR830 lock-in amplifier, referred to as the "lock-in" from now, was used[65]. The lock-in first generates a sinusoidal excitation , V_{AC}, with a fixed frequency, ω_0. In general the returning signal will contain ω_0 plus noise at other frequencies so the lock-in uses phase sensitive detection (PSD) by first amplifying and multiplying the returning signal with a 'reference' copy of the output signal. The result of this is a sum of two AC signals, one with the sum of ω_0 and one with the difference of ω_0. The multiplied waves are then passed through a low-pass filter that effectively takes the average of the product of the waves that, according to Fourier's theorem, ensures that only signals with frequencies exactly equal to the reference frequency survive. The averaging time constant can be set manually after considering the trade-off between too long total measurement time and a higher S/N-ratio. The lock-in leaves a DC component proportional to the voltage of the signal V_{sig}. If the reference and the signal are in phase with each other, V_{sig} is given from this single component. If a capacitive or inductive coupling is present in the circuitry and the phases are slightly mismatched, the lock-in uses a second PSD that is 90 degrees out of phase from the first one, resulting in two components called the X and Y. From taking the Pythagorean sum of X and Y, V_{sig} is given.

The efficient attenuation of noise signals provided by the lock-in enables to do more accurate

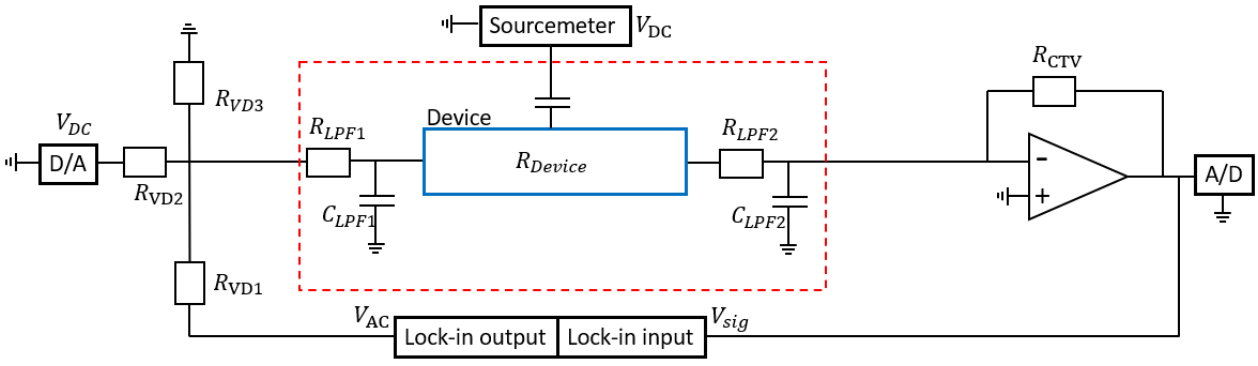

Figure 4.20: The setup of the circuit used for measuring the devices. A DC and AC signal was generated by the D/A converter and lock-in, respectively, and added together by a VD. LPF's residing inside the cryostat, demarked by the red dashed rectangle, filtered out high frequency noise. Sourcemeters were used to apply a voltage to the gate electrodes and change the electronic potential landscape of the device. A CTV was used to convert the current into a voltage and amplify the input signal, that was then measured by the lock-in and the A/D converter.

measurements of the differential conductance by measuring the current response to a small voltage excitation. Since the lock-in measures a voltage, the current through the device has to be converted into a voltage using an current-to-voltage converter (CTV). The CTV works by creating a virtual ground at the node between R_{in} (the total resistance before the CTV) and R_{CTV} and then use the relation: $V_{out} = -V_{in} \cdot \frac{R_{CTV}}{R_{in}} = -I_{sd} \cdot R_{CTV}$ to output a voltage. The measured output voltage enables extraction of the current by knowing the gain of the CTV. The input voltage can in general be a combination of the AC-signal from the lock-in and a DC-signal sourced by a digital-to-analog converter (D/A) - that is interfacing with the computer software - if a bias voltage is wanted. The DC-signal is measured by the reverse process of converting the signal from analog to digital (A/D). The small AC-signal is added to the total input voltage by a voltage divider (VD) box, to be able resolve the electron energies which at the base temperature of the cryostat are on the order of μV. High frequency noise, e.g. warm electrons entering the cryostat from the BoB or background radiation, is impeded by low-pass filters (LPF) connected in series to the device by letting it through a grounded capacitor. Finally, sourcemeters that can simultaneously apply a voltage and measure a current are connected to the gate electrodes on the device. Before any measurements start it is important to test that currents are not leaking into a gate, since gates have only a capacitive coupling to the device. Gate leakage can also be caused by electrostatic breakdown and it

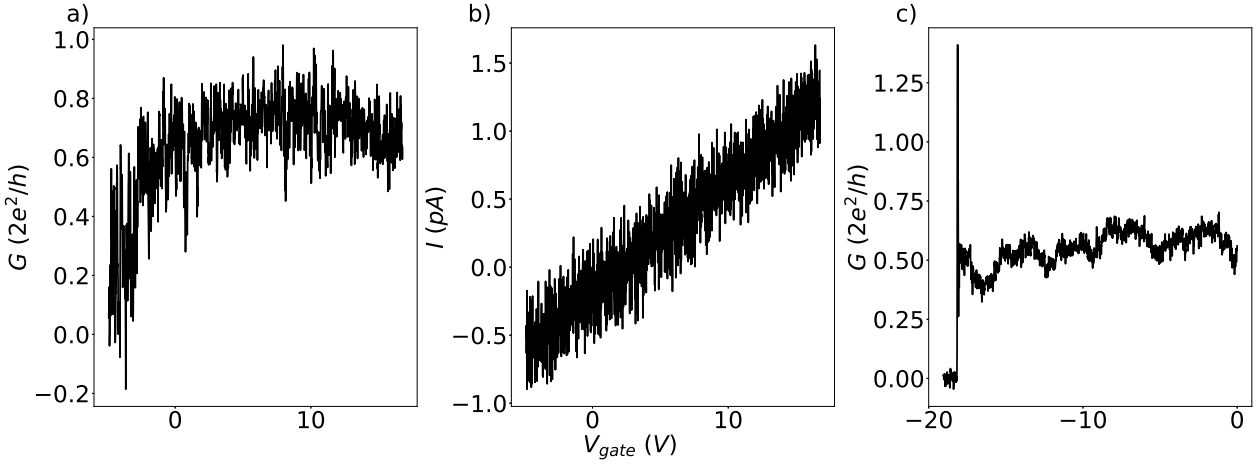

Figure 4.21: Testing gates on device CP1-0.50. **a,** A conductance measurement as a function of a gate voltage providing information about the effectiveness of the particular gate. This is always done for all the gates involved before beginning the experiments. **b,** The gate current is measured while applying the voltage to check for leakage currents. The measurement is watched in real time and by any sign of exponential behavior the measurement is aborted immediately. Here no sign of leakage is observed. **c,** Accidents happen, here a too large voltage was applied and around $-18V$ the device irreversibly stopped functioning, possibly due to a leakage current that blew up the wire.

is therefore important to carefully find a safe voltage range for the gate to function within. The test of gate leakage is done by sweeping the gate voltage within an expected range and measure the current. An example of gate testing for device CP1-0.50, is displayed in fig. 4.21a&b. The current measurement is observed in real time and by any sign of non-linear behavior, the measurement is aborted and the particular gate voltage range can not be used. Figure 4.21b shows no sign of leakage currents in this particular gate range. However, in fig. 4.21c a mistake was made such that the current was not measured while sweeping the gate. It so happened that a too large voltage was accidentally applied to a side gate with the result of a dead device.

Reducing the Signal-to-Noise Ratio

Noise is important because it can have undesirable effects on the measurements that obscures the real signal from the device. For the UCF measurement we paid special attention to the noise-level, since random noise could potentially hide the symmetry dependent differences in δG. We used the lock-in technique to reduce noise - as already explained. However, since we used a finite time constant of 100 ms, we had to consider other sources to reduce the noise-effects i.e. chosen frequency and the excitation voltage.

The typical electron temperature at base temperature of the type of cryostat that we used is $\approx$ 30 mK and the broadening of the Fermi function is therefore, $3K_BT = 8$ μeV. Adding to this that the device does not see the entire applied voltage but a value that is reduced by the factor $\frac{R_{device}}{R_{series}}$, gives us information about which excitation voltage to use. To gain additional information specifically targeting the UCF measurements, the conductance as a function a gate voltage was measured for different values of the excitation voltage and is plotted fig.

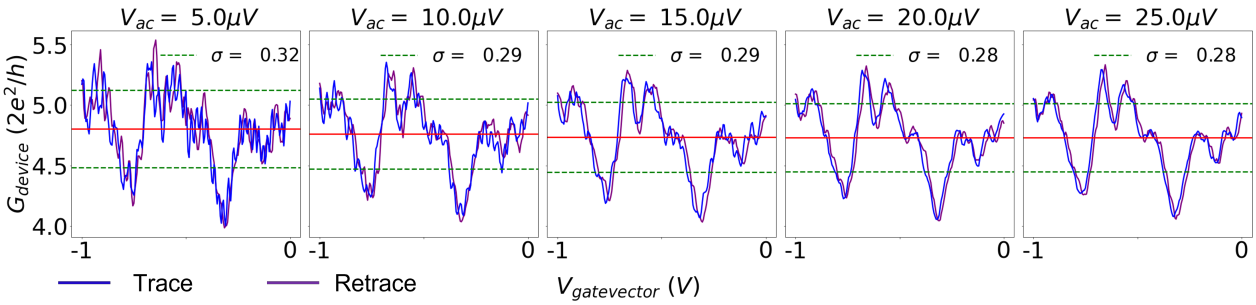

Figure 4.22: Investigating S/N-ratio using different excitation voltages. At excitation below 20 µV, the random noise adds significantly to the UCF. By comparison of the trace (blue) and retrace (retrace) it is seen that the averaging effect at higher excitation reduce the noise and the uncertainty saturates at 20 µV, which was then chosen for the UCF-experiments.

4.22. The data of the trace and retrace makes it possible to separate UCF from noise. By calculating the standard deviation, σ, it is seen that for low excitation voltages the noise adds significantly to the uncertainty and artificially inflates the UCF. As the excitation voltage is increased, the noise is averaged out and around 20 µV the uncertainty saturates, meaning that the UCF that is left is real and it is safe to choose this excitation voltage for the experiments.

To probe the effect of a chosen frequency on the noise level we measured the conductance as a function of time for frequencies between 277 Hz - 283 Hz, as shown in fig. 4.23, left. The standard deviation was plotted as a function of the frequencies (right). The frequency with the lowest noise level was found to be 281.3 Hz. However, this value could change from day-to-day, so the measurement was done frequently and the frequency changed accordingly.

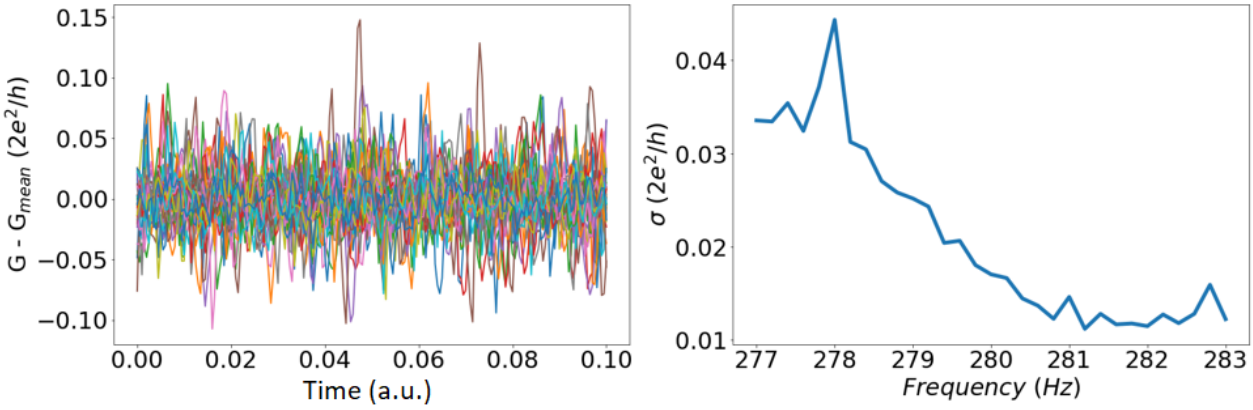

Figure 4.23: Probing the noise level as a function of frequency. **Left,** conductance was measured as a function of time at frequencies ranging from 277-283 Hz. Here the mean conductance is subtracted. **Right,** The standard deviation of the conductance as a function of frequency. The quietest region was 281.3 Hz.

Chapter 5

Measurements and Results

Electronic measurements carried out on devices are presented and the results are analyzed in this chapter. The first section deals with the experiments on UCF-devices while the second section discusses mobility-extraction of FET-devices.

5.1 Universal Conductance Fluctuations

Due to fabrication issues, out of a total of 16 UCF-devices that were fabricated during this thesis, only 2 turned out to have the functionality required for the planned experiments as presented in the following section. Various factors could be the reason for non-functioning devices. Some of them are mentioned in a previous chapter, but a common factor is the author's lack of experience in making devices. Another reason is the extreme sensitivity of the device to electrical discharge and unfortunately, the measurements started with blowing up a device as shown in fig. 4.21c. A SEM+optical-image of the one device that was left is shown in fig. 5.24. The data of this device is now presented.

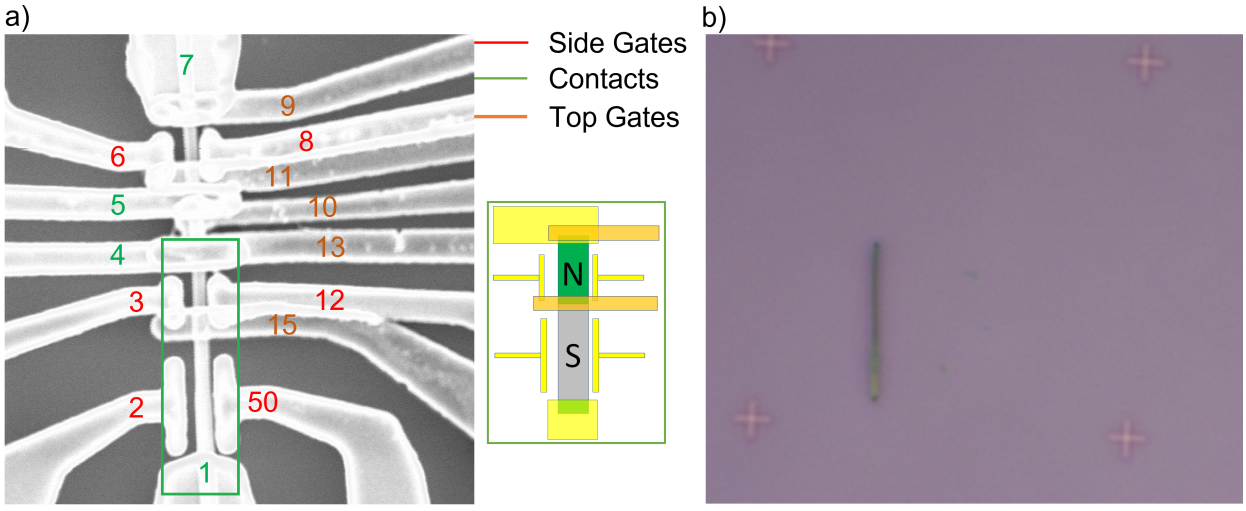

Figure 5.24: Images of CP5-0.75. **a),** A SEM-image of the device. The numbers indicate the BoB-lines. The reference wire from 5-7 was floated while measuring the NS-device from 1-4. The inset shows a schematic of the NS-device defined by the green box. **b),** An optical image of the naked wire on a blank chip before fabrication. The Al is recognized as the bright region of the bottom part.

5.1.1 Characterization of the NS-Device

Gates

We focus first on the effectiveness of the gates in the NS-device shown in the lower part of fig. 5.24a and schematized in the inset next to it. This devices had four side gates, (3, 12, 2 and 50). Due to lack of time, only the side gates located on the N-part of the wire, 3 and 12, were used. Figure 5.25a shows the conductance vs V_{Sg3} and V_{Sg12}. A schematic of the device setup used for this measurement is shown in 5.25c. The red dashed line follows approximately equipotential lines and the slope of this line can be used to find the relative electrostatic coupling between the side gates. From this it was inferred that side gate 12 was more electrostatically coupled to the devices. This makes sense judged from the SEM image in fig. 5.24a, since 12 is much closer to the wire than 3. The black vector shown in fig. 5.24a, is approximately perpendicular to the red dashed line. We chose to sweep along the direction of this vector to change the chemical potential of the device and measure the UCF. An example of such a sweep, from ± 5 V on gate 3 through the origin in fig. 5.24a, is shown in fig. 5.24b. Here the residual conductance, after subtracting a fit to a 4th degree polynomial, is plotted. We see aperiodic fluctuations which are attributed to UCF.

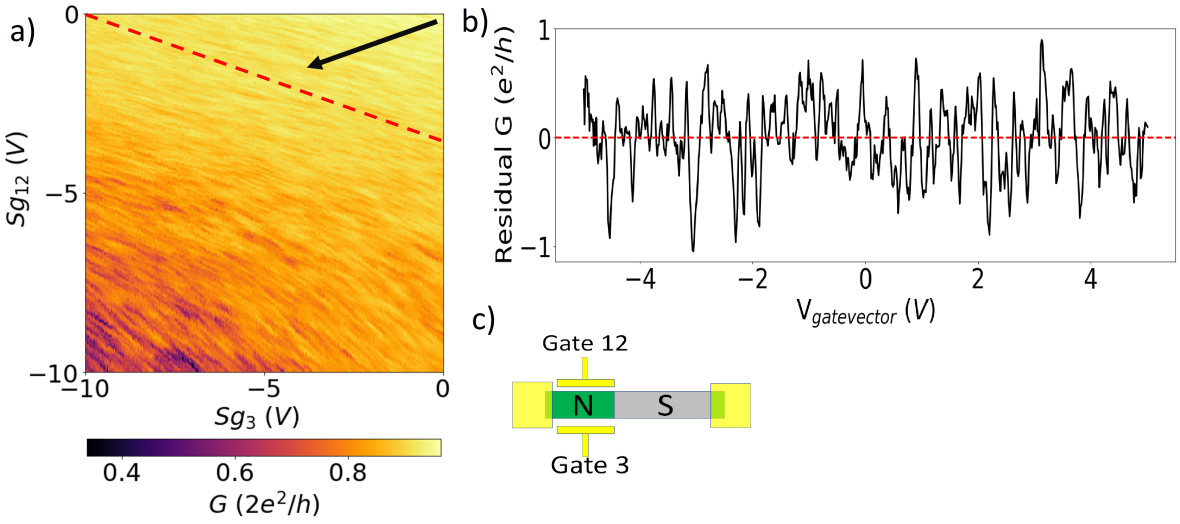

Figure 5.25: The side gates of the NS-device. **a,** A gate-gate map of the conductance for the side gate 12 and 3. The red dashed line indicates the relative electrostatic coupling of the gates to the wire. The black arrow show the vector that was chosen to be swept along for the UCF measurements. **b,** The residual conductance of a gate trace along the direction black arrow in a. The residuals were found by subtracting a 4th degree polynomial to the conductance. **c,** A schematic of the device setup used to collect the data in a.

Next, the effects of the pincher gates 13 and 15 were tested. Gate 13 showed, for all practical purposes, zero response which meant that we only had one pincher gate. This gate was used to reduce the tunnel barrier at the NS interface to avoid charging effects. In fig. 5.26a, a pinch-off-to-saturation curve of the conductance vs. gate no. 15 is shown. When all gates were at 0 V the device was already far from pinch-off but it was possible to gain $\approx$ 25 % in conductance, when increasing the pincher to 1.5 V. A saturation was reached at this

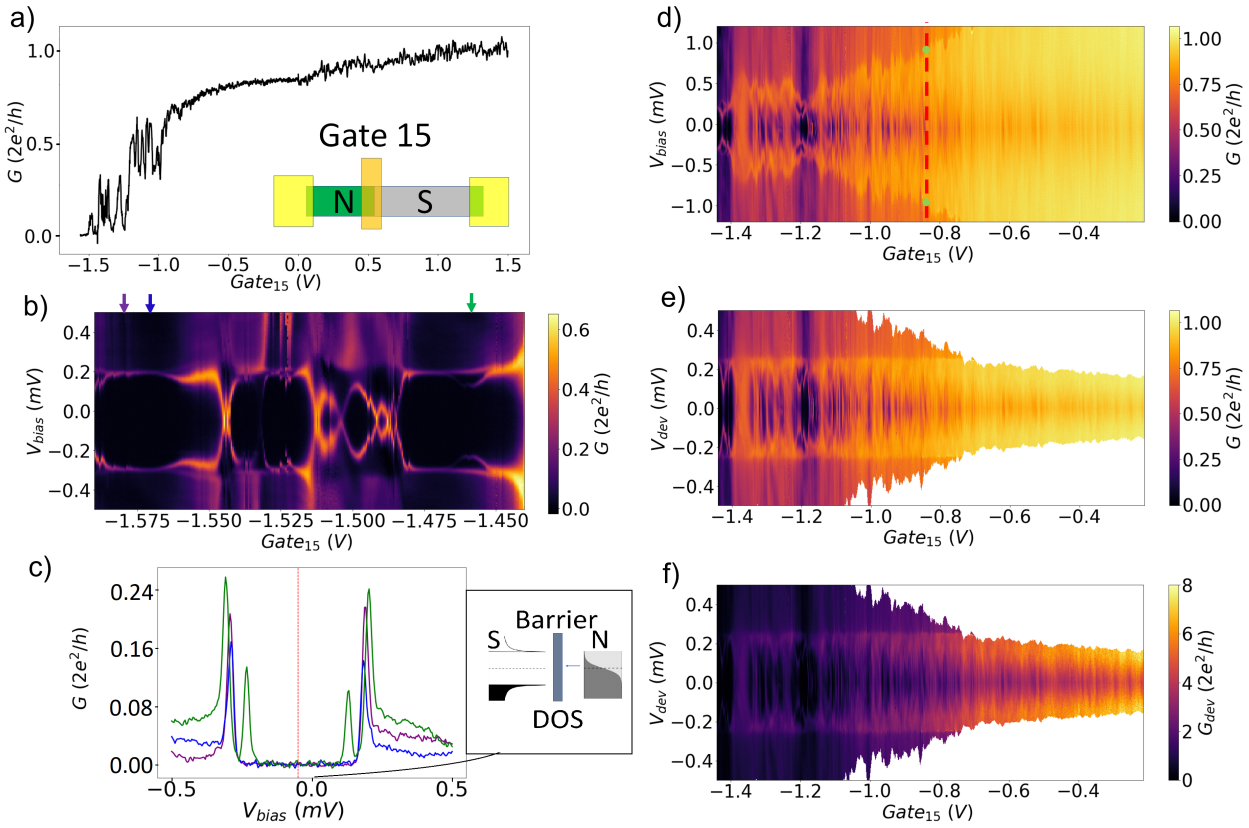

Figure 5.26: Bias spectroscopy vs gate 15 near pinch-off. **a),** The pinch-off curve using the pincher gate no. 15. It was possible to decrease the tunnel barrier and gain $\approx$ 25% of conductance by applying $\approx$1.5 V. The inset show the device setup for this measurement **b),** bias spectroscopy in the near-pinch-off area. A clear Δ is resolved with a value of $\approx$ 195 µeV. The low energy bound sub-gap states are not considered in this thesis. **c),** line traces in b) along the colored arrows used to estimate a bias offset of $\approx$ 0.05 mV. The inset illustrates the gate induced tunnel barrier, preventing transmission of sub-gap energy electrons resulting in zero conductance. **d),** Bias spectroscopy at larger gate voltages. The information of the value of Δ from b) was used to estimate a series resistance. **e),** When subtracting the voltage that drops across the series resistance ($\approx$ 11 kΩ) from the bias voltage, the voltage drop across the devices is left and a constant Δ is seen, indicating that R_s is constant as a function of the pincher gate. **f),** same as in e) but with the device conductance as the color scale.

voltage, due to the series resistance. To investigate the induced superconductivity a DC bias spectroscopy near pinch-off was carried out and is shown in 5.26b. Indeed, this shows the presence of an induced superconducting gap with size $\Delta = 195$ µeV. In addition to the gap, low energy bound sub-gap states is seen at several gate voltages. The cause of this effect is beyond the scope of this thesis and will not be discussed further. Line traces were taken along the V_{bias} at various gate voltage values indicated by the colored arrows in fig. 5.26b and plotted in fig. 5.26c.

UCF is a zero bias phenomenon. To make sure that the measurements were conducted at zero bias, a bias offset was found from the line traces in fig. 5.26c, to be -50 µV indicated by the red vertical dashed line. This offset comes from the input-offset of the CTV and is subtracted in the following measurements. The inset next to fig. 5.26c shows the mechanism behind the zero bias conductance, that arises from the large pincher gate induced tunnel barrier.

In fig. 5.26d, bias spectroscopy at larger gate voltages is shown. As the voltage increases an increase in conductance below the SC-gap is expected due to stronger coupling between the N- and S-part of the wire. That is the probability of AR increases. This is consistent with what is seen in fig. 5.26d. The voltage drop across the semiconducting device (V_{dev}) is variable. From the size of Δ, together with the evolution of the conductance at higher gate voltages to estimate the series resistance (R_s) by applying the voltage divider relation:

$$V_{device} = R_{device} \times \frac{V_{bias}}{R_s + R_{device}} \tag{5.20}$$

and

$$V_{device} = V_{bias} - R_s I_{dc} \tag{5.21}$$

Using eq. 5.20 at very low gate voltages where $R_{device} \gg R_s$, $V_{bias} = V_{device}$ which at $\frac{\Delta}{e} \approx 195$ µV.

What appears to be a broadening of $\frac{\Delta}{e}$ with increasing gate voltage, arises from when the device resistance decreases relative to the series resistance and more bias is needed to get a voltage drop across the device equal to $\frac{\Delta}{e}$. We can use this information to evaluate to the variation in the conductance in a small area around the bias at the green points, V_{bias}^{GP}, in fig. 5.26d, since here, the voltage drop of the device should be approximately 195 µV. This leads

to the relation:

$$R_s = \frac{V_{bias}^{GP}}{I_{dc}} - \frac{\Delta/e}{I_{dc}} \tag{5.22}$$

From which a value of $R_s \approx 11$ kΩ was estimated. When plotting eq. 5.21 in fig. 5.26e, a constant Δ/e is seen indicating a constant series resistance as a function of the pincher gate. In fig. 5.26f, R_s has been subtracted from R_{device} and the conductance of the device is plotted.

The final gate on the device is the back gate. But it was not used during this thesis, since it showed very little response.

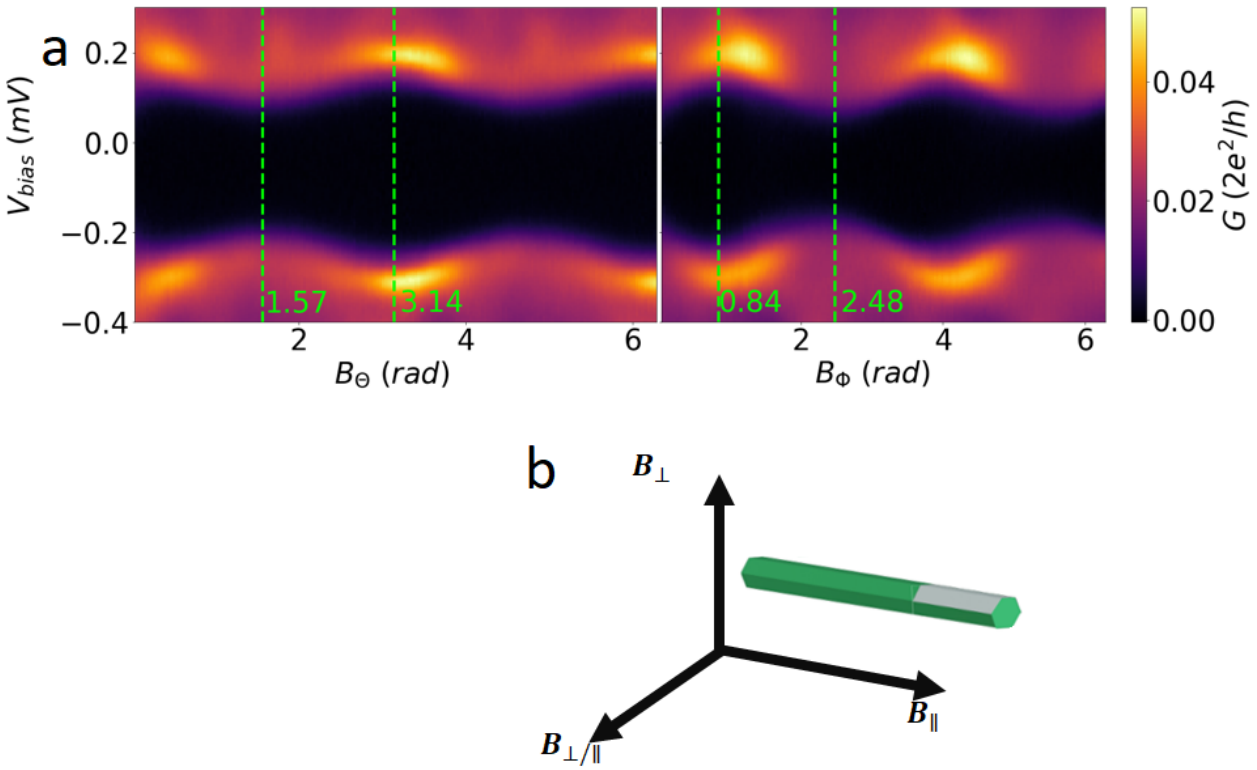

Figure 5.27: a, A bias spectroscopy vs angle of B-field showing the variations of Δ as the azimuthal and polar angle of the B-field is rotated. **b,** From the information i a, we could define three major axes of the B-field, $B_\parallel$, $B_\perp$ and $B_{\perp/\parallel}$, each with their own value of B_{crit}.

Direction of B-field

To find how the device was placed on the chip relative to the axes of the magnet, we did bias spectroscopy near pinch-off vs both the polar- and azimuthal angle, Θ and Φ, respectively as shown in fig. 5.27a. These plots show variations of Δ as the angle of the B-field is rotated. Since B_{crit} depends on the prospect area to the Al this was exploited to define three major B-field axes as shown in fig. 5.27b. We define them as $B_{\parallel}$, which was parallel to the wire. ($B_\Theta = 0$ and $B_\Phi = 0.84$), then $B_\perp$, which was perpendicular the wire ($B_\Theta = 1.57$ and $B_\Phi = 2.48$) and finally, then $B_{\perp/\parallel}$, which was also perpendicular to the wire ($B_\Theta = 1.57$ and $B_\Phi = 0.84$) but with a different prospect area to the Al compared to $B_\perp$.

5.1.2 Auto Correlation Functions

Figure 5.28 shows typical UCF that we will analyze. These fluctuations are aperiodic and were reproducible. To quantify the length scales of the fluctuations the autocorrelation function (ACF) was used. Energetically, the ACF is a measure for the typical scale we need to sweep (gate voltage or B-field) to be uncorrelated. The ACF is defined as:

$$F(\delta x) = \langle (G(x) - \langle G(x) \rangle) \cdot (G(x + \delta x) - \langle G(x) \rangle) \rangle \tag{5.23}$$

where x represent either the magnetic field, B or the gate voltage, V_g. The half-maximum of the function defines the correlation scale, x_c, by $F(x_c) = 0.5F(0)$, where $F(0) =$ the variance. Measuring B_c (not to be confused with the critical field, B_{crit}, of a superconductor), provides information about the phase coherence length, l_ϕ, which from a semiclassical approach is obtained from the expression: $l_\phi = \gamma \frac{\Phi_0}{B_c W}$, where W and Φ_0 is the width and half the

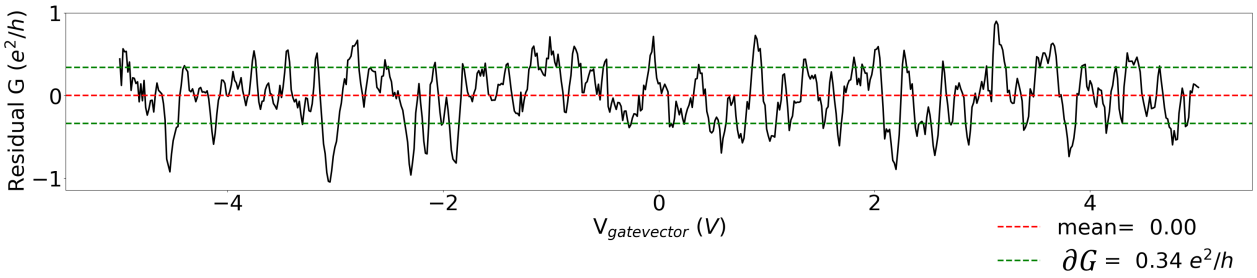

Figure 5.28: The residual G($V_{gatevector}$). All gatevector traces presented in this section were fitted to a 4th-degree polynomial and from the residual conductance (black) a root-mean-square value was calculated giving the amplitude of the UCF, δG. Here is an example of the δG at B= 0 T

flux quantum, respectively. The constant, γ takes the value of 0.42, in a dirty sample at low temperatures where $l_\phi \ll L_T$[66]. It is assumed that B_c is inversely proportional to the maximum phase-coherently enclosed area[8]. For the quasi-one-dimensional system considered here, with $l_\phi \gg W$ this area is given by $l_\phi W$. In fig. 5.29a, an example of the conductance as a function of the perpendicular magnetic field is plotted after averaging out unwanted noise with a Savitzky-Golay filter. As expected from a two-terminal measurement the conductance trace is symmetric around zero field. By calculating the correlation function in fig. 5.29b&c, for $B < B_{crit}$ (blue box) ($\approx$ 2.1 T) and $B > B_{crit}$ (purple box) B_c, was extracted. From this, the value of l_ϕ, was found to be $\approx$ 300 nm, given that the width of the wire was measured to be $\approx$ 100 nm. It is stressed that this single-measured value of l_ϕ is encumbered with high uncertainty, however, being smaller than the length of the normal part of the NS-wire, we would expect a l_ϕ-related decrease in the absolute value of the UCF-amplitude compared to the theoretical value. It is noticed that B_c below the critical field is approximately half the value of the value above the critical field. This is attributed to single electrons/holes with a doubled l_ϕ due to a maintained coherence from the superconductor.

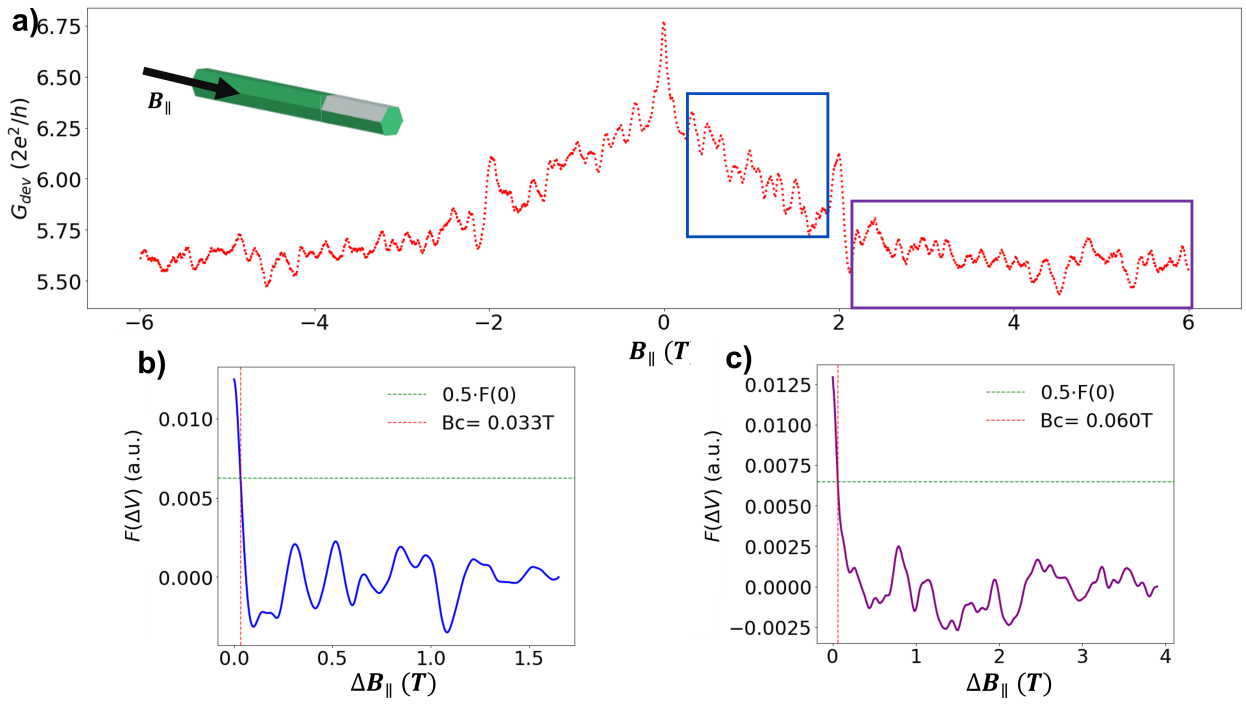

Figure 5.29: ACF for the conductance vs. the parallel magnetic field. **a),** Conductance vs $B_\parallel$. The parallel critical field was $\approx$ 2.1 T. **b**, the ACF for $B < B_{crit}$, yielded a correlation field of $\approx$ 0.033T. **c**, the ACF $B > B_{crit}$ gave a correlation field of $\approx$ 0.060T, corresponding to a phase coherence length of $\approx$ 300 nm.

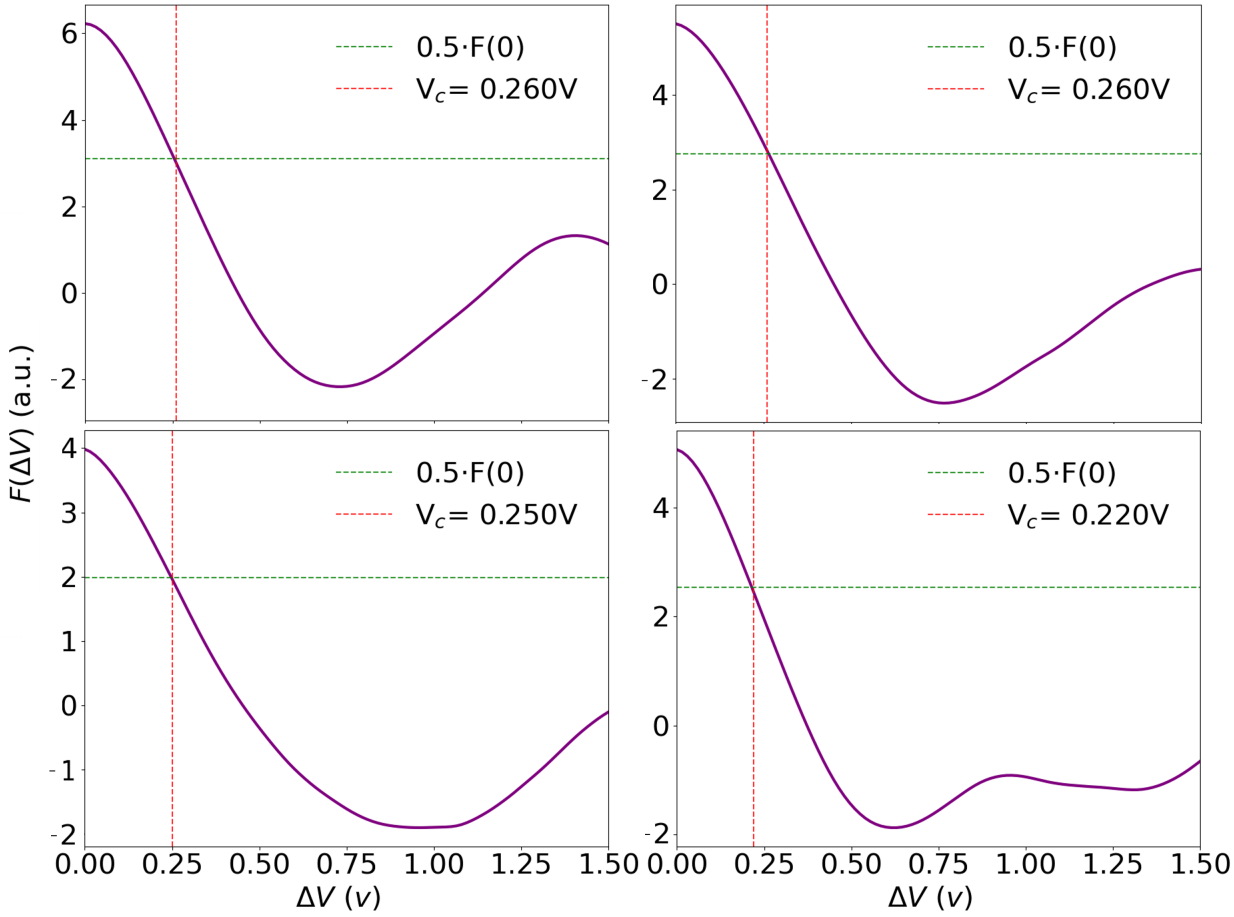

Figure 5.30: The correlation function investigated along the gatevector. With a V_c up to 0.260 V and a sweeping range of 10 V, it is expected that each gate trace gives 30-40 UCF-peaks.

Next, the doubly diminished correlator defining the shift in chemical potential V_c is calculated. The ACF was calculated along the defined gatevector for different values of the B-field. In fig. 5.30 the correlator for three different traces a plotted and shows a V_c up to 0.26 V. Since the sweeping range of the gatevector for these measurements was 10 V we expect around 30-40 UCF-peaks for each gate trace. The value of V_c is also used to shift the gatevector a sufficient amount to uncorrelate the transport properties[67].

5.1.3 Bias Spectroscopy and Temperature

In fig. 5.31a, bias spectroscopy as a function of the applied gatevector is shown in a more open tunnel barrier regime (pincher gate 15 at 1.5 V). Similar to what was shown in fig. 5.26 an increased pincher gate voltage increased both the subgap and above-gap conductance. The conductance peaks, corresponding to enhanced quasi-particle transport when the peaks in the DOS of the leads line-up at $V_{dev} = \pm\Delta/e \approx 195$ µV, are located at a fixed bias value throughout the entire gate voltage range which indicates that neither the induced gap nor the series resistance, depend on the gate voltage. In the inset of fig. 5.31a, the average conductance vs V_{dev} is shown. A suppression of the transmission at zero bias is seen, I interpret

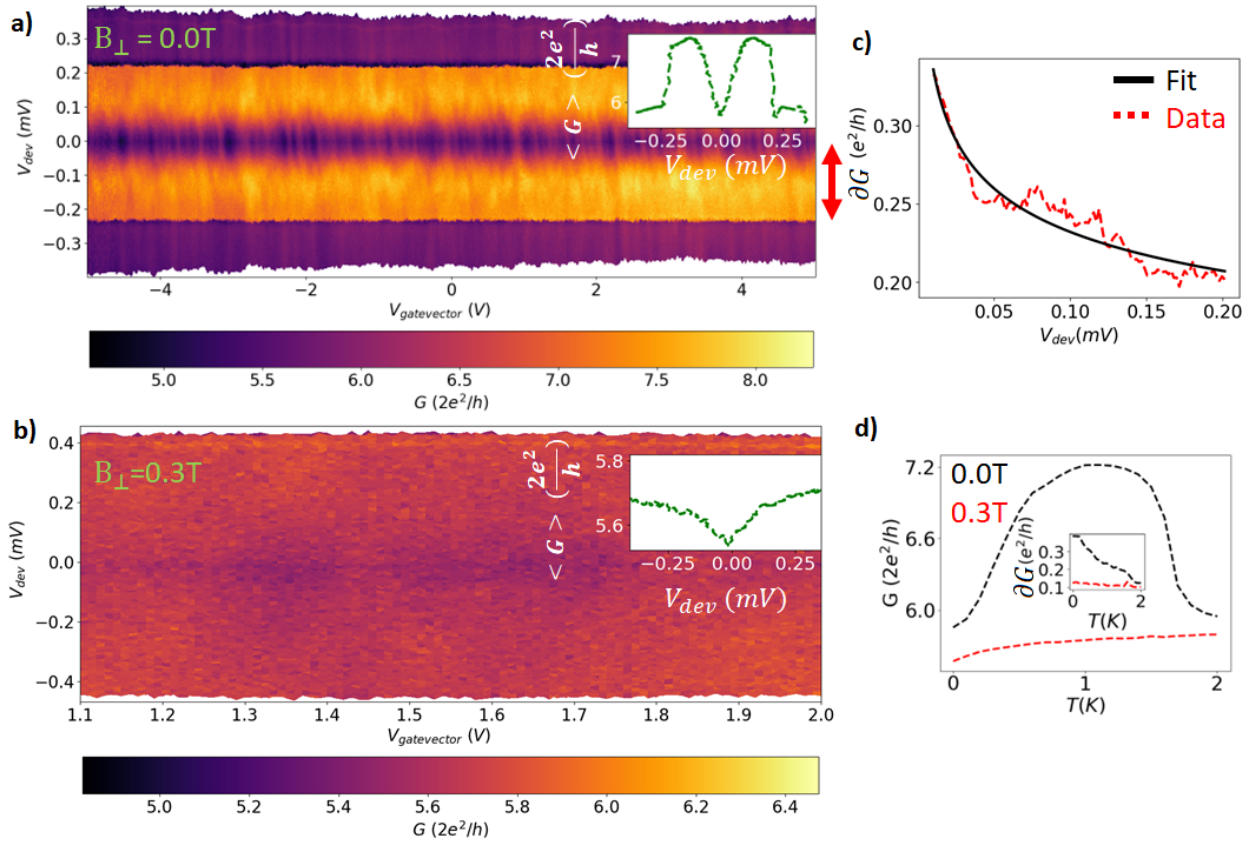

Figure 5.31: Bias spectroscopy along the gatevector. **a),** The conductance as a function of bias and gate voltage at 0 T. A constant SC-gap indicates independence on the gate voltage. The inset shows the average G(V_{dev}). The suppressed transmission might be explained by having an ideal NS-interface causing the EWL-effect **b),** The same as in a, but with a a finite field above B_{crit}. **c),** shows the δG as a function of the applied bias-voltage, with a dependence $\propto V_{dev}^{-0.16}$ obtained from the fit. **d),** The temperature dependence of the conductance and the δG (inset). In both the normal (red) and SC (black) state dephasing causes a decrease in the δG.

this observation as a "*enhanced weak localization*" (EWL). The theory of EWL is developed for a transmission probability per mode of the potential barrier at the NS-interface, Γ, close to 1. To explain this counter-intuitive property, it is convenient to replace the disordered medium by a tunnel barrier inside the semiconductor and consider a periodic orbit consisting of two normal reflections and two retro-reflections as shown in fig. 5.32. A periodic orbit consists of two round-trips, one as an electron at $E_f + \epsilon$, the other as a hole at E_f - ϵ. An incoming electron acquires a phase, $\phi - \pi/2$ upon AR, while the outgoing hole acquires a phase, $-\phi - \pi/2$ upon AR[68]. Thus, we see that a net phase increment of $-\pi$ causing phase coherent particles to interfere destructively. Since EWL requires the phase coherence to remain on length scales larger than the scattering length it is destroyed not only by a magnetic field but also by an applied voltage, which enables detection of EWL in the current-voltage characteristic of an NS junction. It is the enhancement that is destroyed by an applied bias voltage while the weak localization effect is destroyed by the applied B-field[69]. From the width of the EWL dip the Thouless energy, $E_{Thouless} = \frac{\hbar\pi D}{l_\phi^2}$ can be roughly estimated[70] and from this, the diffusion coefficient, D, is determined to be on the order 10^2 cm^2/s, resulting in a thermal length on the order of a few microns. The EWL-effect is considered plausible here, since when applying $B_\perp > B_{crit}$ seen in fig. 5.31b to the same measurement, only a small dip in conductance of ≈ 0.2 e^2/h at zero bias is seen, possibly due to the presence of a Schottky barrier. Further, in the case of a non-ideal interface, $\Gamma = 0.2$-0.4, a conductance

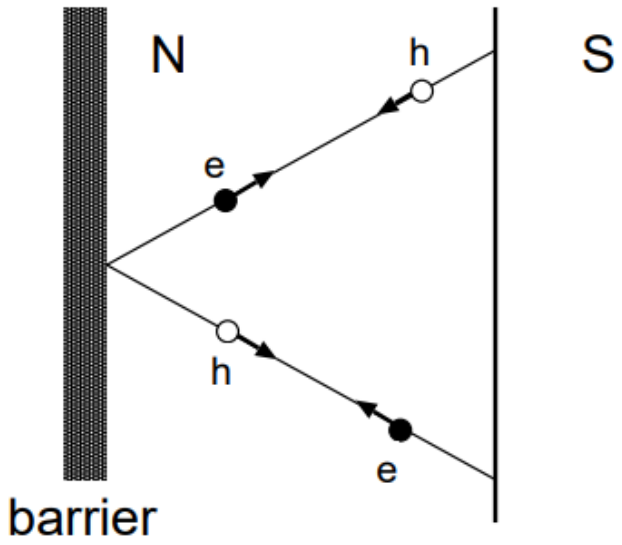

Figure 5.32: The process of EWL. At $B = 0$ T and zero bias, the periodic orbit consisting of two normal reflections and two retro reflections acquire a net phase increment -π, causing destructive interference for electrons. Adapted from ref. [68].

peak would be expected at zero bias due to the effect of "reflectionless tunneling"[70], where, in contrast to EWL, the non-zero probability for single electron reflection at the NS interface, gives repeatedly attempts to undergo AR. More data indicative of an EWL-effect will be presented in the forthcoming figures.

The total zero-bias conductance of ≈ 12 e^2/h is high for NWs, and we consider it reasonable to compare it to the RMT of the large $N >> 1$, which gave the bimodal function defined in eq. 2.10. In fig. 5.31c, δG of horizontal cuts in fig. 5.31a in a bias range of $\pm$ 0.2 V is shown. From a fit to this, δG was found to have a $\propto V_{dev}^{-0.16}$ dependence, which is far from the theoretical value[67] of $\propto V_{dev}^{-2}$. I do not have an explanation to the discrepancy.

Figure 5.31d shows the temperature dependence of the conductance for the NW in the SC-state and normal state, respectively. When in the SC-state the conductance increases up until it reaches the critical temperature before decreasing to the normal state value. What exactly causes the observed T-dependencies is not so clear but it could be related to the T-dependency of EWL and needs further investigation. However, in both the normal and SC state δG decreases with increasing temperature which is an expected dephasing effect.

5.1.4 Probing Symmetry Breaking with UCF

In this final section regarding UCF, the effect of symmetry breaking on the δG values is presented and discussed. A summary of the results is schematized in fig. 5.38.

On the absolute value of δG - classifying the ensemble

In fig. 5.28, δG of the NS-conductance at $B = 0$ T was shown to be 0.34 e^2/h. This value is far from the theoretical value of 1.51 e^2/h from a COE at zero temperature[30]. In the previous section we showed data which could indicate that the NS-interface is approximately ideal and therefore should be comparable to the theory that was introduced in chapter 2. So to explain the discrepancy, it is instructive to first classify our ensemble by considering the measurements of the reference N-device (5-7 in fig. 5.24). Unfortunately, this wire had only one functioning side gate (no. 8). Consequently, it was only possible to change the potential in a 10 V range. Also, only one pincher gate was working (no. 9) and was maximally opened. Figure 5.33a, show a measurement of conductance as a function of side gate 8 and parallel magnetic field for the reference device. From this data, the average conductance and δG as a function of $B_{\parallel}$ was extracted and are shown in fig. 5.33b and fig. 5.33c, respectively. The average conductance shows a peak at zero field, which we attribute to a weak anti-localization (WAL) effect arising

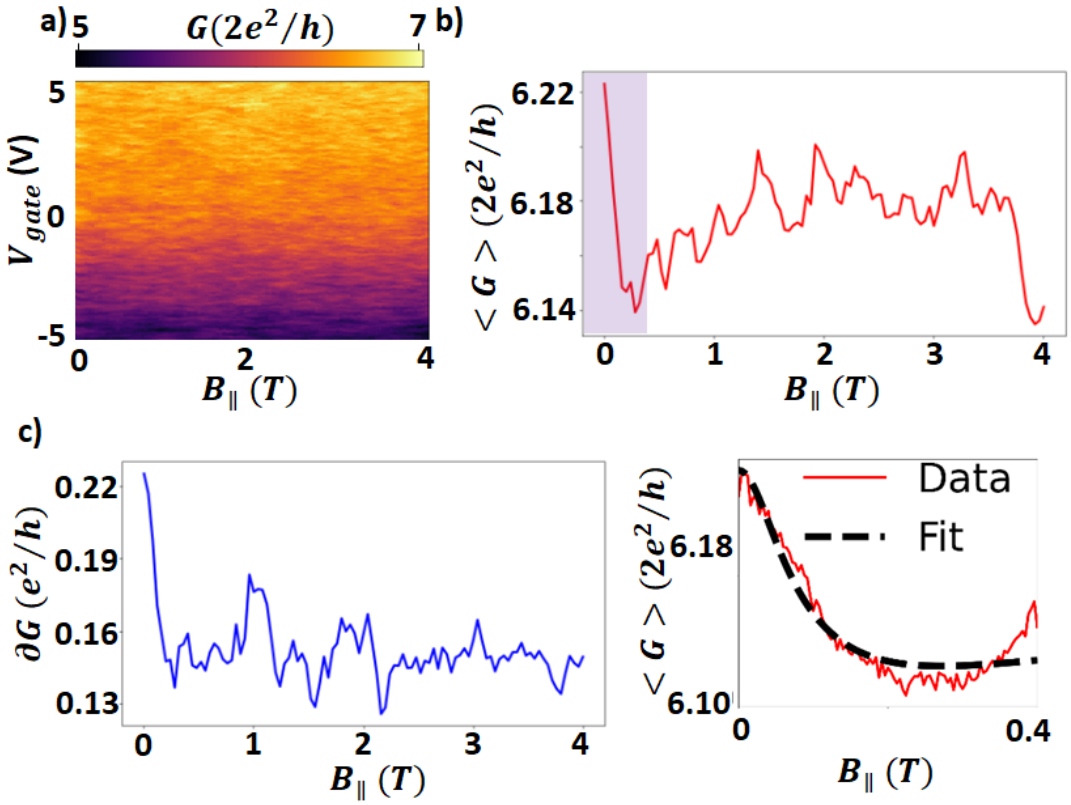

Figure 5.33: UCF measurements of the reference N-device. **a),** the gatevector was swept from ± 5 V and the parallel B-field was stepped while measuring the conductance. The series resistance was essentially unknown but here, 11 kΩ has been subtracted as was measured for the NS-device. **b),** The average conductance extracted from vertical cuts in a. We see a WAL-peak indicative of strong SOI. This makes the system belong to the CSE ($\beta = 4$). The inset below shows a fit of the shaded area to the WAL peak using the dirty metal limit. This estimates l_ϕ to be ≈200 nm. **c),** The extracted δG as a function of $B_\parallel$, shows a single drop in amplitude by a factor of 0.67 owing to the breaking of TRS.

from strong spin-orbit interaction (SOI). This is usually seen in InAs NWs[71–74]. This makes the system belong to the CSE ($\beta = 4$), which leads to by a reduction of the theoretical δG by a factor of 2 compared to COE. Since the SOI also lifts spin degeneracy (g_s: $2 \rightarrow 1$), the δG is reduced by an additional factor of $\sqrt{2}$. The theoretical value of δG in this NS device, at T=0 K, is, therefore, ≈ 0.52 e^2/h. However, if we instead use Beenakker and van Houten's interpolation formula eq. 2.12, for $T > 0$, inserting the correlation field measured value of l_ϕ, 300 nm (see section 5.1.2), and assuming a regime where $l_\phi \ll L_T$, a value of the δG of ≈ 0.30 e^2/h is obtained, in good agreement with the measured value. We emphasize that there is some controversy on how to extract l_ϕ and that the small discrepancy between the

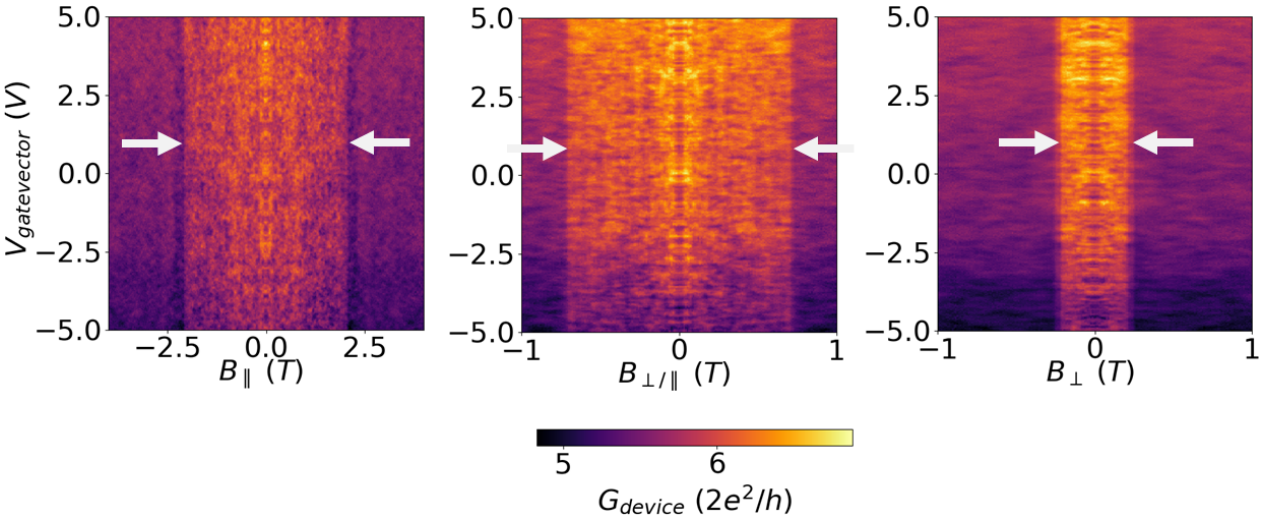

Figure 5.34: Conductance of the NS-device as a function of gate voltage and the B-field for three different B-field directions. The crossover from the brighter regions to the darker regions defines B_{crit} (indicated with arrows) measured to be $\approx$ 2 T, 0.75 T and $\approx$ 0.25 T for the $B_{\parallel}$, $B_{\perp}/\parallel$ and $B_{\perp}$ field, respectively.

theoretical- and measured value of δG might reflect a high uncertainty of the extracted phase coherence length. This is further accentuated by the fact that the fit of the WAL-peak in the inset of fig. 5.33 (using the dirty metal limit[75]), gives a phase coherence length of 200 nm - approximately a 2/3 of the value obtained from measuring B_c. Another factor that might add to the discrepancy is that the amount of UCF-peaks within a measurement (40-80 peaks) borders low statistics. A coincidence of the effect of low statistics might be what we observe as the relatively large oscillation in the amplitude of the δG in 5.33c.

It should be noted, that the absolute value of the δG in fig. 5.33c is not comparable to the δG of the NS-device, since the series resistance was unknown in this device. However, the trend seen in the plot caused by symmetry breaking is still useful. For example, the trace of the δG as a function of the B-field shows a clear drop by a factor of 0.67 in amplitude around B =0.1 T. This is close to the theoretical value of $1/\sqrt{2}$ for breaking TRS and lifting Kramer's degeneracy. We see no further drop in amplitude at a larger field from Zeeman-effect since spin degeneracy was already broken by SOI[76].

The NS-device

Having accounted for the classification of the intrinsic ensemble, the attention is now turned toward the NS-device. The B-field was stepped along the three major axes (See. fig. 5.27) of the NW and the gatevector was swept while measuring the conductance as seen in fig. 5.34. To gather larger statistics, we managed to run the measurements twice with the

gatevector of the first measurement shifted along gate no. 12 by 2 V, relative to the second measurement as seen in fig. 5.35. The magnitude of the shift is much larger than V_c and enables us to measure twice the amount of different impurity configurations, thereby doubling the amount of UCF-peak to around 70. The remaining figures in this section plot an average of the measurements along the shifted gatevectors. The three different B-field axes all show a region at a low field of higher conductance followed by a region of lower conductance at a high field. A crossover between the two is seen when the system changes from NS-state to N-state at B_{crit}. The critical field magnitude is dependent on the direction of the field and is $\approx$ 0.25 T, 0.75 T and 2.0 T, for $B_\perp$, $B_{\perp/\parallel}$ and $B_\parallel$, respectively.

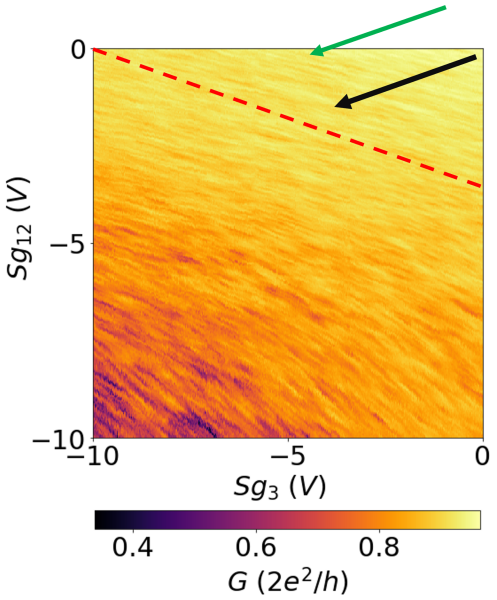

Figure 5.35: The two gatevectors, green and black arrows, that we swept along. Series resistance not subtracted here.

To investigate the B-field dependence of the conductance more closely, the average of vertical cuts in fig. 5.34 were calculated and plotted vs the B-field in fig. 5.36. Here, especially the decrease in conductance at zero field is interesting, since it is consistent with the theory of EWL-effect and the zero-bias conductance dip that was seen in fig. 5.31a. This adds to the hypothesis of a close-to-ideal NS-interface with a high AR probability. A theoretical treatment of a system similar to ours by ref. [77], explains the mechanism of the zero-bias dip at zero B-field. The dip in conductance at zero field is destroyed by TRS-breaking when exceeding the correlation field and in the second row of fig. 5.36, a smaller B-field range is displayed from which the magnetic field scale of the breaking of TRS in the three maps is observed to be roughly of the same order as was previously measured with the ACF ($B_c = 0.06$ T, section 5.1.2).

Since the B-field was stepped across B_{crit} in each direction it was possible to directly probe the relation between δG_{NS}(no TRS) and δG_N(no TRS). Figure 5.37, shows the δG as a function of the B-field in all three directions. From the data in fig. 5.37a-c, a few general statements of δG can be made. First, the value peaks at $B = 0$ T. Then by increasing the B-field we see first a large drop in δG, indicated by the red arrow, until it settles on a plateau. The factor by which δG drops here, is on average 0.68 e^2/h with a minimum of 0.63 e^2/h

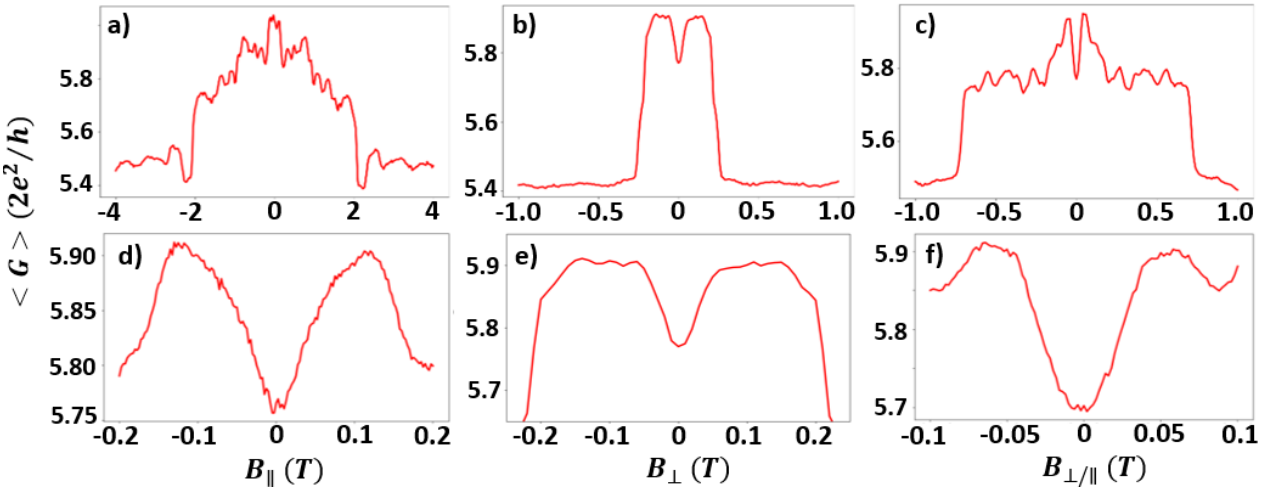

Figure 5.36: The B-field dependence of the average conductance. Measuring along all three major B-field axes, shows two main trends. First, a dip in conductance around 0 T is observed, that might be explained by the EWL effect. The dip is destroyed by TRS-breaking when exceeding the correlation field. At larger fields $B = B_{crit}$ a drop in conductance is seen due to a transition of NS-state into N-state.

for the $B_{\perp/\parallel}$ measurement and a maximum of 0.73 e^2/h $B_{\parallel}$ measurement. This factor is close to the theoretical value followed by changing the ensemble from CSE to CUE. That is, *the fluctuation amplitude of the NS-device is sensitive to the breaking of TRS*. When the magnitude of the B-field crosses B_{crit}, we observe another large drop with an average value of 0.57 e^2/h to a new plateau. This drop is attributed to the breaking of particle-hole symmetry. For $B_{\perp}$ and $B_{\parallel}$ the drop is 0.55 e^2/h and 0.52 e^2/h which is in good agreement with the

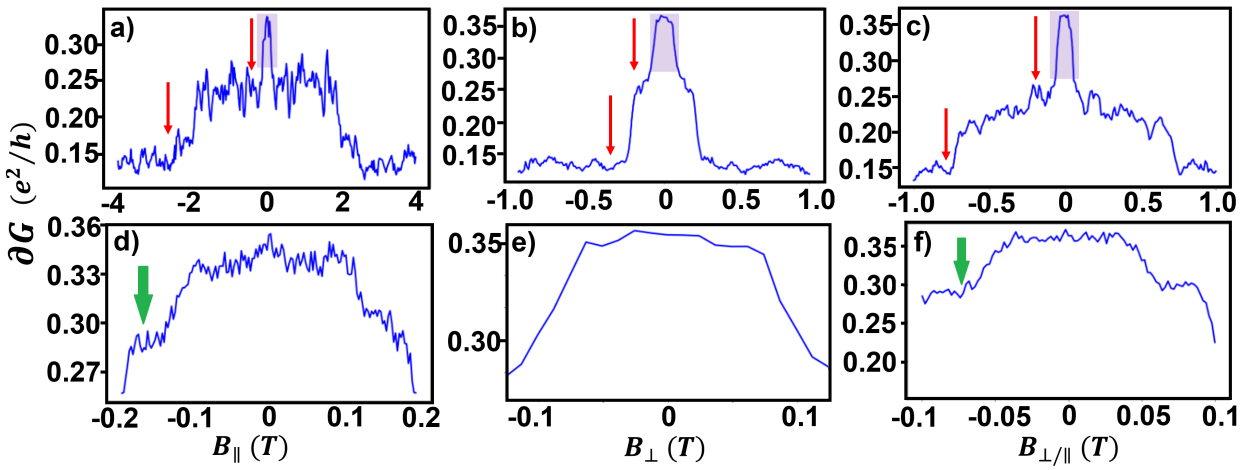

Figure 5.37: The evolution of UCF when a applying a B-field. **a-c,** The red arrows indicate the two major drops in amplitude observed. **d-e,** A higher resolution of the peak in a small range around 0 T. For $B_{\parallel}$ and $B_{\perp/\parallel}$, an additional plateau appears, that we are not able to explain with the present amount of data.

	$B_{\parallel}$	$B_{\perp}$	$B_{\perp/\parallel}$	**Control**
	$\partial G\ (e^2/h)$	$\partial G\ (e^2/h)$	$\partial G\ (e^2/h)$	$\partial G\ (e^2/h)$
Peak value	0.337	0.361	0.361	0.225
	↓ · 0.73	↓ · 0.70	↓ · 0.63	↓ · 0.67
1st Plateau	0.245	0.253	0.226	0.150
	↓ · 0.55	↓ · 0.52	↓ · 0.64	
2nd Plateau	0.135	0.132	0.145	--------
Averaged 1st drop factor = 0.68	**Averaged 2nd drop factor = 0.57**			

Figure 5.38: Summary of the results for the NS-device and the control device. The NS-device and the control device are both transformed from a CSE into a CUE when breaking TRS with a B-field and δG was reduced by $\approx 1/\sqrt{2}$. When the B-field was increased further, the particle-hole symmetry of the NS-device was broken, an additional reduction of $\approx 1/\sqrt{2}$ was observed

theoretical value of ≈ 0.5 e^2/h. For $B_{\perp/\parallel}$ the value is higher (0.64 e^2/h). We do not know the origin of this but this may be related to insufficient statistics.

Whether the normal region contains a reflection symmetry could not be verified from these measurements since this would have required the theoretically predicted insensitivity to the breaking of TRS of the NS-device, together with a fully functional control device with a known series resistance.

In fig. 5.37d-f, a higher resolution (shaded area in fig. 5.37a-c) in a small B-field range shows that for $B_{\perp/\parallel}$ and $B_{\parallel}$ the peaks around 0 T reach an extra small plateau, indicated by the green arrows, before reaching the first large plateau seen in 5.37a&c. It is not seen for $B_{\perp/}$ but this might just be due to a smaller resolution of this data set compared to fig. 5.37d&f. It is hard to imagine extra hidden symmetries that can be broken by an applied B-field in this region and may be related to insufficient statistics. Future measurements may shed further light on this. In general, this might be the cause of the discrepancy between data and theory and future work will aim toward building statistics of the UCF in similar devices.

5.1.5 Summary

The work in this section revolved around UCF in NS-devices to gain insight into the QI-effects in a disordered system with a long phase coherence length. A semiconductor-superconductor hybrid nanowire consisting of a hexagonal cross-sectional InAs wire with half-shell coated Al on two facets was used for this purpose[57]. One of the fabricated devices had a sufficient number of working gates to control the electron wavefunction and density in the device, which was used to gather statistics in various different symmetry regimes. From initial transport characterization with tunnel spectroscopy and magnetoconductance measurements, we saw signs of an EWL-effect indicating that we had an ideal NS-interface which was a condition of the theoretical models concerning UCF[30,68,70,77]. We learned that the amplitude of the UCF is controlled by the presence of fundamental symmetries. Even though the absolute values of the amplitudes diverged slightly from the theoretically predicted values, it was indeed possible to probe the breaking of TRS and particle-hole symmetry by analyzing the amplitude of the UCF in a magnetic field and shifting chemical potentials. To the extent of my knowledge this is the first time the particle-hole crossover has been studied experimentally using UCF. We found that the change in amplitudes caused by breaking these symmetries was not fully consistent with the theories presented in this thesis[31,34,42,75]. For example, the fluctuation amplitude of the NS-device showed sensitivity to the breaking of TRS, which was not predicted by theory[42]. Further, we measured a drop in δG that was related to the breaking of particle-hole symmetry, however, whether the value of this drop contain a hidden exchange of symmetries, e.g. reflection symmetry in the normal device, is not clear and needs further investigation from more devices.

5.2 FET-Mobility

For the measurements of mobility in SAG-FET devices the two setups seen in fig. 5.39, were used. The circuit diagram in fig. 4.20 was used with an applied AC-excitation of 100 µV, while the inner voltage probes were either floated in the sample (FET) measurement or connected to transverse and longitudinal volt-meters for the reference (Hall) measurement. As shown in Ref. [44], the transport is confined to the outer InAs shell.

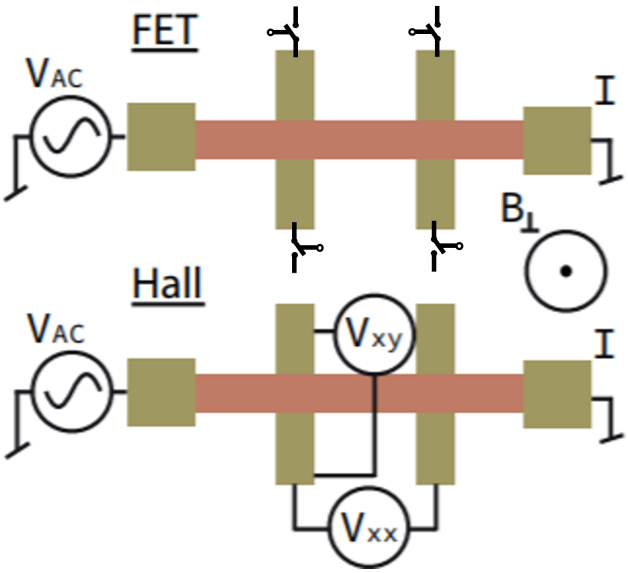

Figure 5.39: *Top:* A schematic of the FET measurement setup used to extract the mobility of the SAG-NWs. *Bottom:* A schematic of the Hall measurement setup used as a reference to the FET-measured data.

We consider first the results from operating the device in the Hall configuration. The voltage drop in the transverse and longitudinal direction was measured as a function of the top gate voltage (V_{tg}) and the perpendicular magnetic field ($B_\perp$). The resistances, R_{xy} and R_{xx} were extracted and are plotted for device Fg1HB4 in fig. 5.40. For the raw measurements from which R_{xy} and R_{xx} is extracted see fig. S53. To reduce hysteresis, and thereby simplify the determination of the threshold voltage (V_{th}), the voltage was limited to range from the ≈ pinch-off point to the beginning of the fully open regime. As a consequence, the gate traces in fig. 5.40a, show exemplary reproducibility, regardless of the sweep direction. The increasing magnetoresistance shown in fig. 5.40d has been observed previously, and attributed to geometrical factors[78].

Indeed, our sample deviates from the archetypal Hall bar geometry. Notably, the 2DEG is confined to a triangular, not flat, surface, the voltage probes are offset due to the intrinsic crystal symmetry of InAs grown on GaAs, and the probes also have a non-zero extension along the channel. In order to ensure that the Hall measurements could function as accurate reference measurements, electrostatic simulations were undertaken by Thierry Pomar using the COMSOL software package, based on the geometry shown in fig. 5.40c. The best fits from these simulations to the data are shown in fig. 5.40e, and suggest a geometrical factor of ≈ 0.90 to modify the carrier density in the NWs. This arises from the deviation from the standard Hall geometry in that the channel has the shape of a pyramid and the voltage-probes

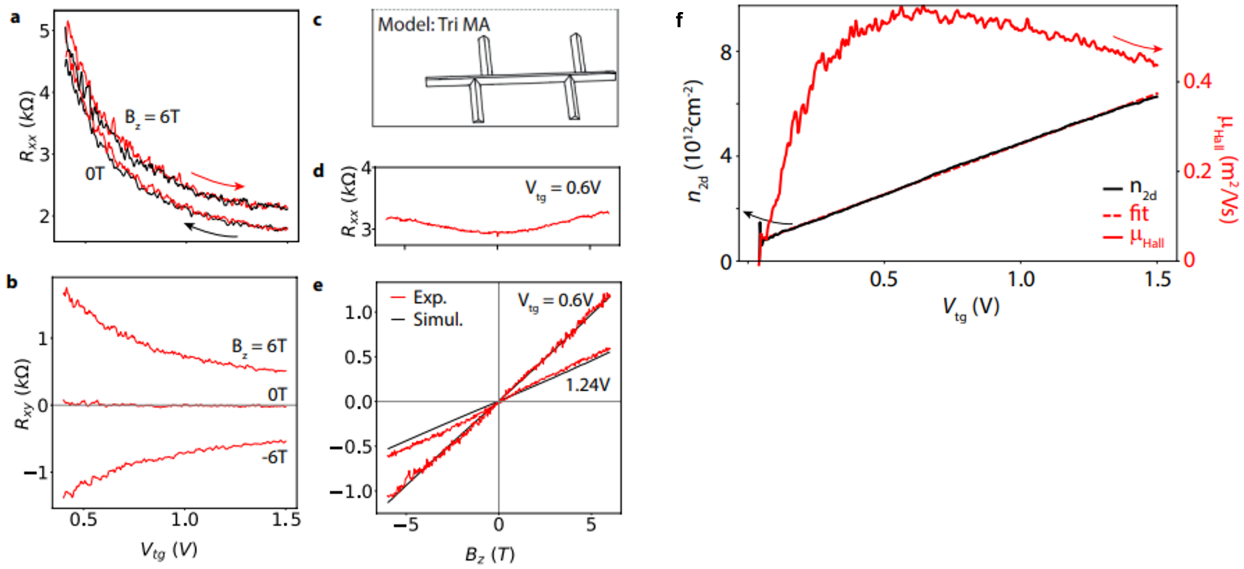

Figure 5.40: Device Fg1HB4. **a**, trace and retrace of R_{xx} as a function of V_{tg} for a perpendicular field of 0 T and 6 T, showing excellent reproducibility. **b**, R_{xy} as a function of V_{tg} after subtraction of the R_{xx}-component caused by misaligned voltage probes. At finite B-field the transverse resistance drops as the transport channel widens. **c,** illustrates triangular shaped core-shell model with misaligned probes (TRI MA) used for simulations. **d**, R_{xx} as a function of $B_\perp$ average over a range 0.6 V to reduce universal conductance fluctuations. At low field weak anti-localization is observed. The increasing magnetoresistance needs further detailed analysis beyond the scope of this thesis. **e**, R_{xy} as a function of $B_\perp$, that was used to extract a density, at two different values of V_{tg}. The best fits from simulations, accounting for both the special geometry of the NWs and the misaligned voltage probes is plotted on top (dashed). **f,** The 2D carrier density as a function of gate voltage. **Orange**, The fitted 2D carrier density, translating into a constant capacitance/area of $\approx 5 \times 10^{-3}\ \frac{F}{m^2}$. **Blue**, the Hall mobility showing a clear dependence on the density, with a peak value of $\approx 5700 \frac{cm^2}{Vs}$.

are not strictly on the edge of the channel but probes the potential at the entire width of the channel side-facet. Due to a slight misalignment of the transverse inner voltage probes a component of R_{xx} adds to the measured R_{xy}. From the off-sets in the raw data of R_{xy}, the magnitude of this component was estimated to be $\approx 0.125 \cdot R_{xx}$. In fig. 5.40e, R_{xy} as a function of $B_\perp$ is shown, after the intrusive R_{xx} has been subtracted. On top of the data, best fits extracted from the simulations, accounting for both the misalignment and the geometrical factor as illustrated in 5.40c, are plotted. The carrier density for a given V_{tg}, is calculated by fitting to: $R_{xy}(B_\perp; V_{tg}) = \frac{B_\perp}{n_{2d}e}$. The electric field dependence of the carrier density is plotted in fig. 5.40f. The linearity implies a constant capacitance pr. area, $C_i = 5 \times 10^{-3}$ F/m^2. Note, however, that below $V_{tg} = 0.1$ V, the linearity is lost, and the n_{2d} drops rapidly to zero. This occurs since the carrier density becomes comparable to the effective charged impurity

density from randomly distributed charges in the 2d-transportation-layer, interfaces and the surrounding layers. The system then becomes insulating due to a percolation transition driven by the failure of screening leading to an inhomogeneous density landscape[79]. The methods used in this thesis to extract mobilities are only valid above the percolation regime, where there is a linear relationship between the conductivity and the carrier density. From the x-axis intercept of the linear relationship between n_{2d} and V_{tg}, we can extract the threshold voltage, $V_{\text{th}}^{H} = -0.16$ V, which is the V_{tg} for which n_{2d} drops to zero.

With the reference data in place, I now turn the attention towards the FET-measurements. From the reliable mobility, μ_{Hall}[80], the validity of the FET-mobility extracted from eq. 2.18 and 2.19 is tested. For the sake of of the reader, let me just restate the two equations:

$$\mu_{FE} = \frac{gL^2}{C} \tag{5.24}$$

and

$$G_{2p,R_s}(V_{tg}) = \Big(R_s + \frac{L^2}{\mu C(V_g - V_{th})}\Big)^{-1} \tag{5.25}$$

In fig. 5.41a, eq. 5.25 is used to fit the two-terminal measured conductivity of device Fg1HB4. At first glance the fit seems to be rather good. However, by digging deeper and comparing to the reference data in fig. 5.41b-d, we discover that the fit-parameters: R_s, V_{th} and μ are all overestimated with values of $\approx 8.7\ k\Omega$, $\approx 0.06\ V$ and $\approx 8240\ \frac{cm^2}{Vs}$, respectively. The discrepancies of the device properties between the two methods is attributed mainly to the erroneous assumption that μ is a constant material parameter as a function of gate voltage. Only smaller discrepancies are attributed to the fact that the FET and the Hall measurements do not exactly reflect properties from the same transport regions.

In fig. 5.41e, the field effect mobility defined by 5.24, is plotted using first the parameter values from fitting with eq. 5.25, $\mu_{FE(fit)}$,. For reference $\mu_{FE(4p)}$ is plotted. This model has the advantage that it is independent of V_{th}. Compared to μ_{Hall}, the method show the same tendency in V_{tg}. But it tends to overestimate the mobility at low voltages and vice versa, since this model is not accounting for the electric field dependence of the mobility - thereby neglecting a contribution from the extra term that would have appeared when applying the product rule to the derivation of eq. 5.24.

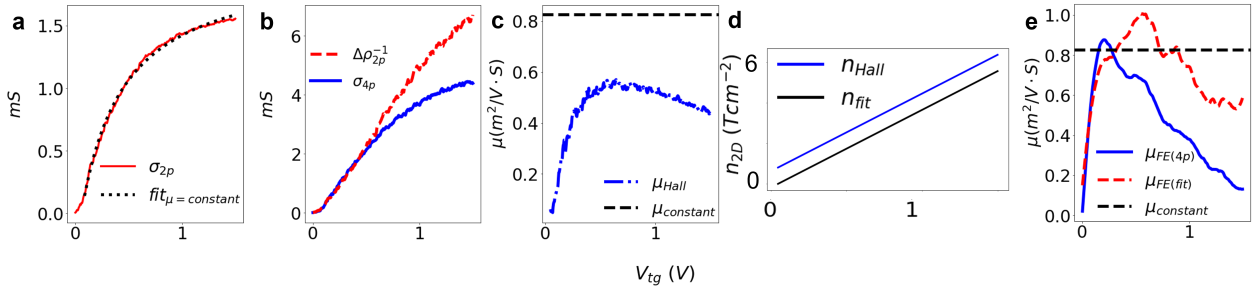

Figure 5.41: **a**, the conductivity of the FET device fitted with eq. 5.25, assuming a constant mobility. **b**, the conductivity of the FET device after the R_s has been subtracted (red). The conductivity of the four-terminal measurement (blue) is plotted to emphasize the error on the fit model, leading to an overestimated series resistance. **c**, the extracted constant mobility from the fit with eq. 5.25 (black) For comparison we plot μ_{Hall} (blue) which shows a largely overestimation of the fitted mobility. **d**, the final parameter from extracted from eq. 5.25, V_{th}, enables to plot the density as a function of gate voltage. When referenced to the Hall density it is clear that this parameter is overestimated as well. **e,** the extracted mobilities using the field-effect mobility method defined by eq. 5.24 for the two-terminal measurement, after the fitted R_s has been subtracted and the four-terminal measurement.

5.2.1 A New Model

The comparison in fig. 5.41 shows that the two commonly accepted methods for extracting FET mobility diverge strongly from the mobility extracted from Hall effect measurements. This motivates development of a new method to ensure better comparability of these two methods. I will now show that it is possible to extract a gate voltage dependent μ from the two-terminal FET measurements and that it closely matches the Hall mobility. This idea is motivated from the plots seen in fig. 5.42a-d. Here it becomes evident that a two-terminal extracted gate voltage dependent mobility, which shows excellent similarity to the Hall mobility, lives somewhere in a multidimensional space expanded in the value of R_s that we subtract from the two-terminal conductance and the value of V_{th} that we choose. In other words, finding the gate dependence of the mobility boils down to being able to estimate values of R_s and V_{th} that are close to the true values.

If in the case where, $\frac{\delta G}{\delta V_g}\,|_{V_{sd}} \neq$ constant but the source-drain conductance, $\frac{\delta I_{sd}}{\delta V_{sd}}\,|_{V_g} =$ constant, an effective mobility, μ_{eff}, can be defined as:

$$\mu_{eff} = \frac{L^2}{C(V_g - V_{th})} \frac{\delta I_{sd}}{\delta V_{sd}}\bigg|_{V_g} \tag{5.26}$$

In practice, eq. 5.26 is the two-terminal measurement equivalent to the Hall mobility, if

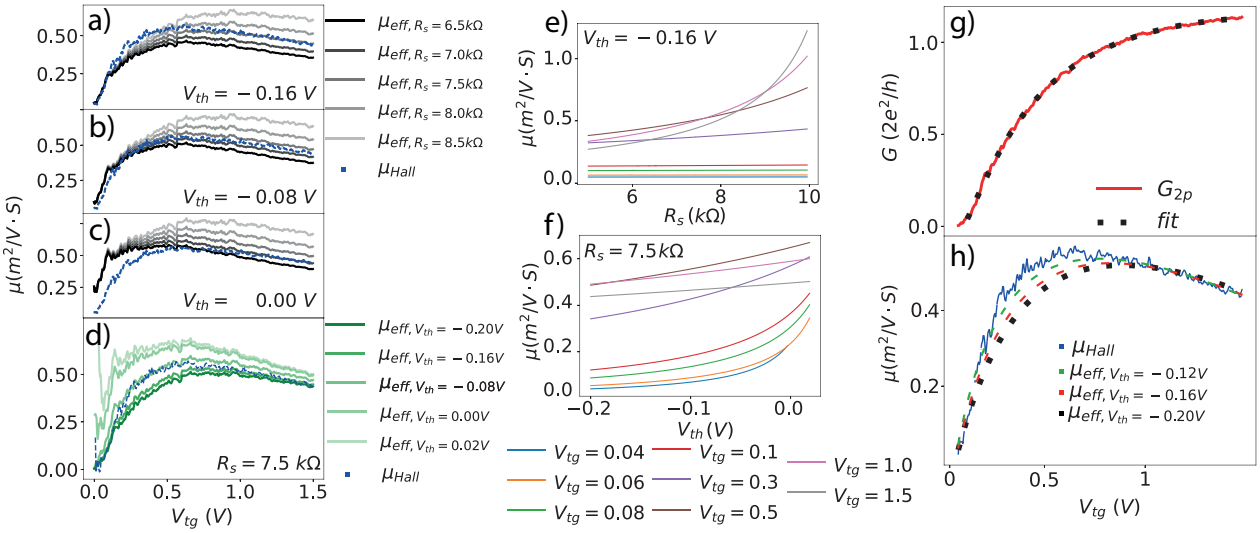

Figure 5.42: a-d), μ_{eff} defined by eq. 5.26 is plotted, for fixed values of V_{th} while varying the subtracted R_s (a-c) and then for a fixed value of R_s fixed while varying V_{th} (d). Comparing to μ_{Hall}, it displays that the a gate dependent μ close to μ_{Hall} is extractable from eq. 5.26, if we know V_{th} and R_s. **e-f**, shows μ_{eff} as a function of the subtracted R_s and V_{th}, respectively, for various gate voltages. The parameter, V_{th}, becomes increasingly important as the voltage decreases, while R_s is more important at higher voltages. The information in panel a-f is useful for putting a constraint on V_{th} in the new fit-model. **g)**, fitting G_{2p} with eq. 5.25 again, after inserting the gate dependent μ_{model} defined by eq. 5.27. We used the same fit-range as for the original version of eq. 5.25, yielding a much better fit. **h)**, extracting μ_{eff} using the fit parameters from the fit in panel g for different constraints on V_{th} shows great similarity to μ_{Hall}.

the majority carriers are either electrons or holes[43]. The difference in applicability is that the density here: $C(V_g - V_{th})$, is directly measured in a Hall measurement, removing the capacitance and V_{th} as unknowns. Further, even if the threshold voltage and the capacitance are known parameters, eq. 5.26 is only directly implementable in the case of zero series resistances, which is practically impossible in a two-terminal measurement. Instead, the approach is to modify eq. 5.25 to contain a non-constant μ. The following μ-function is suggested:

$$\mu_{model} = \frac{1}{2}\left(\mu_1 + \mu_2 - \left([\mu_1 - \mu_2]^2 + M\right)^{\frac{1}{2}}\right) \tag{5.27}$$

This model of μ is based on qualitative features commonly observed for 2D InAs/InSb systems[47–49] above the percolation regime. Starting above percolation, in the intermediate density regime, the mobility rises approximately linearly in V_g because of the dominant role of the charged impurity scattering[81]. This is modelled as $\mu_1 = \alpha V_g + \beta$, for $\alpha \geq 0$. In the

high density regime, where inter-subband scattering becomes dominating, μ decreases linearly in V_g, modelled as $\mu_2 = \gamma V_g + \eta$, for $\gamma \leq 0$. The smoothness of the transition between the Coulomb scattering and inter-subband scattering, is believed to be partly determined by the density of the 2D-short range scattering sites, and modelled with the single parameter, M. By substituting μ_{model} into eq.5.25 the new fitting model will take the form:

$$G(V_g) = \Big(R_s + \frac{L^2}{\mu_{model} C(V_g - V_{th})}\Big)^{-1} \tag{5.28}$$

The new fit-model defined by eq. 5.28 enables us to find extract a gate-voltage dependent μ. Before fitting, we are able to constrain both R_s and V_{th}. R_s must be greater than 7.2 kΩ, the value of the resistors in the in-line filters. Upon introducing this constraint, one finds that the fits only converge for $V_{th} \leq$ -0.12 V. This is valuable information since judged alone from fig. 5.42a-d, values of V_{th} between -0.12 V and -0.08 V could not be excluded. However, going above V_{th} =-0.08 V, μ increasingly diverges at the border between the percolation regime and the start of the linear density regime around $V_{tg} = 0.05$ V as seen in 5.42d. This divergence-effect from overestimating V_{th}, is explained by the failure to account for a residual density at the start of the linear density regime. A better estimate of V_{th} can be inferred from the plots shown in fig. 5.42f. By expecting that the mobility is zero when the density is zero, these plots suggest a constrained value of $V_{th} \leq$ -0.1 V. Notice how, in the low gate voltage regime, the mobility becomes really sensitive to the chosen value of V_{th}, while in the high voltage regime it is most sensitive to the chosen value of R_s (see fig. 5.42e), since R_s dominates over R_{device} in this regime.

In fig. 5.42g, a fit to the two terminal measured conductance of device Fg1HB4 is shown using our new model with a fixed $V_{th} = -0.16$ V. Due to the large number of parameters in the new model, it fits equally well when using a range of V_{th} between -0.12 V and -0.20 V. Thus, the information in fig. 5.42a-f has to be used to fix the value of V_{th} in the model. However as shown in 5.42h , the mobility is quite robust to small variations in V_{th} once narrowed down to a range that yields a density close to the true density. The three fits in 5.42h use three different constraints on V_{th} of -0.12 V, -0.16 V and -0.20 V which yields R_s values of 7.2 kΩ, 7.4 kΩ and 7.5 kΩ, respectively. This is consistent with what we expect from the interpretation of the data in fig. 5.42a-c. Further, they show an excellent match to the mobility extracted from the reference Hall measurement. In appendix A4, conductance fits and gate voltage dependent μ's of two more devices using this new method can be found.

5.2.2 Summary

In summary, we used a gate-tunable InAs SAG-NW device in a Hall bar geometry to evaluate the efficacy of state-of-the-art methods for extraction of FET mobility in a two-terminal configuration against the Hall effect mobility. We found both methods to extract FET mobility fail to accurately capture the carrier density-dependent nature of μ, and severely overestimates the value by a factor of two. We therefore suggested a new model of the conductance that included a carrier density *dependent* mobility. From this we were able to extract an effective mobility that showed great similarity to the Hall-mobility and conclude that the new method can be used to extract more precise values of the mobility, but more importantly, be used to gather invaluable information of scattering mechanism in a particular density regime that can be used to optimize future devices.

Chapter 6

Correlated Materials

When I was a second year undergraduate student, I took my first introductory course in condensed matter physics. During this course, superconducting "magic angle graphene"[82] was discovered. This sparked my interest in correlated materials. The theoretical platform used to describe electron correlations goes beyond traditional band theory. Here this platform will be introduced in the light of the Hubbard model with focus on the 2D correlated lattices that we aim to successfully fabricate. The Hubbard model, is an extension of band theory that takes into account the electron-electron interactions. From this very simple, yet computationally intractable theory, electronic and magnetic properties that are not predicted by simple band theory emerges to give, for example, a more diversified picture of what a conductor is. The chapter ends with a status on the fabrication/growth process of SAG 2D square lattices followed by band diagram calculations that will help the future effort in preparing Hubbard Hamiltonian states, starting from the synthesis of the devices.

6.1 Beyond Band Theory

A simple treatment of band theory predicts that any system where the unit cell has a single valence electron is a metal[83]. However, there are cases where this is not true[84,85]. The problem is that band theory leaves out the effect of Coulomb-interaction between electrons[86]. We know that this non-interacting electron picture at least fails to describe the effect of: magnetic ordering (magnets or Mott-insulators), crystal field splitting and the Jahn-Teller distortion (charge density waves and Peierls distortion in 2D and 1D, respectively)[84,87]. Common to all these phenomena is the breaking of some symmetry that creates a new energetically favoured ordered ground state. To give an example where simple band theory predicts a metal but a more sophisticated treatment predicts a band gap, consider a 1D-chain of equally spaced H-atoms, separated by the distance 'a', each with a single 1s orbital and a single electron. If each lattice point is label by an index, $n = 0, 1, 2, 3..$ and contain a basis function, Bloch functions can be formed from[25,88]:

$$\psi_k = \frac{1}{\sqrt{N}} \sum_n e^{ikna} \chi_n \tag{6.29}$$

For example, at $k = 0$ and $k = \pm\frac{\pi}{a}$ eq. 6.29 becomes:

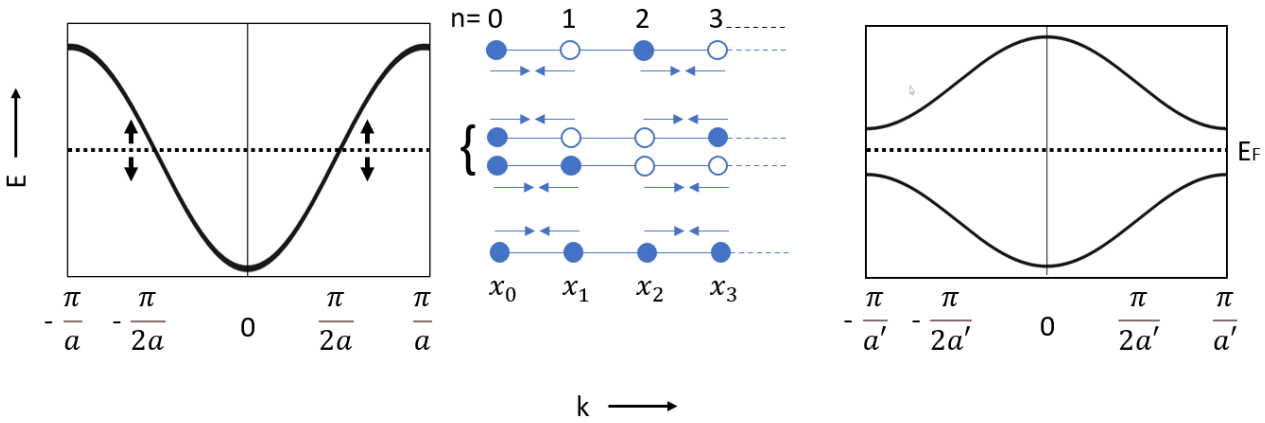

Figure 6.43: A schematic illustrating the idea of a Peierls distortion. The figure to the left shows the E-k diagram of a 1D H-atom chain equally spaced by 'a'. The Fermi level is placed at the center of the band indicating a half filled first Brillouin zone. This dispersion predicts a metal, however, at finite temperatures it is unstable to symmetric electron-phonon coupling pairing that distorts the chain and opens a band gap opening as shown by the black arrows. The Bloch functions are schematized in the middle, where the blue and white circles have opposite phases, meaning that there is a nodal point centered between them. The low-to-high energy functions, $k = 0$ - $k = \pm\frac{\pi}{a}$, are shown from bottom-to-top. Without the Peierl's distortion, all k-states are degenerate between $k = 0$ and $k = \pm\frac{\pi}{a}$. The symmetric pairing, indicated by the blue arrows, lifts the degeneracy at $k = \pm\frac{\pi}{2a}$ and opens a band gap. The opening of the band gap is shown in the right figure. The dimerization cause a doubling of the length of the unit cell such that a' = 2a.

$$\psi_0 = \chi_0 + \chi_1 + \chi_2 + \chi_3 + ...$$

$$\psi_{\pm\frac{\pi}{a}} = \chi_0 - \chi_1 + \chi_2 - \chi_3 + ...$$

The solution to the Schrödinger equation, using eq. 6.29 as an ansatz, can be seen in fig. 6.43 left. In the central part of fig. 6.43, an illustration of the Bloch functions for $k = 0$, $k = \frac{\pi}{2a}$ and $k = \frac{\pi}{a}$ are shown. Since every unit cell is filled with one valence electron, the first Brillouin zone is half filled and with a $E(k) = E(-k)$-degeneracy. At first, no band gap is present and the 1D-chain should be a metal. But at temperatures, T, on the order of $k_BT \approx E_F exp(-\frac{1}{\lambda_{el-ph}})$, where λ_{el-ph} is the electron-phonon coupling constant[87], Peierls instability states that: "a 1D metal is always unstable to a structural distortion that opens a band gap"[89]. If we imagine the symmetric pairing vibration as indicated by the arrows in fig. 6.43 middle panel, it turns out that this electron-phonon coupling, distorts the lattice such that it opens a band gap around the Fermi energy. The argument goes as follows: From

symmetric pairing a dimerization process causes every even-odd numbered site to move closer to each other and every odd-even numbered site moves further apart. Consider now the $k = 0$ state. Here, the energy gained in bonding energy by the electrons that moves closer, is lost by those that moves further apart, so no stabilization happens here. The same would be true for a possible $k = \frac{\pi}{a}$ state. However, at $k = \pm\frac{\pi}{2a}$ the effect of the dimerizations is dramatic. Here the $E(k) = E(-k)$ degeneracy will be lifted, since for one of the $k = \pm\frac{\pi}{2a}$ states both the bonding and anti-bonding energy will decrease, while it will increase for the other. The band gap opening is shown in fig. 6.43 right panel. A new periodicity is introduced, where the unit cell now has the length a'=2a. Consequently, the first Brillouin zone is halved. The new periodicity is defined by the "nesting vector", which in this example is a 1D vector that connects $-\frac{\pi}{2a}$ to $\frac{\pi}{2a}$. In general the nesting vector connects parallel lines of the Fermi surface to define a new Brillouin zone. It therefore requires a highly symmetric Fermi surface. Peierls instability is an example of the extreme importance of the concept of nesting to the interaction effects.

6.2 The Hubbard Model

The tight binding approximation predicts that the 1D H-atom chain is a metal with energies given by:

$$E_k = \alpha + 2\beta \cos k_x a \tag{6.30}$$

Here α is the on-site energy of an isolated H-atom and β is the interaction between two adjacent H-atoms in the nearest neighbour approximation. Consider a thought experiment: Ignoring the Peierls distortion, what happens if the lattice spacing is gradually increased? - As the lattice spacing increases the interaction between adjacent atoms decrease an the bandwidth narrows. The effective mass of the electrons will increase and make it a poorer conductor due to a decrease in the curvature of the band. Nonetheless, band theory still predicts that it is a metal, no matter how far apart the atoms are. This is nonphysical and there must be a critical length where it abruptly transitions into an insulator. For example, when the interaction energy of the atomic orbital becomes small compared to the energy associated with electron-electron interactions. In that case we can instead use the Hubbard model[90–93]. The Hamiltonian of the fermionic Hubbard model, referred to as the Hubbard Hamiltonian (HH), is the tight binding Hamiltonian with an additional term describing the repulsive Coulomb force between two electrons sharing a site. Using second quantization it

can be written as[94]:

$$\hat{H}_{Hubbard} = -t \sum_{\sigma=\uparrow,\downarrow} \sum_{<ij>} (c^{\dagger}_{i\sigma} c_{j\sigma} + c^{\dagger}_{j\sigma} c_{i\sigma}) + U \sum_{i} (n_{i\uparrow} + n_{i\downarrow} - 1)^2 - \mu \sum_{i} (n_{i\uparrow} + n_{i\downarrow}) \quad (6.31)$$

The lattice is indexed by sites i, j and the symbol $< ij >$ in the sum refers to the fact that the sum includes nearest neighbors only. The operator, $c^{\dagger}_{i\sigma}/c_{j\sigma}$, creates/annihilates an electron of spin $\sigma =\uparrow,\downarrow$ at site i. The operator, $n_{i\sigma} = c^{\dagger}_{i\sigma} c_{i\sigma}$, counts the number of spin up electrons at site i. The first term is the usual "hopping" energy known from the tight binding model. The second term is the "interaction" energy that will penalize double occupancy of a site with the energy U. The final term is the chemical potential that controls the filling. An illustration of the Hubbard model in the case of a 2D square lattice can be seen in fig. 6.44a. It is instructive to look at the HH in the limits of $U \gg t$ and $t \gg U$. In the limit of very large U ($t = 0$), it is in particular interesting to consider the average site occupancy as a function of the chemical potential (See fig. 6.44b). At small temperatures, this function will be step-like with a plateau centered around $\mu = 0$ at half filling. The width of the plateau is $2U$ at $T = 0$ and is known as the "Mott insulating gap". Inside this gap it is not possible to add or remove

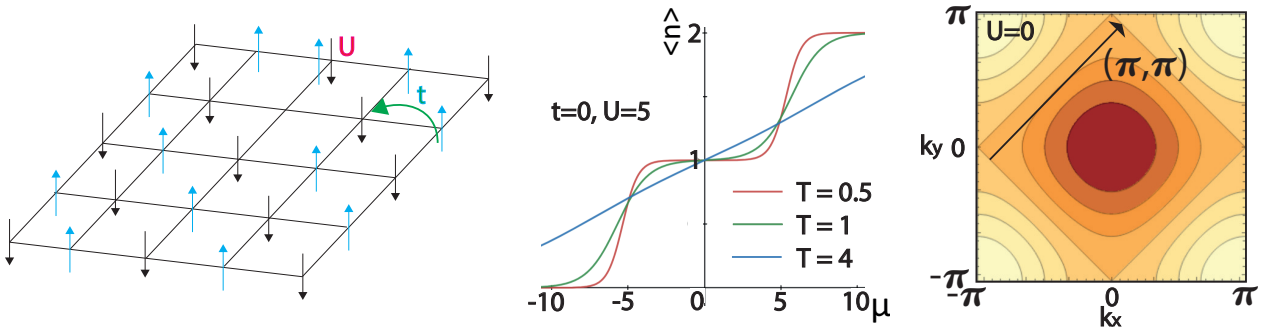

Figure 6.44: a), illustration of the square lattice Fermi-Hubbard model at half filling. In the limit of $U \gg t$, the fermions can lower their kinetic energy (t), by making occasional jumps to the neighbouring site but it comes with a price of U in potential energy. **b)**, The average site occupancy as a function of the chemical potential, μ, at half filling for $t = 0$ and $U = 5$ for different temperatures, T. A Mott insulating gap arises at small temperatures, freezing the average occupancy at $< n >= 1$ over a distance of $\Delta\mu = 2U$. A second order perturbation in t, demonstrate antiferromagnetic order inside the Mott gap. As T increases, the Mott gap smears out. **c)**, In the opposite limit for $U = 0$, the square lattice HH reduce to a tight binding Hamiltonian. Interestingly, at half filling the nesting (π, π)-vector cause a lattice step translation equivalent to a spin flip order and the wave function demonstrates antiferromagnetic order.

electrons. Increasing the temperature will smear the step-like function and narrow the Mott gap. Using second order perturbation theory in hopping, in the large U limit, it can be shown that at half filling the 2D Hubbard model reduces to the Heisenberg model and prefer antiferromagnetic ordering. Qualitatively, this can be understood from the particle-in-a-box perspective where the electrons can lower the kinetic energy by making the box larger from occasional visits to the neighbouring site. Due to Pauli principle, this is only possible if the neighbour has opposite spin and consequently - when it is at the neighbouring site - it only has the possibility to hop back to the empty site again. In the opposite limit of HH, $U = 0$, the solution of the square lattice is similar to eq. 6.30 but with an additional k_y dependent cosine function, $E_k = -2t(\cos k_x + \cos k_y)$. A contour plot of the E-k dispersion at different fillings is shown in fig. 6.44c, for a lattice spacing of $a = 1$. Equivalent to the Peierls distortion discussed earlier, the non-interacting square lattice has perfect nesting at half filling. The (π, π) wave-vector maps a large portion of the Fermi surface onto itself. Interestingly, the wave function demonstrates an antiferromagnetic order, a lattice step translation being equivalent to a spin flip order at half filling and $U = 0$, as was the case in the opposite limit[95]. Thus if nesting is achieved, the value of U is not so important in developing an ordered ground state.

6.3 A Closer Look at the Hubbard Parameters

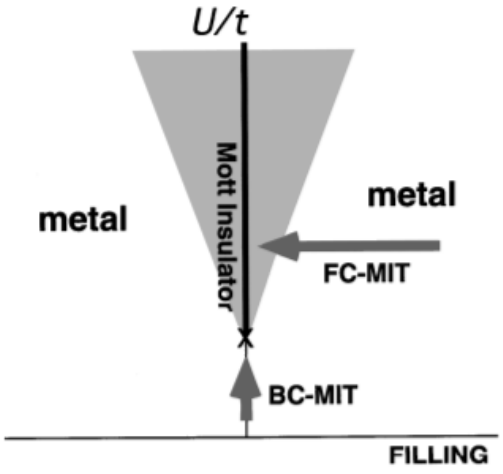

Figure 6.45: Metal-insulator phase diagram with the three parameters of the HH represented on the axes. The parent Mott insulator is shown at half-filling ($\mu = 0$) above U_c. Adjacent to $\mu = 0$ the filling controls if the phase is metallic (white regions) or strongly influenced by the MIT (grey regions). Adapted from[1].

In the previous section the extreme cases of the square lattice HH was considered. Now we will consider the ground state in the case where either t, μ and U are necessarily zero. The energy difference between the lowest and highest allowed state in a given band is defined as the bandwidth. The bandwidth parameter, W, is particularly important in partially filled bands, because it quantifies the decrease in total kinetic energy for all the electrons, if their atomic orbitals merge to overlap in real space[84]. The closer the atomic orbitals move, the more the band spread out. In the case of the square lattice $W = 8t$. In a partially filled band, for a given Hubbard-U, band theory is only a good approximation as long as $W > U$. That is, if the decrease in energy from hopping is larger

than the increase in energy from occupying the same atomic site. The transition, that a half filled band undergoes from $W > U$ to $W < U$, is called the bandwidth controlled (BC) metal-insulator transition (MIT)[96]. The phase diagram of the MIT is shown in fig. 6.45. The white regions are metallic and the shaded region is in principle metallic but under strong influence of MIT[1]. Moving parallel to the y-axis is the route of the BC-MIT, quantified by the ratio, $\frac{U}{t}$ with a finite value of U. Standing at half filling ($\mu = 0$) and taking the BC-MIT route (black fat arrow) drives the Mott insulator, where the metal-insulating phase is sharply divided at a critical $U = U_c$, below which the partially filled band is always metallic. In the situation where there is perfect nesting $U_c = 0$ as was discussed in the previous section. Above U_c at non integer filling the phase is usually metallic. However, moving parallel to the x-axis - the route of filling controlled (FC) MIT - to phases near $\mu = 0$ are of particular interest. Here, more exotic phases are found e.g., unconventional superconductivity, first discovered by Bednorz and Müller in 1986[97], where the Mott insulator is driven towards a superconducting phase. The Mott-superconductor (MS) phase transition gained a lot of interest after its discovery since the mechanism leading to superconductivity could not be described by BCS theory and some MS-materials showed extraordinary high critical temperatures (≈ 100 K).

6.4 Preparing a Hubbard Hamiltonian Simulator

The three parameters of the HH have a deceptive simplicity but the complexity of calculations increases exponentially with the number of particles[98] and makes it an insurmountable task for a classical computer to simulate for more than a few particles. To overcome the mathematical task of solving many-body problems, a quantum simulator was suggested by Feynman in 1982[99]. With an analog Hubbard lattice quantum simulator the idea is to map the HH of the system and then prepare the simulator in a state relevant for the physical problem of interest[3]. In this section the formalism for calculations of band diagrams of experimentally realisable square lattices is introduced. The calculations will aid the experimental effort of tuning in on the right parameters that makes the HH a useful model to describe the physics of the SAG Hubbard lattices (HL).

A crucial assumption of the HH is that the particles are all in the lowest Bloch band. That is, when preparing a HL, it is desirable to have the Bloch waves localized on the lattice sites, such that the eigenvalues are less dispersed. In fig. 6.46 left, a schematic of an idealized HL is shown. The green consist of a metallic/semiconducting material (e.g. InAs or InGaAs) and the blue consist of an insulating material (e.g. SiO_x). Ideally, the electron orbitals are localized in the junctions of the metallic/semiconducting material to define a lattice site. The

Kronig-Penney (KP) model[100] is a useful tool to help tuning in on the parameters that fulfills the desirable conditions. Following the method in ref.[101], a 2D KP square lattice with the most simple potential - the square potential - embedded in an infinite square well (ISW), will now be considered. The model is illustrated in fig. 6.46. with the square lattice implying that the lattice constants in both directions are $a_x = a_y = a$. A schematic of potential in the unit cell normalized to a, is seen in fig. 6.46, right, and the normalized distances $P_{2,x} - P_1 = P_{2,y} - P_1$. The strength of the square potential is V_0.

It then follows that the Hamiltonian is:

$$H = H_0 + V(x, y) \tag{6.32}$$

Where $H_0 = -\frac{\hbar^2}{2m_0}\frac{\delta^2}{\delta x^2} + V_{inf}(x, y)$ is the ISW Hamiltonian, with a ground state energy $E_{ISW} = \frac{\hbar^2\pi^2}{2m_0a^2}$. The periodicity of the lattice implies that the wavefunction satisfies:

$$\psi(x + a_x, y) = \psi(x, y) \tag{6.33}$$

$$\psi(x, y + a_y) = \psi(x, y) \tag{6.34}$$

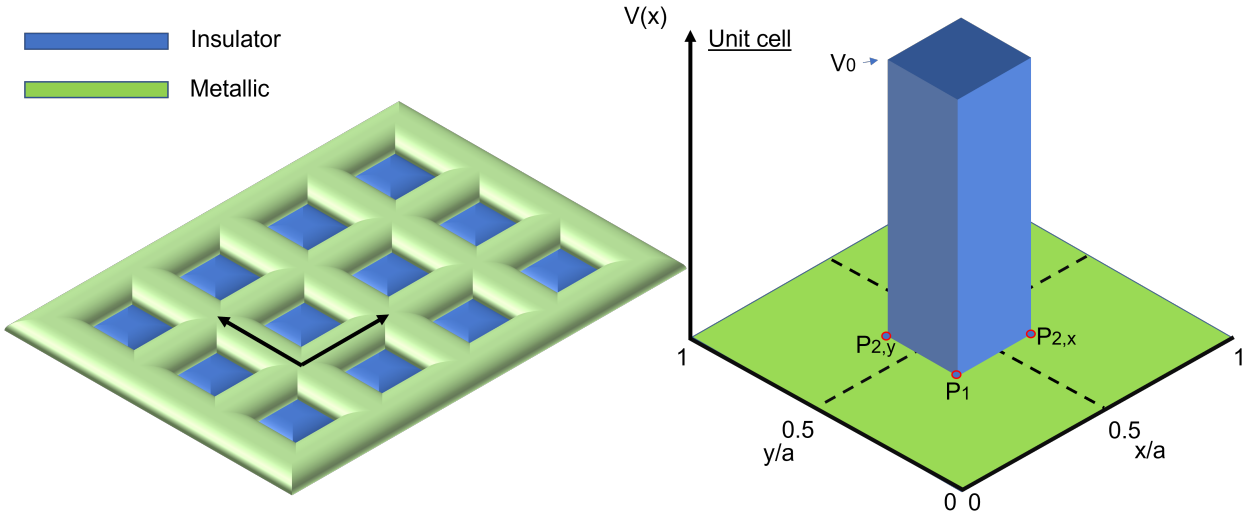

Figure 6.46: The 2D square lattice Kronig-Penney model. **Left,** A model of the square lattice with metallic regions in green and insulating regions in blue. Ideally, the Bloch waves localizes in the junctions of metallic material. The unit cell is indicated with lattice vectors (black arrows). **Right,** The unit cell in potential energy vs real space. A simple square potential arising from the insulating material is considered with parameters $P1$ and $P2$ defining the area of the square potential and V_0 the potential height.

and has orthonormal plane-wave basis states:

$$\psi^{(0)}_{n_x n_y}\Big(x,y\Big) = \frac{1}{a}\exp\Big(i\frac{2\pi}{a}(n_x x + n_y y)\Big) \tag{6.35}$$

Where $n = .. -2, -1, 0, 1, 2...$, and the superscript (0) indicates the free electron eigenstates/eigenvalues. The eigenvalues are:

$$E^{(0)}_{n_x n_y} = 4\Big[n_x^2 + n_y^2\Big]E_{ISW} \tag{6.36}$$

Turning on the potential, $V(x,y)$, the matrix elements become:

$$\begin{aligned} H_{n_x n_y, m_x m_y} &= \langle \psi^{(0)}_{n_x n_y} \mid H_0 + V(x,y) \mid \psi^{(0)}_{m_x m_y}\rangle \\ &= \delta_{n_x m_x}\delta_{n_y m_y}E^{(0)}_{n_x n_y} + H^V_{n_x n_y, m_x m_y} \end{aligned} \tag{6.37}$$

Imposing Bloch's theorem to eq. 6.33 and 6.34 modifies eq.6.36 and leads to the following term on the diagonal of the matrix in dimensionless units:

$$\frac{E^{(0)}_{n_x n_y}}{E_{ISW}} = \Big[\Big(2n_x + \frac{\boldsymbol{K_x}a}{\pi}\Big)^2 + \Big(2n_y + \frac{\boldsymbol{K_y}a}{\pi}\Big)^2\Big] \tag{6.38}$$

Where $-\pi \leq \boldsymbol{K_{x/y}}a \leq \pi$ is satisfied. The embedding potential yields a contribution to the diagonal elements and the off-diagonal elements. These terms are found from the solutions to the integral of:

$$h^V_{n_x n_y, m_x m_y} = v_0 \int_{P_1}^{P_2}\int_{P_1}^{P_2} \delta x \delta y \exp\Big(i2\pi(m_x - n_x)x\Big)\exp\Big(i2\pi(m_y - n_y)y\Big) \tag{6.39}$$

Where $h^V_{n_x n_y, m_x m_y}$ is the dimensionless form of $H^V_{n_x n_y, m_x m_y}$ i.e. v_0 is $\frac{V_0}{E_{ISW}}$ and P_1/P_2 are just points in k-space normalized to a. . This integral has an analytic solution:

$$\begin{aligned} h^V_{n_x n_y, m_x m_y} = v_0\Big[(P_2 - P_1)\delta_{n_x m_x} + i\frac{(e^{i2\pi(m_x - n_x)P_1} - e^{i2\pi(m_x - n_x)P_2})}{2\pi(m_x - n_x)}(1 - \delta_{n_x m_x})\Big] \\ \times\Big[(P_2 - P_1)\delta_{n_y m_y} + i\frac{(e^{i2\pi(m_y - n_y)P_1} - e^{i2\pi(m_y - n_y)P_2})}{2\pi(m_y - n_y)}(1 - \delta_{n_y m_y})\Big] \end{aligned} \tag{6.40}$$

Notice that the contribution from the embedding potential to the diagonal elements is just the volume of the square potential. From equations 6.38 and 6.40 a matrix can be constructed using $(n_x, n_y) = (0,0), (0,1), (0,-1), (1,0), (-1,0), (1,1), (1,-1), (-1,1), (-1,-1), (2,0)...$ up

to some value n_{max} in both x and y that secures a desired level of convergence. Then $\boldsymbol{K_x}$ and $\boldsymbol{K_y}$ are swept while diagonalizing the matrix to construct the 2D E-**K** diagram.

6.5 Realizing Square Hubbard Lattices - Initial Phase

In the previous section, the formalism for calculating eigenvalues and eigenstates of a 2D square lattice with a square potential was developed. In this section the KP-model is applied to

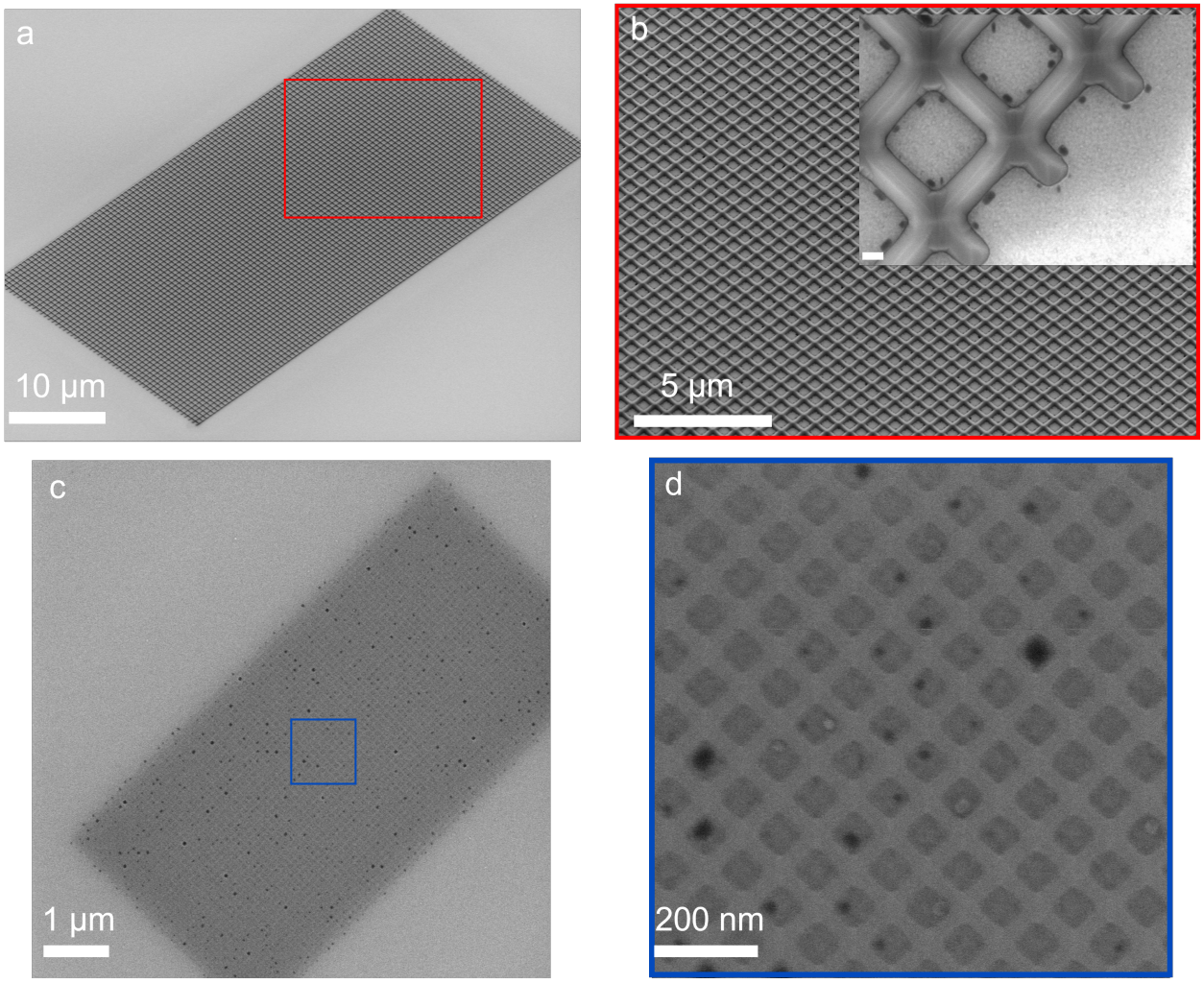

Figure 6.47: SEM images of 2D square lattices. **a,** A tilted SEM image showing a lattice with only the buffer, GaAs(Sb) grown inside the SiO_xmask-openings. The lattice consists of 40x80 lattice point. **b,** a higher resolution of the red box in a. The inset shows the highest resolution, where defects in the mask become visible. **c,** a SEM image of a lattice with a thin layer of ≈ 2 nm InGaAs grown on top of the buffer. This lattice had a pitch and width of 100 nm and 75 nm, respectively. **d,** a higher resolution of the blue box in c.

construct band diagrams and ground state wavefunctions (WF), based on estimated parameter values from the synthesized lattices shown fig. 6.47. A discussion of the results follows with a focus on how to tune the parameters such that a regime close to the tight-binding regime is reached. That is, 1) we want the orbitals to be localized on each lattice site 2) we want a large band-gap from the lowest Bloch band to higher bands 3) we want a flat Fermi surface at half-filling to be able to achieve nesting that allows for an ordered ground state (e.g. charge density wave, antiferromagnetism, etc) regardless of a small Hubbard-U.

To set the stage, let us look at some of the grown HL. The initial phase required an effort in optimizing the MBE and lithographic processes and was carried out by my colleagues Daria Beznasyuk & Damon Carrad. Figure 6.47 summarizes the status of the square HL. It was grown using a SAG method similar to that described in chapter 3 and shown fig. 3.10. In fig. 6.47a, a tilted SEM image of a HL is shown, where only the buffer GaAs(Sb) has been grown in the mask-openings. The mask consists of SiO_x. The lattice has 40x80 lattice sites with a pitch (lattice spacing) of 500 nm. Figure 6.47b, is a higher resolution image of the same lattice enclosed by the red box in fig. 6.47a. The inset figure shows the highest resolution, where small defects in the mask become visible. These defects have not been included in the preliminary calculations considered in this thesis but will be the subject of future work. In fig. 6.47c, lattice with a pitch of 100 nm is shown. This lattice had a very thin layer of ≈2 nm InGaAs grown on top of a 10 nm GaAs(Sb) with a 10 nm tall SiO_x layer. With this small pitch, the defects take up more space of the square lattice unit cell as seen in fig. 6.47d. Thus, a larger effect on the transport properties is expected which might undermine the quantitative conclusions that can be drawn from the simple calculations shown in this section. However, even though this simple model neglects the influence from defects and effects from edges states due to a finite amount of lattice sites, the qualitative trends are still believed to be useful for future optimization purposes.

The pitch and the effective mass of the metallic material determines bandwidth of the lowest Bloch band, E_{ISW}. Based on the images in fig. 6.47c&d, pitches between 75-100 nm and effective masses ranging from (0.023-0.050)$\cdot m_0$, where m_0 is the electron mass, are used, giving E_{ISW} between 0.75-2.91 meV. The height of the square potential, v_0 is determined by mismatch between the conduction band edges of the metallic and insulating material. This value is unknown but the unnormalized value, $V_0 = v_0 \cdot E_{ISW}$, is assumed to be on the order of a few eV. The value of v_0 is set, depending on E_{ISW}, to match a realistic scenario. The last parameter defines the area of the square potential and is given as the ratio between the area of the insulator, A_I, and the area of the metallic region, A_M in a unit cell. This ratio is settled during synthesis by controlling the width and the pitch of the mask openings.

6.5.1 *Band Diagrams*

The first Brillouin zone of a square lattice is shown in fig. 6.48. Eigenvalues of the KP-model were traced out between high-symmetry points in crystal momentum from the Γ-point → X'-point, X'-point → M-point and from M-point → Γ-point and are shown in fig. 6.49 for two different area ratios $\frac{A_I}{A_M}$. All eigenvalues are normalized to E_{ISW}. In the tight-binding limit at half-filling the Fermi surface is a square rotated 45° in the first zone and takes up $\frac{1}{2}$ of the total area. To achieve nesting, the path along the Fermi surface, indicated by the purple arrow in fig. 6.48, must be flat. The eigenvalues along this path are plotted in the narrow band diagram in fig. 6.49 and shows that as the insulator takes up more space of the unit cell a tight binding limit is approached with a flat Fermi surface. When the insulator takes up 25% of the area of the unit cell ($P_1 = 0.25$ and $P_2 = 0.75$) i.e. when the width of the insulator equals the width of the metallic grid-arms , the lattice is already set up for nesting. At this setting the band gap from the lowest Bloch band is $\approx 2E_{ISW}$, which then makes the effective mass and the pitch important parameters for comparing the energy scale of the band gap to an energy scale from effects such as impurities, temperature etc. From the view of the band gap, these parameters must be minimized.

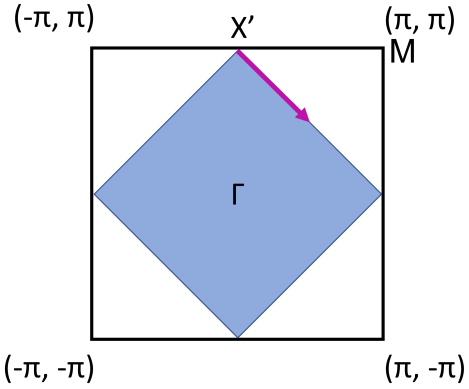

Figure 6.48: The first Brillouin zone of a square lattice. The high symmetry points are defined at $\Gamma = (0, 0)$, $X' = (0, \pi)$ and $M = (\pi, \pi)$. the Fermi surface at half-filling is a square (blue). Tracing out the eigenvalues of the KP-model along the Fermi surface (purple arrow), in the tight-binding limit is flat which indicates perfect nesting.

6.5.2 *Ground State Wavefunctions*

Figure 6.50 shows a matrix of calculated charge densities in real space, $|\psi_0(r)|^2$, at **K=0** (Γ-point). The ratio between A_I and A_M is varied on the y-axis and V_0 is varied on the x-axis. The dark regions are nodes in the charge density. As the insulator takes up more space, the Bloch WFs contract and accumulate in the junctions of the metallic material (bright regions). This shows that it is possible to generate localised orbitals without the need to fabricate gates that will act as tunnel barriers to "disconnect" neighbouring orbitals and is consistent with

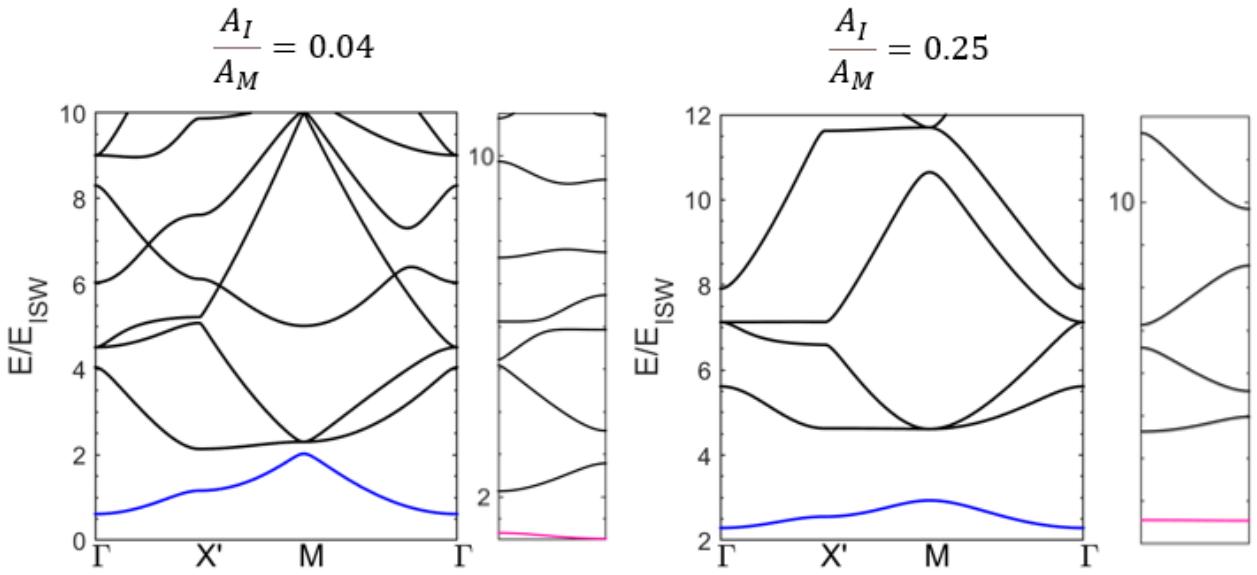

Figure 6.49: Band diagrams of a 2D-square lattice. When the area of the insulator, A_I, in the unit cell is small, left plot, the band gap from the lowest Bloch band (blue band) to higher ones is small compared to the band gap when A_I is larger as seen in the right plot. The dispersion along the path shown in fig. 6.48 at half-filling (purple) is shown in the narrow band diagrams. The tight binding limit is reached when A_I is 25 % of the unit cell and at half-filling of the lowest bloch band the Fermi surface is flat. In this situation the Fermi surface is nested.

what was inferred from the band diagrams that a width/pitch ratio ≤ 1 is desirable. However, from the variation in V_0, here shown by letting v_0 take values from 10-10^4, it is noticed that a larger v_0 gives the most localized WFs which suggest that a larger pitch/effective mass or smaller conduction band mismatch is desirable. The least complicated parameter to vary from an experimental point of view would be the pitch. But there is a trade-off between increasing the pitch to get more localized WFs and having a large band gap to higher Bloch bands. To give an example of this dilemma, consider the HL in fig. 6.47d. The pitch is ≈100 nm and the width of the metallic arms ≈75 nm giving the ratio $\frac{A_I}{A_M} = 0.33$ and a $E_{ISW} \approx 1.5$ meV. Thus, the band gap from the lowest Bloch band to the closest higher band is ≈ 3.75 meV. If we assume a conduction band mismatch between the InGaAs and SiO_x is at a fixed values of a few eV, the representation of the orbitals can be placed somewhere between row 1 and 2, column 3 and 4 in fig. 6.50. In this case only a small reduction of the pitch down to ≈75 nm, would be beneficial to increase the band gap without risking to delocalize the WFs and lose the nesting property. A further reduction of the pitch would require engineering of local gates to increase to value of V_0.

6.5.3 *Summary*

In summary, we developed a simple model of the 2D square lattices using matrix mechanics to find solutions to the KP-model. From these solutions we were able to to construct band diagrams and calculate charge densities in real space, that - at least on a qualitative level - gives us insight into the relevant parameters that we can control to prepare a lattice in a state that can be described with the a simple HH. In the future we can elaborate on this model, e.g., consider different periodic potentials and add impurities or edge states, to obtain an even better and perhaps more quantitative understanding that can direct the synthesis process of the devices.

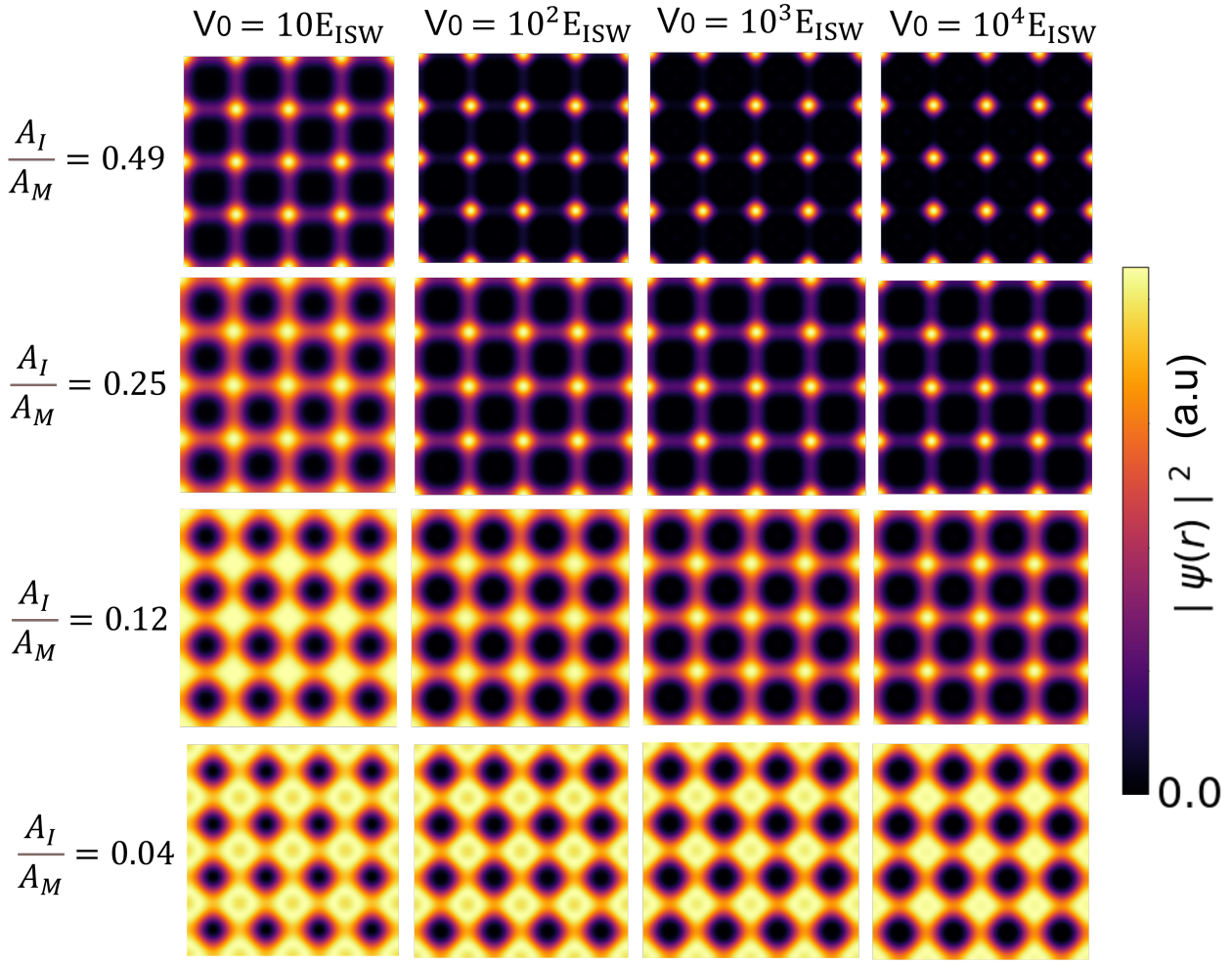

Figure 6.50: The electron density in real space $|\psi_0(r)|^2$. As the insulator takes up more space of the unit cell the density tends to accumulate in the junctions of the HL. An increasing conduction band mismatch, V_0, results in an increase of the localization of the electron density.

Chapter 7

Conclusion & Outlook

In every branch of knowledge the progress is proportional to the amount of facts on which to build, and therefore to the facility of obtaining data - James Clerk Maxwell

7.1 Conclusion

In conclusion, we did preliminary tight binding calculations on the 2-dimensional square Hubbard lattices with dimensions matching those of the most recent selective-area-growth synthesized lattices. We showed that it is possible to create localized orbitals in the junctions of the lattices and that we can achieve nesting to develop an ordered ground state.

We developed a method to accurately extract the gate voltage-dependent mobility from a two-terminal FET measurement that showed an excellent match with the Hall mobility. Our approach further enables systematic investigation of the underlying scattering mechanisms that determine the mobility in a particular carrier density regime.

We studied UCF, specifically, the statistics in normal-superconducting nanowires, which has not been done before and showed that it is possible to probe the underlying symmetries in a device from the amplitude of these fluctuations in different regimes.

7.2 Outlook

Universal Conductance fluctuations in Quasi-1D NS-Devices

The most immediate future work we will undertake is the repeat the experiments performed here with further devices and increased gate range to improve the statistical certainty of the claims made in chapter 5. For the next round of measurements, it would be interesting to have devices with a wide variety of different lengths of the N-part of the wire, in a range around the typical phase coherence lengths of these types of wires, to probe the l_ϕ-dependence of δG and test Beenakker and van Houten's interpolation formula in eq. 2.12.An extended analysis of control devices would also be desirable to assist determination of the UCF amplitude when both particle-hole and time-reversal symmetry are broken.

Carrier Density Dependent Mobility in Semiconductor Nanowires

With the new model of the gate-dependent mobility, we aim to build up statistics from two terminal measurements on similar systems. The collected statistics can be utilized to gain insight about the physical meaning of the parameters of the model which, for now, remain unknown. This will not only help us optimize the fit but also provide invaluable information about scattering mechanism that together with information about synthesis of the devices can help the optimization process towards less disordered materials.

Correlated Materials from SAG Hubbard Lattices

In the near future, we can test the quality of the developed KP-model from electron transport measurements by probing the insulating/conducting behaviour of several devices, i.e. is it possible to change the band gap or create localized/delocalized orbitals by tuning the parameters the way the KP-model predicts?

To elaborate on the model we can construct a more realistic potential and also add small random potentials in the unit-cell to probe the effect of impurities on the band structure. In the far future, it would be interesting to add edge states. For this we have to model a finite lattice.

Appendices

A1 NanoWireWeek Chamonix-Mont-Blanc April 2022

Carrier density-dependent mobility in semiconductor nanostructures

Christian E. N. Petersen[1], Damon J. Carrad[1,2], Thierry D. Pomar[2], Daria V. Beznasyuk[1,3], Jung-Hyun Kang[1,3], Gunjan Nagda[1,3], Dennis Valbjørn Christensen[2], Peter Krogstrup[1,3] and Thomas S. Jespersen[1,2]

[1] Center for Quantum Devices, Niels Bohr Institute, University of Copenhagen, Denmark
[2] Department of Energy Conversion and Storage, Technical University of Denmark, Denmark
[3] Microsoft Quantum Materials Lab Copenhagen, Denmark
Contact: lbc622@alumni.ku.dk

Increasing material quality and carrier mobility of semiconductor nanostructures is crucial in many applications for coherent nanoelectronics and nanotechnology. A challenge in this respect is the inherent difficulty in performing four-terminal Hall effect measurements on nanostructures, including nanowires [1] and prompts efforts to extract mobility in other ways. In materials where mobility is independent of carrier density, field-effect measurements can be used [2]. However, this situation seldom occurs in nanostructures, where density-dependent scattering mechanisms give rise to a non-constant – and in some cases non-monotonic – relationship between carrier mobility and density. In this study, we investigate the non-monotonous electron mobility in InAs nanowires in a Hall bar geometry made using selective area growth (Fig 1, left) [3,4]. We develop a method to accurately extract the gate voltage-dependent mobility from two-terminal field-effect transistor measurements and demonstrate an excellent match with the Hall mobility (Fig 1, right). Our method enables extracting similar information to a Hall effect measurement on two-terminal devices at zero magnetic field. Going beyond the conventional models which assume constant mobility – and significantly overestimate the true value – (Fig 1, right), our approach further enables systematic investigation of the underlying scattering mechanisms that determine the mobility in a particular carrier density regime. For example, Fig 1, right shows that our devices exhibited an initial rise in mobility with increasing gate voltage, followed by a fall beyond the peak around V_{tg} = 0.5 V. The two behaviours may be attributed to screening of charged impurities and inter-subband scattering, respectively [5].

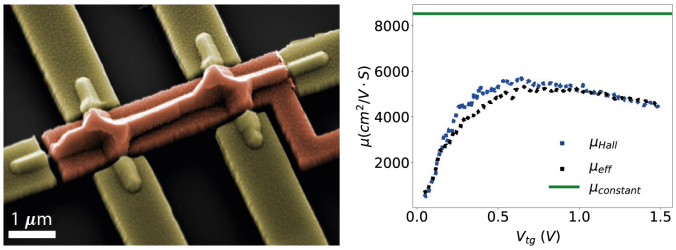

Figure 1 Left: False-colour scanning electron microscope of a selective-area-growth nanowire in a Hall bar geometry with Ti/Au contacts (yellow) and top gate (orange). Right: Mobility, μ, vs top gate voltage V_{tg}. Blue shows the Hall-mobility and black the gate-dependent effective mobility extracted from a two-terminal measurement. For comparison, we plot the constant mobility obtained from conventional field-effect techniques (green).

[1] K. Storm, et al., Nat Nano **7**, 718–722 (2012)
[2] S. M. Sze, Physics of Semiconductor Devices, 3rd ed. Hoboken, N.J: Wiley-Interscience (2007)
[3] F. Krizek et al., Phys. Rev. Materials **2**, 093401 (2018)
[4] D. V. Beznasyuk et al., arXiv:2103.15971 (2021)
[5] S. Ahn et al., arXiv:2109.00007 (2021)

Nanowire Week 2022, 25-29 April, Chamonix, France

Figure S51: The abstract that was accepted for a talk by the committee of the NanoWireWeek.

Appendices

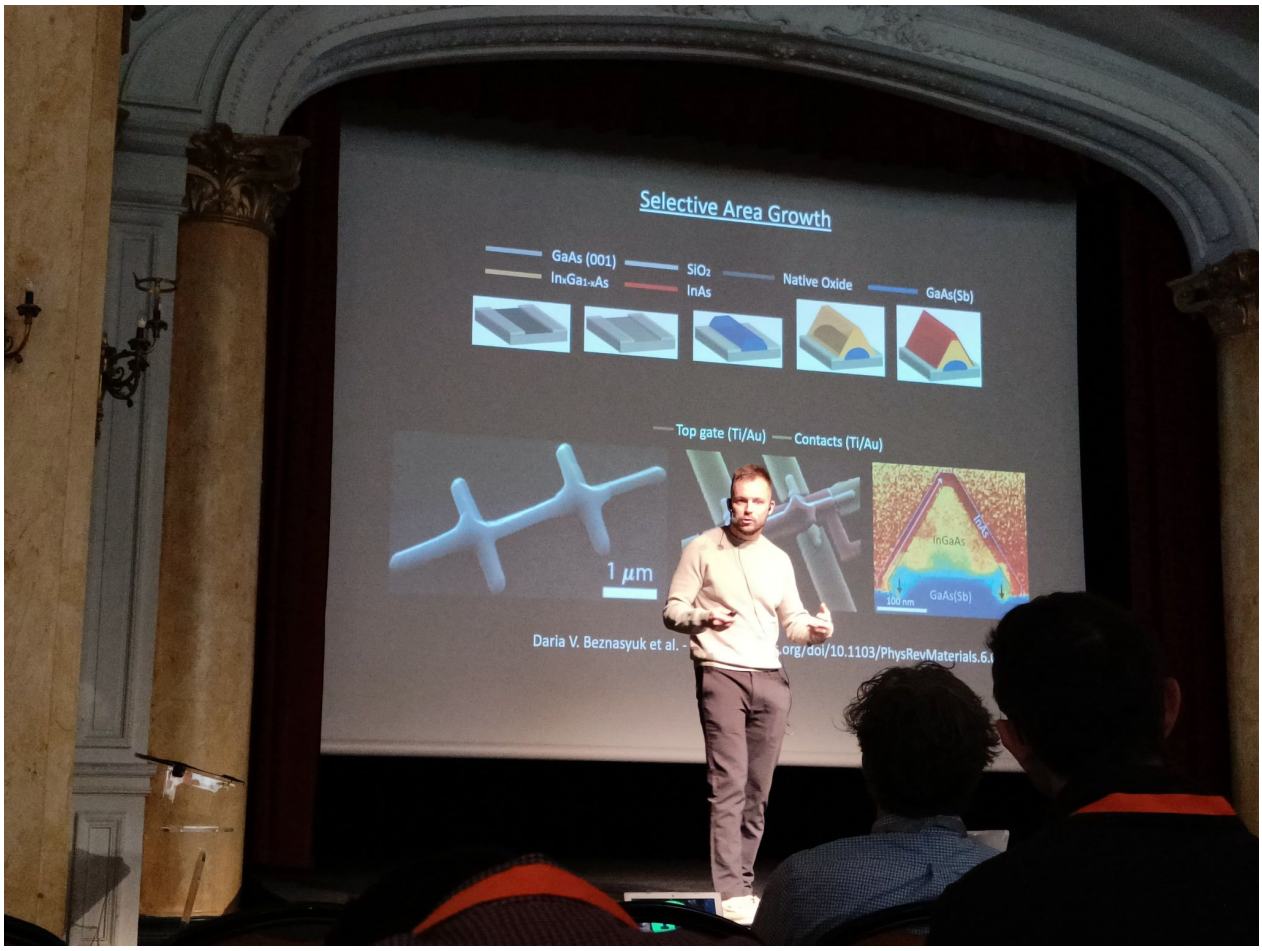

Figure S52: Me doing a talk about a new method to extract carrier density dependent mobility from a two-terminal field-effect transistor measurement at NanoWireWeek in Chamonix-Mont-Blanc. Date: 28th of April 2022.

Appendices

A2 Overview of Fabricated Devices

UCF Chips	
Device Name:	*Comments:*
CP1-1.00	Did conduct but had a side gate shorted to the source contact at the NS-device
CP1-0.70	Did not conduct
CP1-0.50	Did conduct at the NS-device. The reference device did not conduct. Device was unfortunately blown up with a side gate before starting to show interesting results
CP2-1.25	Did not conduct
CP2-0.85	Did not conduct
CP2-0.35	Did not conduct
CP3-1.25	Fabrication failed. Leads were misaligned to the wire
CP3-0.75	Fabrication failed. Leads were misaligned to the wire
CP3-0.50	Fabrication failed. Leads were misaligned to the wire

Appendices

UCF Chips	
Device Name:	*Comments:*
CP4-1.50	Fabrication failed. Leads were misaligned to the wire
CP4-1.00	Fabrication failed. Leads were misaligned to the wire
CP4-0.35	Fabrication failed. Leads were misaligned to the wire
CP5-1.50	did not conduct
CP5-0.75	2nd layer was overexposed causing different leads to overlap. Stripping the resist and make a new exposure worked and device conducted beautifully. Results shown in chapter 5
CP6-1.50	did not conduct. Might have been blown up during bonding
CP6-0.75	did not conduct. Might have been blown up during bonding

Appendices

Hall Bars	
Device Name:	*Comments:*
MQML22 Fg1HB4	results presented in appendixA4 fig. S54
MQML38 Fg1HB4	results presented in chapter 5
MQML38 Fe1HB4	Hooked up wrong
MQML38 Fg2HB5	results presented in appendix A4 fig. S54

A3 Fabrication Recipes

UCF chips

1. 1st Spinning of resist
   - A single drop of MicroChem PMMA A6 from a 1.5 ml pipette
   - Ramp up to 4000 rpm for 5 s and spin for 60 s.
   - Wait 30 s for the resist to settle
   - Clean the back of chip for resist with acetone
   - Bake on hot plate at 185° C for 60 s.

2. 1st exposure on Elionix 100 kV
   - Write-field size 300x300 $(\mu m)^2$
   - Area dose 950 $\frac{\mu C}{cm^2}$
   - Exposure time 0.475 $\frac{\mu s}{pixel}$
   - Beam current of 500 pA

3. 1st Develop
   - 60 s MIBK:IPA 1:3
   - 30 s IPA
   - Blow dry with nitrogen for 30 s
   - 60 s ash

4. Argon Milling
   - Struck a plasma 15 watts at pressure 18 Torr for 8 min.

5. 1st Titanium deposition 10 kV
   - e-beam current 32 mA
   - 5 nm thickness at a rate of ≈ 1 Å$/s$

6. 1st Gold deposition 10 kV
   - e-beam current 32 mA
   - 250 nm thickness at a rate of $\approx 1.5 - 2.0$ Å$/s$

7. 1st Lift-off
   - 50 °C acetone for 1 hour, use pipette to swirl lift off the resist if necessary,
   - Clean in IPA
   - Blow dry with nitrogen

8. ALD
   - Deposited a layer of 150 cycles pulse water $\rightarrow$ pump out, pulse precursor $\rightarrow$ purge at 110 °C to have a final layer of 15nm HfO_2.

9. 2nd Spinning of resist
   - Same as step 1

10. 2nd exposure on Elionix 100 kV
    - Same as step 2

11. 2nd Develop
    - Same as step 3

12. 2nd Titanium deposition 10 kV
    - Same as step 5

13. 2nd Gold deposition 10 kV
    - e-beam current 32 mA
    - 150 nm thickness at a rate of ≈ 1 Å$/s$

14. 2nd Lift-off
    - Same as step 7

A4 Carrier Density-Dependent Mobility in Semiconductor Nanostructures

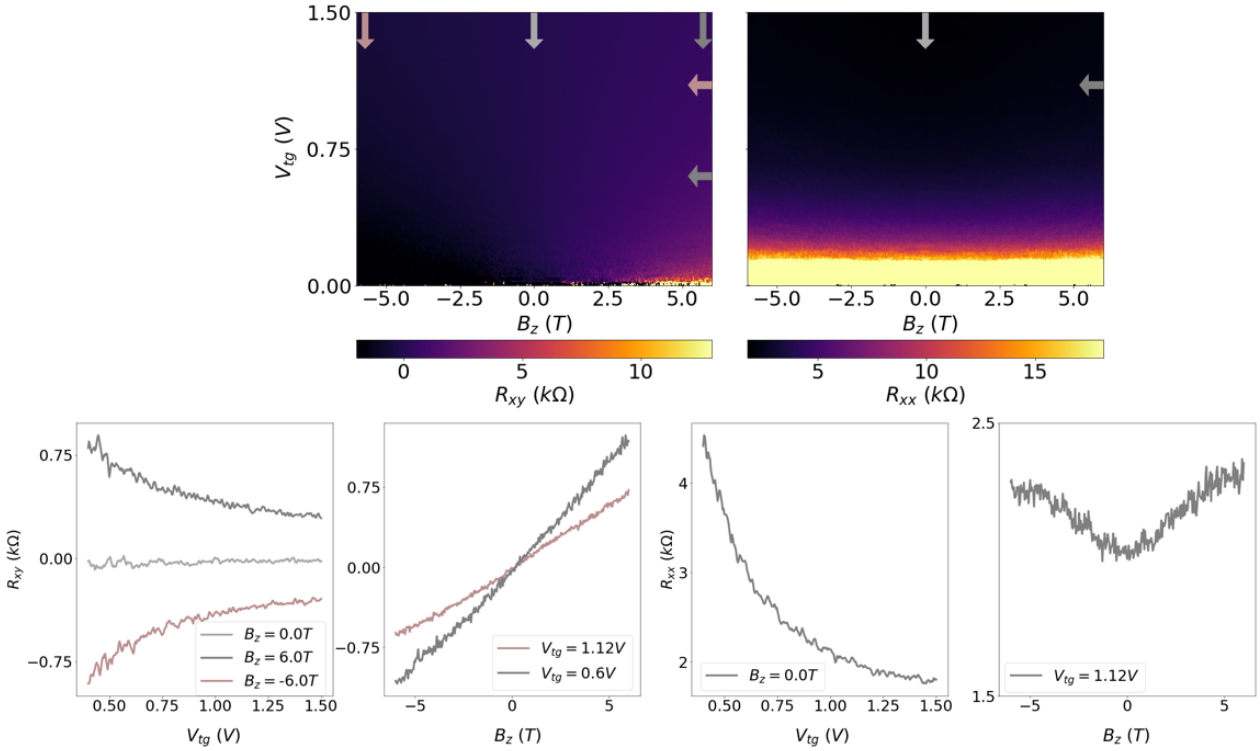

Figure S53: Raw data. The bottom row data was extracted from line traces indicated by the arrows in the top row 2D colormaps.

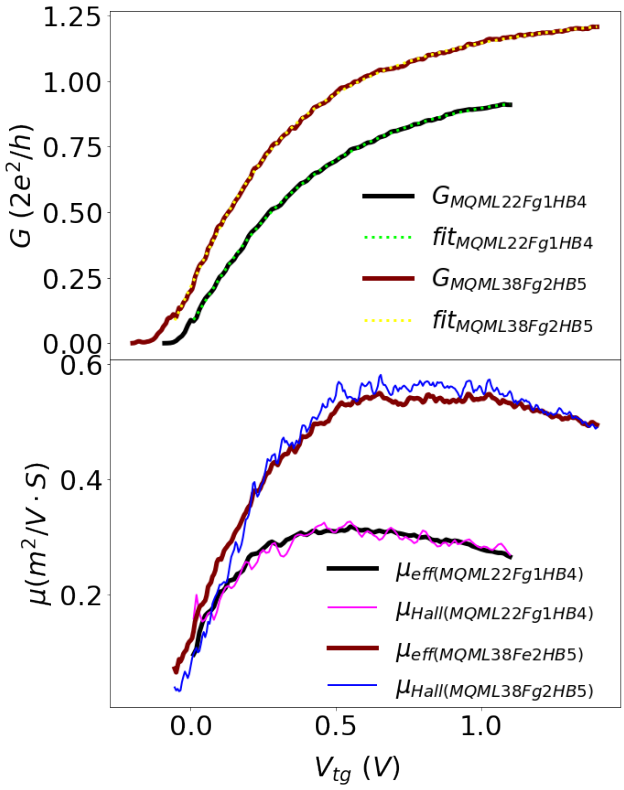

Figure S54: More fits to eq. 5.28. From the parameters extracted the effective mobility, showing great similarity to the Hall mobility, is found.

Bibliography

[1]M. Imada, A. Fujimori, and Y. Tokura, "Metal-insulator transitions", Rev. Mod. Phys. **70**, 1039–1263 (1998).

[2]P. Anderson, "Twenty-five Years of High-Temperature Superconductivity - A Personal Review", Journal of Physics Conference Series **449**, 2001 (2013).

[3]I. Bloch, J. Dalibard, and S. Nascimbène, "Quantum simulations with ultracold quantum gases", Nature Physics **8**, 267–276 (2012).

[4]P. Barthelemy and L. M. K. Vandersypen, "Quantum Dot Systems: a versatile platform for quantum simulations", Annalen der Physik **525**, 808–826 (2013).

[5]S. Ahn, H. Pan, B. Woods, T. D. Stanescu, and S. Das Sarma, "Estimating disorder and its adverse effects in semiconductor majorana nanowires", Physical Review Materials **5**, 10.1103/physrevmaterials.5.124602 (2021).

[6]K. Storm, F. Halvardsson, M. Heurlin, D. Lindgren, A. Gustafsson, P. M. Wu, B. Monemar, and L. Samuelson, "Spatially resolved hall effect measurement in a single semiconductor nanowire", Nature nanotechnology **7**, 718–722 (2012).

[7]A. V. Kretinin, R. Popovitz-Biro, D. Mahalu, and H. Shtrikman, "Multimode fabry-pérot conductance oscillations in suspended stacking-faults-free inas nanowires", Nano Letters **10**, 3439–3445 (2010).

[8]S. Alagha, S. Hernández, C. Blömers, T. Stoica, R. Calarco, and T. Schäpers, "Universal conductance fluctuations and localization effects in InN nanowires connected in parallel", Journal of Applied Physics **108**, 113704–113704 (2010).

[9]V. Hui and C. Lambert, "Andreev scattering, universal conductance fluctuations and phase periodic transport", EPL (Europhysics Letters) **23**, 203 (2007).

[10]W. J. Skocpol, "Conductance Fluctuations in Narrow Silicon MOSFETs", **T19A**, 95–101 (1987).

[11]W. J. Skocpol, P. M. Mankiewich, R. E. Howard, L. D. Jackel, D. M. Tennant, and A. D. Stone, "Nonlocal Potential Measurements of Quantum Conductors", Physical Review Letters **58**, 2347–2350 (1987).

Bibliography

[12]W. J. Skocpol, P. M. Mankiewich, R. E. Howard, L. D. Jackel, D. M. Tennant, and A. D. Stone, "Universal conductance fluctuations in silicon inversion-layer nanostructures", Physical Review Letters **56**, 2865–2868 (1986).

[13]A. Benoit, C. P. Umbach, R. B. Laibowitz, and R. A. Webb, "Length-Independent Voltage Fluctuations in Small Devices", Physical Review Letters **58**, 2343–2346 (1987).

[14]R. A. Webb, S. Washburn, H. J. Haucke, A. D. Benoit, C. P. Umbach, and F. P. Milliken, "Quantum Interference Effects in Disordered Sub-micron Wires and Rings", in Physics and Technology of Submicron Structures, edited by H. Heinrich, G. Bauer, and F. Kuchar, Springer Series in Solid-State Sciences (1988), pp. 98–107.

[15]T. J. Thornton, M. Pepper, H. Ahmed, G. J. Davies, and D. Andrews, "Universal conductance fluctuations and electron coherence lengths in a narrow two-dimensional electron gas", Physical Review B **36**, 4514–4517 (1987).

[16]H. van Houten, B. J. van Wees, J. E. Mooij, G. Roos, and K. .-F. Berggren, "Magnetic depopulation of subbands and universal conductance fluctuations in quasi-one dimensional GaAs-AlGaAs heterostructures", Superlattices and Microstructures **3**, 497–501 (1987).

[17]P. A. Lee, A. D. Stone, and H. Fukuyama, "Universal conductance fluctuations in metals: effects of finite temperature, interactions, and magnetic field", Physical Review B **35**, 1039–1070 (1987).

[18]P. A. Lee, "Universal Conductance Fluctuations in Disordered Metals", in *Condensed Matter Theories: volume 2*, edited by P. Vashishta, R. K. Kalia, and R. F. Bishop (Springer US, Boston, MA, 1987), pp. 265–266.

[19]Y. Imry, "Active Transmission Channels and Universal Conductance Fluctuations", **1**, 249–256 (1986).

[20]C. W. J. Beenakker and H. van Houten, "Quantum Transport in Semiconductor Nanostructures", Solid State Physics **44**, 1–228 (1991).

[21]T. Ihn, *Semiconductor Nanostructures Quantum states and electronic transport* (Oxford University Press).

[22]B. L. Al'Tshuler, "Fluctuations in the extrinsic conductivity of disordered conductors", Soviet Journal of Experimental and Theoretical Physics Letters **41**, 648 (1985).

[23]P. A. Lee and A. D. Stone, "Universal conductance fluctuations in metals", Phys. Rev. Lett. **55**, 1622–1625 (1985).

Bibliography

[24]R. Landauer, "Spatial variation of currents and fields due to localized scatterers in metallic conduction", IBM J. Res. Dev. **32**, 306–316 (1988).

[25]N. W. Ashcroft and N. D. Mermin, *Solid State Physics* (Holt-Saunders, 1976).

[26]P. W. Brouwer, "On the random-matrix theory of quantum transport", PhD thesis (Citeseer, 1997).

[27]G. Livan, M. Novaes, and P. Vivo, "Introduction to Random Matrices - Theory and Practice", arXiv:1712.07903 [cond-mat, physics:math-ph] **26**, 10.1007/978-3-319-70885-0 (2018).

[28]A. Altland and M. R. Zirnbauer, "Novel Symmetry Classes in Mesoscopic Normal-Superconducting Hybrid Structures", Physical Review B **55**, Comment: Criticism of results by Nagao and Slevin withdrawn, 1142–1161 (1997).

[29]F. J. Dyson, "Statistical theory of the energy levels of complex systems. ii", Journal of Mathematical Physics **3**, 157–165 (1962).

[30]C. W. J. Beenakker, "Random-Matrix Theory of Quantum Transport", Reviews of Modern Physics **69**, Comment: 85 pages including 52 figures, to be published in Rev.Mod.Phys, 731–808 (1997).

[31]C. W. J. Beenakker, "Random-matrix theory of mesoscopic fluctuations in conductors and superconductors", Phys. Rev. B **47**, 15763–15775 (1993).

[32]S. Rotter and S. Gigan, "Light fields in complex media: mesoscopic scattering meets wave control", Reviews of Modern Physics **89**, 10.1103/revmodphys.89.015005 (2017).

[33]R. A. Jalabert, J.-L. Pichard, and C. W. J. Beenakker, "Universal quantum signatures of chaos in ballistic transport", Europhysics Letters (EPL) **27**, 255–260 (1994).

[34]A. Altland and M. R. Zirnbauer, "Random matrix theory of a chaotic andreev quantum dot", Physical Review Letters **76**, 3420–3423 (1996).

[35]A. Altland, B. D. Simons, and D. Taras-Semchuk, "Field Theory of Mesoscopic Fluctuations in Superconductor/Normal-Metal Systems", arXiv:cond-mat/9807371, Comment: 75 pages, REVTEX, twenty-four eps-figures included; submitted to Advances in Physics (1998).

[36]J. F. Annett, *Superconductivity, superfluids, and condensates / james f. annett.* eng, Oxford master series in condensed matter physics (Oxford University Press, Oxford ; New York, 2004).

[37]J. Bardeen, L. N. Cooper, and J. R. Schrieffer, "Theory of superconductivity", Phys. Rev. **108**, 1175–1204 (1957).

Bibliography

[38]M. R. Norman and C. Pépin, "The electronic nature of high temperature cuprate superconductors", Reports on Progress in Physics **66**, 1547–1610 (2003).

[39]H. Courtois, P. Charlat, P. Gandit, D. Mailly, and B. Pannetier, "The Spectral Conductance of a Proximity Superconductor and the Reentrance Effect", Journal of Low Temperature Physics **116**, 187–213 (1999).

[40]N. N. Bogoljubov, "On a new method in the theory of superconductivity", Il Nuovo Cimento (1955-1965) **7**, 794–805 (1958).

[41]C. W. J. Beenakker, "Random-matrix theory of majorana fermions and topological superconductors", Reviews of Modern Physics **87**, 1037–1066 (2015).

[42]P. W. Brouwer and C. W. J. Beenakker, "Insensitivity to Time-Reversal Symmetry Breaking of Universal Conductance Fluctuations with Andreev Reflection", Physical Review B **52**, Comment: 8 pages, REVTeX-3.0, 2 figures, 16772–16775 (1995).

[43]D. K. Schroder, *Semiconductor material and device characterization*, English (John Wiley & Sons, Incorporated, Hoboken, 2015).

[44]D. V. Beznasyuk, S. Martí-Sánchez, J.-H. Kang, R. Tanta, M. Rajpalke, T. Stankevič, A. W. Christensen, M. C. Spadaro, R. Bergamaschini, N. N. Maka, C. E. N. Petersen, D. J. Carrad, T. S. Jespersen, J. Arbiol, and P. Krogstrup, *Doubling the mobility of inas/ingaas selective area grown nanowires*, 2022.

[45]H. H. Choi, K. Cho, C. Frisbie, H. Sirringhaus, and V. Podzorov, "Critical assessment of charge mobility extraction in fets", Nature Materials **17**, 2–7 (2017).

[46]Ö. Gül, D. J. van Woerkom, I. van Weperen, D. Car, S. R. Plissard, E. P. A. M. Bakkers, and L. P. Kouwenhoven, "Towards high mobility InSb nanowire devices", en, Nanotechnology **26**, 215202 (2015).

[47]P. Aseev, G. Wang, L. Binci, A. Singh, S. Martí-Sánchez, M. Botifoll, L. J. Stek, A. Bordin, J. D. Watson, F. Boekhout, D. Abel, J. Gamble, K. Van Hoogdalem, J. Arbiol, L. P. Kouwenhoven, G. de Lange, and P. Caroff, "Ballistic InSb Nanowires and Networks via Metal-Sown Selective Area Growth", Nano Letters **19**, 9102–9111 (2019).

[48]"Bottom-up grown 2d insb nanostructures", English, Advanced Materials **31**, `10.1002/adma.201808181` (2019).

Bibliography

[49]S. J. Pauka, J. D. S. Witt, C. N. Allen, B. Harlech-Jones, A. Jouan, G. C. Gardner, S. Gronin, T. Wang, C. Thomas, M. J. Manfra, J. Gukelberger, J. Gamble, D. J. Reilly, and M. C. Cassidy, "Repairing the surface of inas-based topological heterostructures", Journal of Applied Physics **128**, 114301 (2020).

[50]S. Dayeh, C. Soci, P. Yu, E. Yu, and D. Wang, "Transport properties of inas nanowire field effect transistors: the effects of surface states", Journal of Vacuum Science & Technology B: Microelectronics and Nanometer Structures **25**, 1432–1436 (2007).

[51]M. Kjaergaard, "Proximity induced superconducting properties in one and two dimensional semiconductors", PhD thesis (University of Copenhagen, 2005).

[52]L. Ö. Olsson, C. B. M. Andersson, M. C. Håkansson, J. Kanski, L. Ilver, and U. O. Karlsson, "Charge accumulation at inas surfaces", Phys. Rev. Lett. **76**, 3626–3629 (1996).

[53]J. R. Weber, A. Janotti, and C. G. Van de Walle, "Intrinsic and extrinsic causes of electron accumulation layers on inas surfaces", Applied Physics Letters **97**, 192106 (2010).

[54]V. Degtyarev, S. Khazanova, and N. Demarina, "Features of electron gas in inas nanowires imposed by interplay between nanowire geometry, doping and surface states", Scientific Reports **7**, 10.1038/s41598-017-03415-3 (2017).

[55]P. Krogstrup, N. L. B. Ziino, W. Chang, S. M. Albrecht, M. H. Madsen, E. Johnson, J. Nygård, C. M. Marcus, and T. S. Jespersen, "Epitaxy of semiconductor–superconductor nanowires", Nature Materials **14**, 400–406 (2015).

[56]W. Chang, S. M. Albrecht, T. S. Jespersen, F. Kuemmeth, P. Krogstrup, J. Nygård, and C. M. Marcus, "Hard gap in epitaxial semiconductor–superconductor nanowires", Nature Nanotechnology **10**, 232–236 (2015).

[57]D. J. Carrad, M. Bjergfelt, T. Kanne, M. Aagesen, F. Krizek, E. M. Fiordaliso, E. Johnson, J. Nygård, and T. S. Jespersen, "Shadow epitaxy for in situ growth of generic semiconductor/superconductor hybrids", Advanced Materials **32**, 1908411 (2020).

[58]T. Kanne, M. Marnauza, D. Olsteins, D. J. Carrad, J. E. Sestoft, J. de Bruijckere, L. Zeng, E. Johnson, E. Olsson, K. Grove-Rasmussen, and J. Nygård, "Epitaxial pb on InAs nanowires for quantum devices", Nature Nanotechnology **16**, 776–781 (2021).

Bibliography

[59]F. Krizek, J. E. Sestoft, P. Aseev, S. Marti-Sanchez, S. Vaitiekėnas, L. Casparis, S. A. Khan, Y. Liu, T. Stankevič, A. M. Whiticar, A. Fursina, F. Boekhout, R. Koops, E. Uccelli, L. P. Kouwenhoven, C. M. Marcus, J. Arbiol, and P. Krogstrup, "Field effect enhancement in buffered quantum nanowire networks", Physical Review Materials **2**, 10.1103/physrevmaterials.2.093401 (2018).

[60]N. Wang, X. Yuan, X. Zhang, Q. Gao, B. Zhao, L. Li, M. Lockrey, H. Tan, C. Jagadish, and P. Caroff, "Shape engineering of inp nanostructures by selective area epitaxy", ACS nano **13**, 10.1021/acsnano.9b02985 (2019).

[61]J. Winnerl, M. Kraut, S. Artmeier, and M. Stutzmann, "Selectively grown gan nanowalls and nanogrids for photocatalysis: growth and optical properties", Nanoscale **11**, 10.1039/C8NR09094G (2019).

[62]J. J. Sakurai and J. Napolitano, *Modern quantum mechanics*, 2nd ed. (Cambridge University Press, 2017).

[63]Oxford, *Triton™ 200/400, cryofree® dilution refrigerator manual, issue 3.7* (Copyright © 2015 Oxford Instruments plc, Tubney Woods, Abingdon, OX13 5QX, UK, 2015).

[64]F. Pobell, *Matter and Methods at Low Temperatures*, en, Third (Springer-Verlag, Berlin Heidelberg, 2007).

[65]-, *Dsp lock-in amplifier model sr830* (Stanford Research Systems Revision 2.5 edition, 2011).

[66]C. W. J. Beenakker and H. van Houten, "Flux-cancellation effect on narrow-channel magnetoresistance fluctuations", Phys. Rev. B **37**, 6544–6546 (1988).

[67]T. S. Jespersen, M. L. Polianski, C. B. Sørensen, K. Flensberg, and J. Nygaard, "Mesoscopic conductance fluctuations in InAs nanowire-based SNS junctions", en, New Journal of Physics **11**, 113025 (2009).

[68]C. W. J. Beenakker, "Why does a metal—superconductor junction have a resistance?", in *Quantum mesoscopic phenomena and mesoscopic devices in microelectronics* (Springer Netherlands, 2000), pp. 51–60.

[69]I. K. Marmorkos, C. W. J. Beenakker, and R. A. Jalabert, "Three signatures of phase-coherent andreev reflection", Phys. Rev. B **48**, 2811–2814 (1993).

[70]C. W. J. Beenakker, "Quantum transport in semiconductor-superconductor microjunctions", 10.48550/ARXIV.COND-MAT/9406083 (1994).

Bibliography

[71]A. E. Hansen, M. T. Björk, C. Fasth, C. Thelander, and L. Samuelson, "Spin relaxation in inas nanowires studied by tunable weak antilocalization", Phys. Rev. B **71**, 205328 (2005).

[72]Z. Scherübl, G. ő. Fülöp, M. H. Madsen, J. Nygård, and S. Csonka, "Electrical tuning of rashba spin-orbit interaction in multigated inas nanowires", Phys. Rev. B **94**, 035444 (2016).

[73]D. Liang and X. Gao, "Strong tuning of rashba spin-orbit interaction in single inas nanowires", Nano letters **12**, 3263–7 (2012).

[74]S. Nadj-Perge, S. M. Frolov, E. P. A. M. Bakkers, and L. P. Kouwenhoven, "Spin–orbit qubit in a semiconductor nanowire", Nature **468**, 1084–1087 (2010).

[75]C. W. J. Beenakker and H. van Houten, "Boundary scattering and weak localization of electrons in a magnetic field", Phys. Rev. B **38**, 3232–3240 (1988).

[76]O. Millo, S. J. Klepper, M. W. Keller, D. E. Prober, S. Xiong, A. D. Stone, and R. N. Sacks, "Reduction of the mesoscopic conductance-fluctuation amplitude in gaas/algaas heterojunctions due to spin-orbit scattering", Phys. Rev. Lett. **65**, 1494–1497 (1990).

[77]D. Pikulin, J. Dahlhaus, M. Wimmer, H. Schomerus, and C. Beenakker, "Zero-voltage conductance peak from weak antilocalization in a majorana nanowire", New Journal of Physics **14**, 10.1088/1367-2630/14/12/125011 (2012).

[78]S. Dhara, H. S. Solanki, V. Singh, A. Narayanan, P. Chaudhari, M. Gokhale, A. Bhattacharya, and M. M. Deshmukh, "Magnetotransport properties of individual inas nanowires", Physical Review B **79**, 10.1103/physrevb.79.121311 (2009).

[79]S. Ahn, H. Pan, B. Woods, T. D. Stanescu, and S. D. Sarma, *Estimating disorder and its adverse effects in semiconductor majorana nanowires*, 2021.

[80]H. H. Choi, K. Cho, C. D. Frisbie, H. Sirringhaus, and V. Podzorov, "Critical assessment of charge mobility extraction in FETs", Nature Materials **17**, 7 (2017).

[81]S. Das Sarma and E. H. Hwang, "Universal density scaling of disorder-limited low-temperature conductivity in high-mobility two-dimensional systems", Phys. Rev. B **88**, 035439 (2013).

[82]Y. Cao, V. Fatemi, S. Fang, K. Watanabe, T. Taniguchi, E. Kaxiras, and P. Jarillo-Herrero, "Unconventional superconductivity in magic-angle graphene superlattices", Nature **556**, 43–50 (2018).

Bibliography

[83]F. Bloch, "Bemerkung zur elektronentheorie des ferromagnetismus und der elektrischen leitfähigkeit", Zeitschrift für Physik **57**, 545–555.

[84]S. H. Simon, *The Oxford solid state basics* (Oxford Univ. Press, Oxford, UK, 2013).

[85]J. H. de Boer and E. J. W. Verwey, "Semi-conductors with partially and with completely filled3d-lattice bands", Proceedings of the Physical Society **49**, 59–71 (1937).

[86]N. F. Mott and R. Peierls, "Discussion of the paper by de boer and verwey", Proceedings of the Physical Society **49**, 72–73 (1937).

[87]S. Blundell, *Magnetism in condensed matter*, Oxford Master Series in Condensed Matter Physics (OUP Oxford, 2001).

[88]R. Hoffmann, "How chemistry and physics meet in the solid state", Angewandte Chemie International Edition in English **26**, 846–878 (1987).

[89]J. Law and R. Rennie, *Peierls instability* (Oxford University Press, 2020).

[90]M. C. Gutzwiller, "Effect of correlation on the ferromagnetism of transition metals", Physical Review Letters **10**, 159 (1963).

[91]J. Kanamori, "Electron correlation and ferromagnetism of transition metals", Progress of Theoretical Physics **30**, 275–289 (1963).

[92]J. Hubbard, "Electron correlations in narrow energy bands", Proceedings of the Royal Society of London. Series A. Mathematical and Physical Sciences **276**, 238–257 (1963).

[93]J. Hubbard, "Electron correlations in narrow energy bands iii. an improved solution", Proceedings of the Royal Society of London. Series A. Mathematical and Physical Sciences **281**, 401–419 (1964).

[94]R. T. Scalettar, "4 an introduction to the hubbard hamiltonian", in (2016).

[95]M. Cini and G. Stefanucci, "Antiferromagnetism of the two-dimensional hubbard model at half-filling: the analytic ground state for weak coupling", Journal of Physics: Condensed Matter **13**, 1279–1294 (2001).

[96]N. F. Mott, "Metal-insulator transition", Rev. Mod. Phys. **40**, 677–683 (1968).

[97]J. G. Bednorz and K. A. Müller, "Possible highTc superconductivity in the Ba-La-Cu-O system", Zeitschrift für Physik B Condensed Matter **64**, 189–193 (1986).

[98]P. Barthelemy and L. Vandersypen, "Quantum dot systems: a versatile platform for quantum simulations", Annalen der Physik **525**, 808–826 (2013).

Bibliography

[99]R. P. Feynman, "Simulating physics with computers", International Journal of Theoretical Physics **21**, 467–488 (1982).

[100]R. D. L. Kronig, W. G. Penney, and R. H. Fowler, "Quantum mechanics of electrons in crystal lattices", Proceedings of the Royal Society of London. Series A, Containing Papers of a Mathematical and Physical Character **130**, 499–513 (1931).

[101]R. L. Pavelich and F. Marsiglio, "Calculation of 2d electronic band structure using matrix mechanics", American Journal of Physics **84**, 924–935 (2016).